Neutron Studies of Magnetic Oxides with Triangular Motifs

Neutron Scattering Studies of Magnetic Oxides based on Triangular Motifs

By

Katharina Fritsch, B.Sc., M.Sc.

A Thesis

Submitted to the School of Graduate Studies

in Partial Fulfilment of the Requirements

for the Degree

Doctor of Philosophy of Science

McMaster University

DOCTOR OF PHILOSOPHY OF SCIENCE (2013) McMaster University

(Department of Physics and Astronomy) Hamilton, Ontario

TITLE: Neutron Scattering Studies of Magnetic Oxides based on Triangular Motifs

AUTHOR: Katharina Fritsch, B.Sc. (University Leipzig), M.Sc. (McMaster University)

SUPERVISOR: Dr. Bruce D. Gaulin

NUMBER OF PAGES: xxvi, 212

Abstract

The following dissertation presents neutron scattering studies on three specific magnetic insulating oxide materials whose lattice is based on triangular structural motifs. Each of the three materials studied, $LuCoGaO_4$, $Co_3V_2O_8$ and $Tb_2Ti_2O_7$, displays an interesting disordered ground state that is reached by different mechanisms: site disorder, geometric frustration, and quantum fluctuations induced by a transverse magnetic field. The main focus of this work is the characterization of the resulting magnetic ground states and magnetic excitations within these systems.

Chapters 3, 4 and 5 contain original work in the form of six research articles that have either been published or have been prepared for publication in peer-reviewed journals.

Chapter 3 describes studies of the quasi two-dimensional triangular layered antiferromagnet $LuCoGaO_4$. This material is found to exhibit a spin glass ground state as a result of geometrical frustration and site disorder inherent in this system. Below the freezing temperature, this system exhibits static, two-dimensional correlations consistent with frozen short-range correlated regions in the plane of the bilayers that extend over roughly five unit cells. The dynamic correlations reveal typical spin glass behavior upon cooling. Furthermore, a resonant gapped spin-wave-like excitation is observed, that can be related to the anisotropy in the system. Such an excitation is relatively uncommon in spin glasses and has been studied for the first time in such detail.

Chapter 4 is concerned with the study of the kagome staircase system $Co_3V_2O_8$. While prone to geometrical frustration due to its underlying kagome structural motif, this material is characterized by predominantly ferromagnetic interactions that lead to an unfrustrated, ferromagnetic ground state. In this chapter, departures from this conventional ground state by different disordering mechanisms are investigated. The first part focuses on the effects of site disorder by introducing quenched nonmagnetic impurities into the system. The growth of single crystals of $(Co_{1-x}Mg_x)_3V_2O_8$ is reported. These crystals reveal that the ferromagnetic ground state is very sensitive to doping, and show that a low doping concentration of 19% leads to a suppression of the ferromagnetic ground state below 1.5 K. This could be understood as percolation problem on the quasi two-dimensional kagome lattice including site and bond percolation. The second part focuses on the influence of a transverse magnetic field on the ground state of Ising spins, introducing quantum fluctuations that lead to quantum phase transitions at ~ 6.25, 7 and 13 T. The observed quantum phase transitions are characterized by distinct changes in the magnetic structure and their associated spin excitation spectra.

Chapter 5 presents studies on the pyrochlore antiferromagnet $Tb_2Ti_2O_7$, which is a proposed spin liquid candidate but whose actual ground state is still the topic of current debate. The ground state of $Tb_2Ti_2O_7$ was revisited by neutron scattering measurements, revealing a new phase in the low temperature low field phase diagram that can be described as a frozen antiferromagnetic spin ice that exhibits distinct elastic and inelastic scattering features.

Acknowledgements

The following work would not have been possible without the help of many talented people that I have been fortunate to work with during the last five years, and I would like to thank them here.

First of all, I would like to thank my supervisor, Dr. Bruce Gaulin, for welcoming me into his group and for giving me the chance to work on fascinating scientific problems, using not only the laboratories at McMaster University but at facilities all over the world. Thank you Bruce for your patience, your enthusiasm and your guidance throughout my degree.

All of the projects presented in this thesis were based on the availability of high-quality single crystals which were grown under the expert supervision of Hanna Dabkowska. I would like to thank her, not only for her time and efforts spent on many crystal growths, but also for many great words of advice, not just related to science but to life in general. I would also like to thank Antoni Dabkowski for his help and guidance on sample preparation and characterization.

I also thank Marek Kiela, who has become a good friend over the last seven years I spent at McMaster. His technical expertise has been invaluable in the lab where I could always count on him to get equipment to work.

At the neutron scattering facilities, the experiments were supported by many enthusiastic instrument scientists, who made every experiment an enjoyable experience. In particular, I wish to thank Garrett Granroth and Georg Ehlers at SNS, Kirrily Rule at HZB, Yiming Qiu and John Copley at NIST, and Zahra Yamani at Chalk River labs.

My time at McMaster would not have been the same without the company of my friends and in particular my lab and office mates over many years, Kate Ross, Pat Clancy and Jerod Wagman. It has been a pleasure to work with you.

Finally, I thank my parents for their continued patience, their love and support.

Co-Authorship

All of the projects presented in this thesis are a result of collaborative research efforts. While I was the principal investigator of each of the projects discussed in this thesis, this work greatly profited from the contributions of several co-authors. Their contributions are described below.

The single crystal of $LuCoGaO_4$ studied in Chapter 3 was grown by Hilary Noad as part of her fourth year undergraduate project under the supervision of Hanna Dabkowska. The sample characterization by Laue X-ray diffraction and magnetization measurements have been carried out by myself. I planned and performed the neutron scattering experiment on SEQUOIA, SNS that took place in November 2011. Instrument support was provided by Garrett Granroth. The subsequent experiment on CNCS resulted from beamtime initially intended for one of Kate Ross' projects that experienced sample environment issues. As a consequence, we were able to perform a complete parametric study of $LuCoGaO_4$. Kate Ross and myself planned this experiment, and Kate performed it while I ran an experiment at another facility at the same time. The experiment at CNCS was supported by Georg Ehlers. The data analysis as well as the writing of the manuscript was done by me.

The work on the kagome staircase system $Co_3V_2O_8$ presented in Chapter 4 arose out of initial neutron scattering measurements on the pure $Co_3V_2O_8$ compound by Mehmet Ramazanoglu, Pat Clancy and Carl Adams, which employed a single crystal provided to us by our collaborators at the Polish Academy of Sciences in Warsaw. Following this work, single crystals of pure $Co_3V_2O_8$ and its magnetically dilute variant $(Co_{1-x}Mg_x)_3V_2O_8$ have been grown by Mehmet Ramazanoglu and myself under the supervision of Hanna Dabkowska. The article on the crystal growth and the characterization of $(Co_{1-x}Mg_x)_3V_2O_8$ presented in Chapter 4.1 was written

by me. The neutron scattering measurements on $(Co_{1-x}Mg_x)_3V_2O_8$ described in Chapter 4.2 were performed at NIST in 2009, using the cold triple axis spectrometer SPINS and the disk chopper spectrometer DCS. The SPINS experiment was carried out by myself with the support of Zahra Yamani of the Canadian Neutron Beam Centre at Chalk River Laboratories. The DCS experiment was performed by myself. Instrument support at DCS was provided by Yiming Qiu. Additional polycrystalline samples of $(Co_{1-x}Mg_x)_3V_2O_8$ required for this study were prepared at McMaster University by myself with assistance of Casey Marjerrison. I performed the magnetization measurements, analyzed the data and wrote the article presented in Chapter 4.2.

The magnetization and neutron scattering measurements on $Co_3V_2O_8$ in transverse field described in Chapter 4.3 have been experimentally challenging and are a result of several experiments performed in 2010 and 2011. Magnetization measurements have been planned and carried out by myself and Kirrily Rule at HZB. The triple axis neutron scattering data were also obtained at HZB, using the cold triple axis spectrometer FLEX. These experiments were performed by myself, with instrument support from Kirrily Rule and Klaus Habicht. The time-of-flight measurements on CNCS were planned and carried out by me. Instrument support was provided by Georg Ehlers. I performed the data analysis and wrote the manuscript.

The neutron scattering experiments on $Tb_2Ti_2O_7$ described in Chapter 5.1 were performed in 2012 by myself at DCS, NIST and by Kate Ross on LET, ISIS. The data analysis of the DCS experiment and the article was written by me, with significant contributions from Kate Ross who analyzed and wrote the article sections pertaining to the LET measurement, and commented on the manuscript as a whole. The subsequent parametric neutron study presented in Chapter 5.2 was performed on DCS in March 2013 by myself, Edwin Kermarrec and Kate Ross. The specific

heat data were collected by David Pomaranski from Jan Kycia's group at the University of Waterloo. I analyzed the neutron scattering data and wrote the article, with contributions from Edwin Kermarrec and Bruce Gaulin. The $Tb_2Ti_2O_7$ single crystal used for both neutron studies has been grown in 2006 and has been used in previous studies by Kirrily Rule and Jacob Ruff.

Each of these projects was performed under the guidance of my supervisor Bruce Gaulin, and all of the manuscripts presented in Chapters 3 through 5 have greatly benefited from his input. The additional writing in this thesis is my own, for which I appreciate comments and corrections offered by Bruce Gaulin.

Table of Contents

List of Figures

List of Tables

Chapter 1

Introduction

This chapter provides an introduction to magnetism in insulating oxides, focusing on the topics that are most relevant to the materials investigated in this thesis, $LuCoGaO_4$, $Co_3V_2O_8$ and $Tb_2Ti_2O_7$. These topics include single ion properties, magnetic interactions, order and disorder, geometrical frustration, and a brief introduction to spin glasses and to quantum phase transitions. Additional details on the topics discussed here can be found in the books by Ashcroft and Mermin,[1] Blundell,[2] Plischke and Bergersen,[3] Lacroix *et al.*,[4] Diep,[5] Mydosh,[6] Fischer and Hertz,[7] and Sachdev,[8] and references therein. At the end of this chapter, a brief introduction is given for each of the materials studied to set the stage for the work presented in Chapters 3, 4 and 5.

1.1 Magnetism in insulating oxides

1.1.1 Single ion properties

The magnetic properties of ionic solids arise from magnetic moments associated with unpaired electrons in partially filled electron shells of the ions. In the insulating materials studied here, these magnetic moments are well-localized and form a magnetic sublattice inside the crystal structure. The magnetic moment of an ion is given by its total angular momentum $\mathbf{J}$ which combines the total spin and orbital angular momenta from the unpaired electrons as $\mathbf{J} = \mathbf{S} + \mathbf{L} = \sum_i \mathbf{s}_i + \mathbf{l}_i$. Its magnitude is given by $\hbar\sqrt{J(J+1)}$, where J is the angular momentum quantum number that can take values from $|L - S| \leq J \leq L + S$. In an isolated ion, the electronic configuration of the ground state multiplet is given by Hund's rules, which state that the total spin, S, and total orbital angular momentum, L, must be maximized in order to minimize the Coulomb repulsion between the electrons.[1] Given a total angular momentum J, the magnitude of the effective magnetic moment can then be expressed as

$$\mu_{\text{eff}} = g_J \mu_{\text{B}} \sqrt{J(J+1)}, \tag{1.1}$$

where $\mu_{\text{B}} = \frac{\hbar e}{2mc}$ is the Bohr magneton and g_J is the Landé g-factor given by

$$g_J = \frac{3}{2} + \frac{S(S+1) - L(L+1)}{2J(J+1)}. \tag{1.2}$$

However, the magnetic ion in a material is not free, but is located in the crystal environment where it is subject to the electrostatic field of the sur-

rounding ions in the lattice. This crystal electric field (CF) can split the degeneracy of the ground state J multiplet and thus affect the magnetic moment.

In $3d$ transition metal ions such as Co^{2+} studied in this thesis, the partially filled $3d$ orbitals are the outermost orbitals and thus strongly affected by the crystal field. Depending on the local environment of the ion (Figs. 1.1(a) and (b)), the five-fold degenerate d orbitals may split into two doubly degenerate e_g and three triply degenerate t_{2g} levels. In this case, the crystal field quenches the orbital angular momentum ($L = 0$) such that the magnetic moment is purely due to the total spin S of the ion. This total spin S is determined by the balance of the electron-electron interaction and the size of the crystal field. In the case of Co^{2+} with seven electrons in the $3d$ orbital, this can lead to a low-spin (S=1/2) or a high-spin ($S = 3/2$) electronic configuration based on the distribution of the seven electrons into the t_{2g} and e_g orbitals. As mentioned earlier, the effective magnetic moment is no longer given by Eqn. 1.1, but by

$$\mu_{\text{eff}} = g\mu_{\text{B}}\sqrt{S(S+1)}, \tag{1.3}$$

where g is taken as 2.00023 for the electron spin. Since this effective moment is based only on the spin angular moment, it implies that the moment would be isotropic. Deviations from this picture arising from a partially unquenched orbital momentum are usually included as small perturbation altering the value of g. It it also this crystal electric field that is responsible for the magnetocrystalline or single-ion anisotropy that constrains the magnetic moment to be oriented in a particular way with respect to its local environment, such as

shown in Figs. 1.1(a)-(c) for the case of the materials studied in this thesis that all exhibit so-called *easy-axis* anisotropy. In particular, for the case of the Co^{2+} ions, this easy-axis anisotropy shows that some unquenched orbital angular momentum is present.

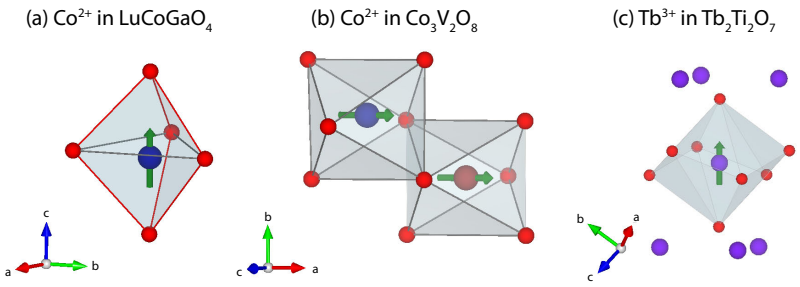

Figure 1.1: Local environments of the magnetic ions relevant in the three materials studied in this thesis. (a) $LuCoGaO_4$: Co^{2+} ion inside a triangular bipyramid of five O^{2-} ions, leading to easy-axis anisotropy with magnetic moment pointing along c. (b) $Co_3V_2O_8$: The two inequivalent Co^{2+} ions inside their edge-sharing distorted octahedra of six O^{2-} ions. The magnetic moments point along a. (c) $Tb_2Ti_2O_7$: Tb^{3+} ion inside a distorted cube of eight O^{2-} ions. The magnetic moment is Ising-like and favors to point along the cube diagonal connecting the centers of adjacent Tb tetrahedra or, equivalently, along the $\langle 111 \rangle$ direction.

For the rare-earth ions such as Tb^{3+} with eight electrons in the $4f$ shell, the crystal field plays a less important role in the determination of the ion's ground state. This is due to the fact that the partially filled $4f$ orbitals are closer to the nucleus and effectively shielded from the crystal electric field by the $5s$ and $5p$ orbitals. Hund's rules therefore give a reasonable description of the magnetic moment, with J being a good quantum number. However, the crystal field can still act as a perturbation on the spin-orbit coupling and can influence the magnetic moment and its anisotropy.

1.1.2 Magnetic interactions

Perhaps the simplest interaction between magnetic moments arises from the *dipolar interaction*. The energy for a magnetic moment $\boldsymbol{\mu}$ in a magnetic field $\mathbf{B}$ is given by $E = -\boldsymbol{\mu} \cdot \mathbf{B}$ where the magnetic field is created by another magnetic moment located at distance r:

$$\mathbf{B} = \frac{3(\boldsymbol{\mu} \cdot \hat{\mathbf{r}})\hat{\mathbf{r}} - \boldsymbol{\mu}}{r^3}. \tag{1.4}$$

The resulting dipolar interaction term is given by:

$$\mathcal{H}_{\text{dip}} = (g\mu_{\text{B}})^2 \sum_{\langle i,j \rangle} \left(\frac{\mathbf{S}_i \cdot \mathbf{S}_j}{r_{ij}^3} - 3\frac{(\mathbf{S}_i \cdot \hat{\mathbf{r}}_{ij})(\mathbf{S}_j \cdot \hat{\mathbf{r}}_{ij})}{r_{ij}^3} \right), \tag{1.5}$$

where the sum is carried out only over nearest neighbors (indicated by $\langle i, j \rangle$) separated by distance r_{ij} and the magnetic moments are denoted by the vector spin operators $\mathbf{S}_i$. As this dipolar interaction falls of as $1/\text{r}^3$, the interaction energy for typical separations ($r \approx 3$ Å) between moderately sized moments $\mu_{\text{eff}} \approx 3\mu_{\text{B}}$ is on the order of $\sim$ 0.1 meV or $\sim$ 1 K. However, for larger moments and systems which are frustrated or order at temperatures on the order of $\sim$1 K, dipolar interactions may well play an important role for the ground state selection. This is especially true for the rare-earth pyrochlore magnets known as classical dipolar spin ices, $Ho_2Ti_2O_7$ and $Dy_2Ti_2O_7$,[9] but less so for $Tb_2Ti_2O_7$, which has a smaller effective magnetic moment.

A more important interaction is the *exchange interaction* which arises from the overlap of the electron wave functions. It is given by

$$\mathcal{H}_{\text{ex}} = \sum_{i,j} J_{ij} \mathbf{S}_i \cdot \mathbf{S}_j. \tag{1.6}$$

Here, the J_{ij} are the exchange constants describing the interactions between spins i and j, which can be either positive, favoring an antiferromagnetic (anti-parallel) alignment of the spins, or negative, favoring ferromagnetic (parallel) alignment. The origin of this exchange interaction can be best understood by considering a two-electron system. According to the Pauli principle, the wave function of two spin-1/2 electrons has to be antisymmetric with respect to the exchange of the two electrons. Since the wave function of a two-electron system is written as a product of a spatial and spin dependent part, to obtain an antisymmetric spin function the spatial function must be symmetric or vice versa. Depending on the spatial part of the wave function, the spin part is either symmetric or anti-symmetric, leading to a $S = 1$ (triplet) or $S = 0$ (singlet) state, respectively. The spin coupling in these two cases would be either ferromagnetic or antiferromagnetic, respectively. The above example assumes a direct spatial overlap of the electronic orbitals of the neighboring ions and is therefore an example of *direct exchange*. In most insulating materials including the materials studied in this thesis however, the crystal structure is such that there is often no appreciable overlap between the wave functions of the magnetic ions, that are usually separated from each other by several Å. In this case, the exchange is indirect and mediated by a nonmagnetic ion such as O^{2-} that is located in between the two magnetic ions. This is called *superexchange*,

and it is highly dependent on the overlap of the orbitals of the magnetic and the nonmagnetic ions and thus on the bond angles between them. Whether interactions between ions are likely to be antiferromagnetic or ferromagnetic can be estimated from the Goodenough-Kanamori rules[10,11] that work well for simple geometries (ie. 90° or 180° bond angles).

Another type of magnetic interaction, usually much weaker than the exchange or the dipolar interactions, is the antisymmetric Dzyaloshinskii-Moriya (DM) interaction,[12,13] which is allowed by symmetry in the pyrochlore lattice of $Tb_2Ti_2O_7$.[14] It can be expressed as

$$\mathcal{H}_{\mathrm{DM}} = \sum_{\langle i,j \rangle} \mathbf{D}_{ij} \cdot (\mathbf{S}_i \times \mathbf{S}_j). \tag{1.7}$$

Here, $\mathbf{D}_{ij}$ is the DM vector. The DM interaction is allowed if the center of the bond connecting the two spins $\mathbf{S}_i$ and $\mathbf{S}_j$ does not have an inversion symmetry. The DM interaction energy is minimized if the angle between the interacting spins is 90° and if the spins are perpendicular to $\mathbf{D}_{ij}$. It therefore acts as an effective *easy-plane* anisotropy.

A Hamiltonian that includes all of the above interactions between nearest neighbors can be written as:

$$\begin{aligned} \mathcal{H} = & \sum_{\langle i,j \rangle} J_{ij} \mathbf{S}_i \cdot \mathbf{S}_j + (g\mu_{\mathrm{B}})^2 \sum_{\langle i,j \rangle} \left(\frac{\mathbf{S}_i \cdot \mathbf{S}_j}{r_{ij}^3} - 3 \frac{(\mathbf{S}_i \cdot \hat{\mathbf{r}}_{ij})(\mathbf{S}_j \cdot \hat{\mathbf{r}}_{ij})}{r_{ij}^3} \right) \\ & + \sum_{\langle i,j \rangle} \mathbf{D}_{ij} \cdot (\mathbf{S}_i \times \mathbf{S}_j) + \sum_i \sum_\alpha A_i^\alpha (\mathbf{S}_i^\alpha)^2 - g\mu_{\mathrm{B}} \sum_i \mathbf{S}_i \cdot \mathbf{H}, \end{aligned} \tag{1.8}$$

where J_{ij} is the exchange coupling, g is the Landé g-factor given earlier in Eqn. 1.2, r_{ij} is the distance between the sites i and j, $\hat{\mathbf{r}}_{ij}$ is the unit vector along the direction connecting sites i and j, and $\mathbf{D}_{ij}$ is the DM vector. Additionally, a term corresponding to the anisotropy is introduced, in which A_i^α are the anisotropy constants at site i related to the spin component $\alpha = (x, y, z)$. The final term in the above equation is the Zeeman term which introduces an energy splitting as a function of applied field $\mathbf{H}$.

As can be seen from this already fairly complex Hamiltonian, a theoretical description of the magnetic properties of a material involving only the most important interactions can quickly become a very difficult task. It is therefore very useful to have some prior knowledge about the most important interactions in the system which can be obtained from neutron scattering or magnetization measurements, for example.

1.1.3 Order and disorder

To understand how a magnetically ordered state arises, it is useful to consider the thermodynamic free energy of a system at temperature T, given by:

$$F = E - TS, \tag{1.9}$$

where E is the internal energy of the system associated with the spin interactions described in Eqn. 1.8, and S is the entropy. In the absence of any external work done on the system, the equilibrium configuration of the system is given by the configuration that minimizes the free energy. From this condi-

tion, two limiting cases arise, for temperatures large or small compared to the internal energy in the system.

Obviously, the entropic part always dominates for temperatures that are large compared to the relevant interaction energy in the system and thus keeps the system in a highly degenerate, disordered (paramagnetic) state. This state is characterized by a random orientation of each magnetic moment that at a given instant in time points in each possible direction with equal probability, thus preserving the rotational symmetry of the spins.

For temperatures comparable to or lower than the interaction energy, a state corresponding to a unique spin configuration that minimizes the internal energy E, can usually be reached. This state is generally referred to as *ordered state* and for $T = 0$ this ordered state is also the *ground state*. As a unique spin configuration is selected, this ordered state is characterized by a broken rotational spin symmetry. The simplest examples of magnetically ordered states are called ferromagnet (FM) or antiferromagnet (AFM), and they describe a global spin configuration in which all spins are aligned either parallel or antiparallel to each other, respectively. This *global* spin configuration implies a long-range ordered (LRO) state in which the spin correlation length ξ is of comparable size as the system. For comparison, a short-range ordered state (SRO) would be characterized by a correlation length much smaller than the system size.

A system reaches its long-range ordered state by going through a thermodynamic phase transition at a characteristic (critical) temperature T_{C}, provided that the thermal fluctuations are smaller than the magnetic interactions given

by Eqn. 1.8. The phase transition is usually characterized by the appearance of an order parameter, such as the magnetization M, which is zero above the transition and finite below it. The behavior of this order parameter at the critical temperature determines whether the phase transition is labeled discontinuous or continuous. A discontinuous phase transition is characterized by a discontinuous change in the order parameter, the presence of phase coexistence near T_{C}, a latent heat and thermal hysteresis. A continuous phase transition, on the other hand, is one in which the order parameter changes continuously at the phase transition. The temperature dependence of various physical parameters such as the magnetization, specific heat, the susceptibility, and the correlation length are found to have a characteristic power-law behavior, $f(t) \propto t^{-x}$, as a function of reduced temperature $t = \frac{T-T_{\mathrm{C}}}{T_{\mathrm{C}}}$, in the vicinity of T_{C}. This behavior is governed by different universal critical exponents x.

So far, the discussion has focused on how conventional long-range order arises. However, this does not always occur, as shown by the materials studied in this thesis that display interesting *disordered* ground states. The different mechanisms by which these materials reach their ground states will be discussed next.

1.1.4 Magnetic and geometric frustration

Frustration is, simply speaking, the inability of a system to satisfy all interactions simultaneously, and is thus observed most often in materials with competing interactions (magnetic frustration) or in materials based on magnetic sublattices that prevent simultaneous satisfaction of all interactions for

topological reasons (geometric frustration). Some excellent review articles of this topic exist in the literature.[15,16]

The concept of *magnetic frustration* is perhaps best illustrated by the well-known J_1-J_2 model on the square lattice shown in Fig. 1.2(a). While spins with *nearest-neighbor* antiferromagnetic coupling J_1 on the square lattice are not frustrated and the classical Néel states can satisfy all the interactions in the system, introduction of *next-nearest-neighbor* antiferromagnetic interactions J_2 (shown as diagonal bonds) leads to frustration which may prevent the selection of a unique long-range ordered ground state depending on the relative strengths of the interactions. In this particular case of a square lattice, a ratio of $J_2/J_1 = 0.5$ has been shown to lead to such a degenerate ground state, and the system remains disordered down to the lowest temperature, $T = 0$, and no phase transitions exists.[17,18]

Geometric frustration arises when the underlying lattice is responsible for frustrating the interactions, which can be isotropic, as in the prototypical example of the Ising AFM on the triangular lattice shown in Fig. 1.2(b). This problem was first studied by Wannier,[19] who showed that it was impossible to decorate the triangular plaquette with antiferromagnetic spins such that the interactions would be simultaneously satisfied, because the triangular lattice cannot be divided into unique sublattices for neighboring spins (the triangular lattice is said to be not bipartite). The exchange energy cannot be minimized for all three pair-wise interactions, leading to a degeneracy of the lowest energy configurations. This degeneracy can become macroscopic for a large periodic lattice composed out of either edge-sharing (Fig. 1.2(c)) or corner-sharing tri-

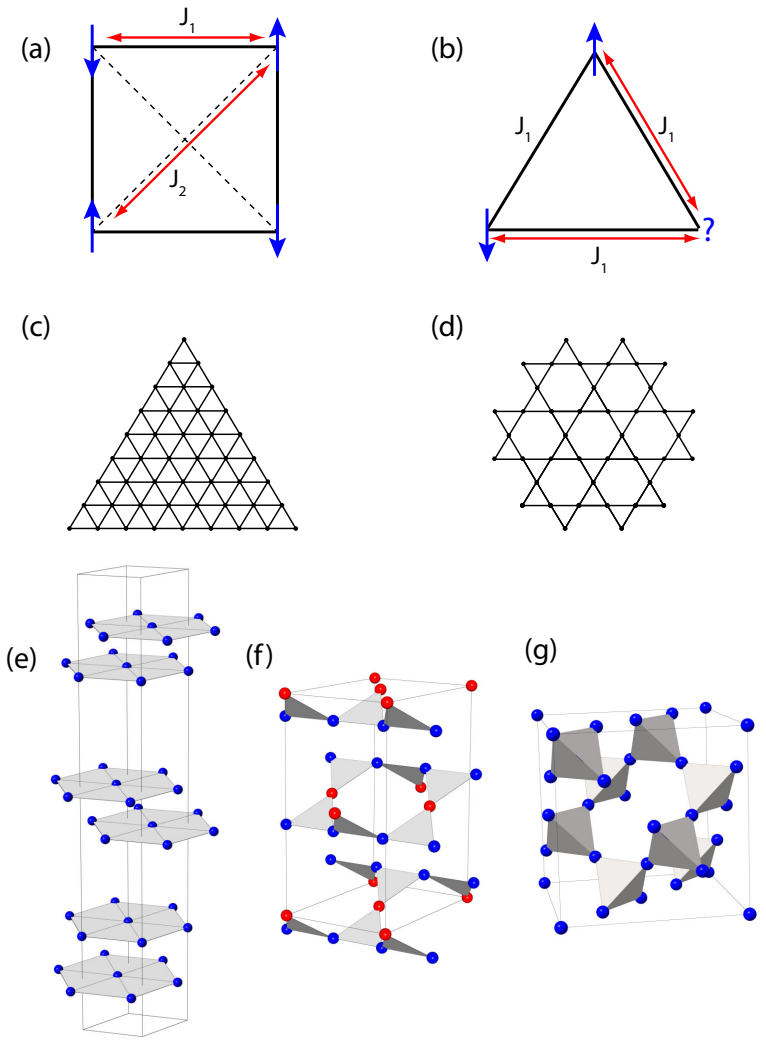

Figure 1.2: Different forms of frustration. (a) The J_1-J_2 model on the square lattice as an example of magnetic frustration. (b) Geometrical frustration on a triangular plaquette decorated with antiferromagnetically interacting Ising spins. (c) The two-dimensional triangular net composed of edge-sharing triangular plaquettes. (d) The two-dimensional kagome net composed of corner-sharing triangular plaquettes. (e) The magnetic sublattice of the antiferromagnetic triangular bilayer system $LuCoGaO_4$ studied in Chapter 3. (f) The magnetic sublattice of the kagome staircase system $Co_3V_2O_8$, made of buckled kagome layers, studied in Chapter 4. (g) The magnetic sublattice of the pyrochlore lattice of $Tb_2Ti_2O_7$, made of corner-sharing tetrahedra, studied in Chapter 5.

angular plaquettes (the kagome lattice in Fig. 1.2(d)), for which the number of degenerate ground states scales as the system size.

This idea can also be generalized to three dimensions in the following ways. One could think of either decorating a three-dimensional lattice by two-dimensional layers of edge-sharing triangular plaquettes ($LuCoGaO_4$ in Fig. 1.2(e), studied in Chapter 3), by tiling it with quasi two-dimensional corner-sharing triangular plaquettes ($Co_3V_2O_8$ in Fig. 1.2(f), studied in Chapter 4), or by creating a lattice out of the three-dimensional analogue to the triangle, the tetrahedron, which results in the pyrochlore lattice composed of corner-sharing tetrahedra ($Tb_2Ti_2O_7$ in Fig. 1.2(g), studied in Chapter 5).

While one might think that geometric frustration is a peculiar phenomenon and more of a theoretical construct, it is actually often observed in real-world magnetic systems, where antiferromagnetic interactions and geometries involving triangular motifs are quite common. In this thesis, two out of the three materials studied in this thesis are geometrically frustrated - only $Co_3V_2O_8$ does not strictly fall into this category as the exchange interactions are predominantly ferromagnetic.

Geometric frustration and its extensive ground state degeneracy leading to a finite zero temperature entropy imply that many systems can never achieve long-range magnetic order. However, such a disordered ground state scenario would violate the third law of thermodynamics that requires the entropy to vanish at zero temperature, and thus a unique single ground state must be selected eventually if the system is in equilibrium. This ground state is usually selected by weaker terms in the Hamiltonian or by lattice distortions, for

example, that collectively relieve the frustration and cause a transition to a long-range ordered state at a much reduced temperature scale in the system.

Other frustrated systems form (non-equilibrium) spin glass ground states wherein the moments are frozen into a disordered spin configuration, such a state will be discussed in Chapter 3. A special ground state arising from geometric frustration on the pyrochlore lattice is the so-called spin ice state, realized in $Ho_2Ti_2O_7$ and $Dy_2Ti_2O_7$. This state mimics the properties of water ice (thus the name) and is described by a spin configuration on each tetrahedron for which two spins point into and two spins point out of each tetrahedron, in analogy to the protons in water ice that are either near or far from the oxygen. This local spin configuration leads to six degenerate ground states per tetrahedron and consequently to a macroscopic degeneracy in the system that leads to an absence of a transition to long-range order down to 50 mK.[20,21]

In yet other materials, the magnetic moments remain dynamic down to the lowest temperature and never reach a transition to a frozen state, these materials are known as spin liquids. While theoretically proposed by Anderson in the 1970s,[22] the experimental realization of these has only recently been reported. The most prominent example is herbertsmithite[23,24] which is based on a system of s=1/2 moments decorating two-dimensional kagome layers. $Tb_2Ti_2O_7$ has also been proposed as spin liquid, however, its actual ground state is the subject of current debate. $Tb_2Ti_2O_7$ will be introduced later in this chapter and discussed in detail in Chapter 5.

1.1.5 Spin glasses

The spin glass state is a result of frustration and (random) site disorder, and it is characterized by a configuration of spins that is frozen into a more or less random pattern below its *freezing* temperature, T_f, below which the random, thermally active spin fluctuations become static. There is thus no long-range order in a spin glass.

The first spin glasses investigated in the 1970s and 1980s, today known as the canonical spin glasses, were the magnetic binary alloys $Cu_{1-x}Mn_x$ and $Au_{1-x}Fe_x$, in which the frustration arises from site-disordered impurity spins that interact via the long-range RKKY interaction.[6,25] It was later found that insulating materials also support spin glass states, and one of the first materials studied was $Eu_xSr_{1-x}S$.[26] However, these systems remain poorly understood due to the complexity of their behavior. One of the main problems arises from the absence of a single unique equilibrium spin glass ground state. In fact, spin glasses have a multi-valley free-energy landscape, which gives rise to a large number of low-energy metastable states that are separated by very small energy differences. The exact ground state found in the experiment therefore depends on the specific experimental conditions and as a consequence, hysteresis will be observed.

Experimentally, the spin glass state can be identified from several key signatures. Most commonly observed are:[16] a divergence of the field-cooled (FC) and zero field-cooled (ZFC) susceptibility below T_f, a strong frequency dependence of the ac-susceptibility in both the real and imaginary parts, the absence of long-range order, a linear T dependence of the magnetic contribution to the

specific heat at temperatures below T_f, and most importantly, a strong decrease in the spin fluctuations as T_f is approached from above, measured for example, by inelastic neutron scattering or μSR.

Several phenomenological parameters have been introduced to classify spin glass behavior based on the frequency dependence of its freezing temperature, T_f. One of them is the peak-shift per decade-frequency, sometimes also called Mydosh-parameter,[6] which is given by

$$p = \frac{\Delta T_\mathrm{f}}{T_\mathrm{f} \Delta \log_{10} f}, \tag{1.10}$$

where f is the frequency of the measurement and T_f the freezing temperature, and which is used to distinguish between canonical spin glass ($p < 0.01$), insulating spin glass behavior ($0.01 < p < 0.1$), and cluster glass or superparamagnetic behavior ($p > 0.1$).

Additionally, the frequency dependence of the freezing temperature has been described within a dynamic scaling approach,[27] however the critical exponents one usually finds are typically much higher than those of conventional phase transitions[28] and are therefore difficult to interpret.

In the work presented later in Chapter 3, a mainly qualitative description is therefore presented of the spin glass properties in $LuCoGaO_4$.

1.1.6 Quantum fluctuations

Another route to creating disordered ground states is by introducing quantum fluctuations into a long-range ordered ground state, which can lead to a

quantum phase transition (QPT).[8] In contrast to the classical thermodynamic phase transitions discussed above which are driven by thermal fluctuations, QPTs are related to a change in the magnetic ground state of a system in the absence of any thermal fluctuations, ie. at $T = 0$. These phase transitions are driven by some tuning parameter such as applied pressure, chemical doping, or, as will be discussed in Chapter 4.3, a transverse magnetic field, which will be introduced here shortly.

Experimental realizations of the transverse field Ising model have been discussed in the literature for the Ising chain system $CoNb_2O_6$[29] and for the three-dimensional dipolar exchange-coupled $LiHoF_4$,[30,31] but so far there have been no reports of a quantum phase transition in a quasi two-dimensional system, such as we will present in Chapter 4.3. Transverse field induced QPTs are difficult to observe experimentally, and a material that undergoes a QPT should have several key properties to make experimental investigations feasible. The exchange interaction between spins must not be too large, such that magnetic fields available in the laboratory are able to overcome the exchange. The exchange interaction should therefore be ~ 1 meV or smaller. The single-ion anisotropy constraining the moments to point along a specific direction in the lattice must have a sufficiently pronounced Ising character but again must not be too large. Also, an experimental contraint may be that the magnetic moment in the material should also not be too large, so that the torque is minimal when a magnetic field is applied transverse to the easy axis of the magnetic moments.

The quantum Ising model in a transverse magnetic field h can be described by the following Hamiltonian:*

$$\mathcal{H} = -J \sum_{\langle i,j \rangle} \sigma_i^z \sigma_j^z - h \sum_i \sigma_i^x. \tag{1.11}$$

Here, only near-neighbor interactions with ferromagnetic exchange constant J are considered (sum over $\langle i, j \rangle$), and in which h is, in units of energy, the transversely applied field (along x, transverse to the easy Ising axis of the spins z). The spin operators σ_i are the Pauli spin operators. The role of the externally applied field h is to tune the relative strengths of the two parts of the Hamiltonian.

For $h \to 0$, this model reduces to that of the quantum Ising model which has a ground state in which all spins are polarized in either the $+z$ or $-z$ direction. These two ground states can be represented as $|\uparrow\rangle$ and $|\downarrow\rangle$. Increasing the field strength h from 0, the field will mix the two up and down states by introducing quantum fluctuations via σ^x that reduce the magnetization in the same way as thermal fluctuations would in a classical system at finite temperatures. At very large fields $h \to \infty$, the system's ground state is one in which all spins are polarized along the field (along x), which corresponds to a different ground state that can be expressed as

$$|\rightarrow\rangle = \frac{1}{\sqrt{2}}(|\uparrow\rangle + |\downarrow\rangle). \tag{1.12}$$

* Following the notation of Sachdev,[8] where the dimensionless coupling parameter g is introduced as the parameter tuning the strength of the quantum fluctuation, we use here the parameter h in units of J, which is given explicitly by $h = g\mu_B H$ with H being the externally applied field.

There is therefore a phase transition at a critical field h_c, called quantum critical point (QCP), that separates the low-field ordered phase with finite order parameter $\langle \sigma^z \rangle \neq 0$ from the high-field *quantum disordered* phase in which $\langle \sigma^z \rangle = 0$. At the quantum critical point, the energies of the two ground states are degenerate. This has the interesting consequence that near the QCP, there should be a vanishing energy cost associated with fluctuations from the ground state to the first excited (nearly degenerate) state. The energy gap Δ between ground state and first excited state can therefore be described by a similar power-law as seen in conventional phase transitions:

$$\Delta \propto (h - h_c)^{z\nu}, \tag{1.13}$$

where z and ν are critical exponents determined by the universality class. It is this vanishing energy gap along with changes in the static and dynamic correlations of the system that will be of importance in the investigation of $Co_3V_2O_8$ in transverse field.

1.2 Introduction to the materials studied in this thesis

The three materials studied in this thesis exhibit a variety of disordered ground states that are reached by different disordering mechanisms, all departing from a conventional magnetic ground state. These mechanisms are illustrated in Fig. 1.3, which is adapted from Ramirez *et al.*'s review on "Strongly geometrically frustrated magnets".[15]

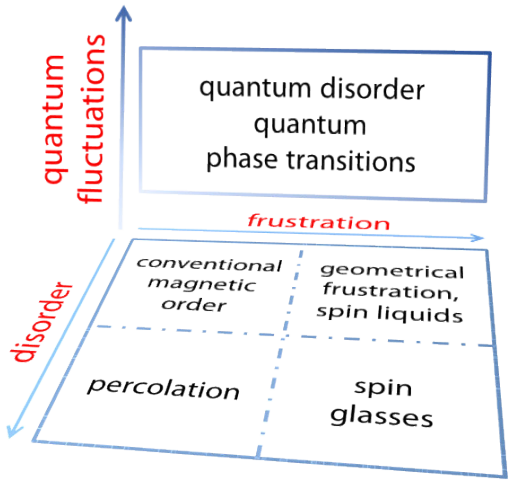

Figure 1.3: Ground states of the insulating magnets investigated in this thesis from the perspective of disorder, frustration and quantum fluctuations, adapted from Ramirez *et al.*[15]

In Chapter 3, the effects of geometric frustration and site disorder lead to a spin glass state studied in the triangular bilayer system $LuCoGaO_4$. In Chapter 4.2, site disorder in the from of quenched nonmagnetic Mg ions is studied in $(Co_{1-x}Mg_x)_3V_2O_8$, leading to a percolation problem. Chapter 4.3 explores the effects of quantum fluctuations on the ferromagnetic ground state of $Co_3V_2O_8$. These quantum fluctuations are introduced by a transverse magnetic field. Finally, in Chapter 5, the rare-earth pyrochlore system $Tb_2Ti_2O_7$ is discussed, in which geometric frustration leads to a disordered ground state that has been labeled as a spin liquid in the literature.

In what follows, each of the three materials is briefly introduced. For a more detailed discussion, the reader is referred to the manuscripts in each of the chapters.

1.2.1 The triangular bilayer system $LuCoGaO_4$

$LuCoGaO_4$ is a triangular layered antiferromagnetic spin glass, in which geometric frustration is realized by antiferromagnetically coupled $s = 3/2$ magnetic moments decorating planar triangular bilayers (Fig. 1.2(e) and Fig. 3.1) that are effectively decoupled from each other, creating a quasi two-dimensional system. Site disorder arises from a random distribution of Co^{2+} and nonmagnetic Ga^{3+} ions within the bilayers, creating a spin glass state below $T_g \sim 19$ K, that has been reported for the first time by Cava *et al.* in 1998 for polycrystalline samples.[32]

The material crystallizes in the hexagonal RFe_2O_4 type structure, which has attracted considerable interest for not only its possible spin liquid or spin glass properties but also for the interplay between charge and magnetic order that can be studied, as has been the shown for the multiferroic $LuFe_2O_4$ in which a mixture of Fe^{2+} and Fe^{3+} occupies the triangular bilayers.[33,34]

Detailed studies of the static and dynamic correlations in $LuCoGaO_4$ by means of neutron scattering have so far lacked because of the unavailability of large, high-quality single crystals. Our group has been successful in growing a large, pristine single crystal of $LuCoGaO_4$, which we investigate in Chapter 3, using magnetization measurements and time-of-flight neutron scattering techniques.

1.2.2 The kagome staircase system $Co_3V_2O_8$

The kagome staircase material $Co_3V_2O_8$ (CVO) is based on a magnetic sublattice of Co^{2+} ions that occupy two inequivalent crystallographic sites (so-called cross-tie and spine sites) on a buckled version of the kagome lattice that was introduced in Section 1.1.4. A picture of the magnetic sublattice is shown in Fig. 1.2(f) and in Fig. 4.6.

Previous work on CVO and other members of the kagome staircase family such as $Ni_3V_2O_8$ (NVO) has focused mainly on the characterization of their complex low temperature phase diagrams that consist of a series of 4 and 5 phase transitions below ~ 10 K, respectively.[35,36] For NVO, it was found that the ground state is antiferromagnetic, justifying the classification as geometrically frustrated material. In contrast, CVO is seen to undergo a first-order phase transition to a ferromagnetic ground state at $T_C \sim 6.2$ K, indicating that geometric frustration only plays a negligible role in the ordering mechanisms in this material.

The zero-field spin wave spectrum of CVO was measured by Ramazanoglu *et al.* in 2009.[37] These data were used to extract the exchange parameters using linear spin wave theory assuming a flat kagome lattice and only one type of magnetic ion on both cross-tie and spine sites. The resulting exchange parameters for cross-tie - spine interactions ($J_{cs} \sim 1.25$ meV) and for spine-spine interactions ($J_{ss} \sim 0$) and an additional anisotropy term on the order of $1 - 2$ meV are found to describe the observed spin wave spectrum well, even though several features are not captured, most notably the existence of six spin wave modes instead of three that have only been resolved recently in

this work (Chapter 4.3) or the detailed dispersion of the low-energy bands. Nevertheless, the exchange interactions determined in Ramazanoglu *et al.*'s work serve as a good approximation of CVO.

In order to better understand the relevant interactions in this system, the magnetic behavior of the system in the presence of quenched *nonmagnetic* impurities can be studied. While dilution studies of CVO with magnetic Ni ions have been performed,[38,39] these have introduced even more complex magnetic behavior and have helped only little to understand the pure CVO system better.

As will be shown in Chapters 4.1 and 4.2, the CVO system can be diluted with Mg^{2+} ions that almost randomly substitute for the Co^{2+} ions at the cross-tie and spine sites. The magnetic phase diagram as a function of nonmagnetic dilution will be presented in Chapter 4.2, and it will be seen that a two-dimensional percolation model based on site dilution (capturing the nonmagnetic quenched disorder) and bond dilution (capturing the effect of negligible interactions between spine sites) is able to explain the observed dilution-dependent suppression of the magnetic long-range order.

The effect of a transverse magnetic field inducing quantum fluctuations (see Section 1.1.6) in the ground state of CVO will be studied in Chapter 4.3. This study relies on the observation of a relatively weak ($J_{cs} \sim 1.25$ meV) ferromagnetic ground state below 6.2 K, as mentioned earlier. In addition, it has been shown that the magnetic behavior is highly anisotropic, favoring a uniaxial spin configuration with an easy axis along a at all temperatures below 11.2 K.[40] Our measurements will show that three quantum critical points exist

below 15 T, and that all of these are associated with interesting changes in the static and dynamic spin correlations.

1.2.3 The pyrochlore spin liquid candidate $Tb_2Ti_2O_7$

$Tb_2Ti_2O_7$ belongs to the family of magnetic rare-earth titanate pyrochlore oxides with the chemical formula $R_2Ti_2O_7$ that have recently received considerable attention due to their exotic low temperature properties such as ground state selection by order-by-disorder,[41,42] as well as classical[20,43–45] and quantum spin ice [46–51] physics.

The structure of $Tb_2Ti_2O_7$ is composed of trivalent R^{3+} rare-earth metal ions that occupy a network of corner-sharing tetrahedra known as the pyrochlore lattice (Fig. 1.2(g)), which has been introduced as the prototypical example of geometric frustration in three dimensions in Section 1.1.4.

$Tb_2Ti_2O_7$ has attracted much interest as a potential experimental realization of a quantum spin liquid,[52] based on its lack of long-range order down to at least 50 mK observed by neutron scattering, spin echo and μSR techniques,[53,54] despite having a Curie Weiss temperature of ~ -14 K[55] that would suggest ordering at ~ 1 K based on a mean-field treatment within the dipolar spin ice model.[9]

The Tb^{3+} ions ($J = 6$) in $Tb_2Ti_2O_7$ have an Ising crystal field doublet ground state that leads to $\langle 111 \rangle$ easy-axis anisotropy as in the canonical spin ice materials $Ho_2Ti_2O_7$ and $Dy_2Ti_2O_7$. In contrast to these materials however, the net exchange in $Tb_2Ti_2O_7$ is antiferromagnetic. This observation led to

an apparent contradiction, since the combination of Ising-like ⟨111⟩ anisotropy and antiferromagnetic interactions on the pyrochlore lattice are unfrustrated,[56] so that $Tb_2Ti_2O_7$ would be expected to form a unique long-range ordered ground state.

The work that will be presented in Chapter 5 has been motivated by the ongoing debate about the actual ground state of $Tb_2Ti_2O_7$. Two theoretical pictures have been proposed to explain the apparent lack of order in the ground state of $Tb_2Ti_2O_7$. One of them proposed a "quantum spin ice" (QSI) scenario,[57,58] which invokes virtual quantum excitations of the ions between the crystal field ground state doublet and the first excited doublet ($\Delta \sim 15$ K) that would reposition $Tb_2Ti_2O_7$ into a spin ice phase. This spin-ice phase should exhibit characteristic features, such as pinch-point scattering or a magnetization plateau for magnetic fields along [111], evidence for which has been controversially discussed in the literature.

Another possible scenario hinges on the fact that the Tb^{3+} ions are non-Kramers ions for which the doublet ground state is not protected a priori. It is therefore conceivable that a splitting of the accidental ground state doublet, for example by a structural distortion of a Jahn-Teller-type would result in a non-magnetic singlet ground state,[59] and that this singlet ground state would exclude the formation of a long-range ordered state. This scenario has been highly debated, as there is no conclusive evidence for a deviation from the cubic structure at low temperatures.

In the work that will be discussed in Chapter 5, the ground state of $Tb_2Ti_2O_7$ will be re-investigated using neutron techniques, and it will be shown

that a new, previously unobserved, low-temperature low-field phase exists in the phase diagram of this material. These measurements will also shown to be inconsistent with the non-magnetic singlet scenario.

1.3 * References

[1] N. W. Ashcroft and D. N. Mermin, *Solid state physics*, 1 ed. (Thomson Learning, Toronto, 1976).

[2] S. Blundell, *Magnetism in Condensed Matter (Oxford Master Series in Condensed Matter Physics)* (Oxford University Press, USA, Oxford, 2001).

[3] M. Plischke and B. Bergersen, *Equilibrium Statistical Physics* (World Scientific Pub Co Inc, Singapore, 1994).

[4] C. Lacroix, P. Mendels, and F. Mila, in *Introduction to Frustrated Magnetism* (Springer Series in Solid-State Sciences, Heidelberg, 2011).

[5] H. T. Diep, *Frustrated Spin Systems* (World Scientific Pub Co Inc, Singapore, 2005).

[6] J. A. Mydosh, *Spin Glasses: An Experimental Introduction* (CRC Press, Bristol, PA, 1993).

[7] K. H. Fischer and J. A. Hertz, *Spin Glasses (Cambridge Studies in Magnetism)* (Cambridge University Press, Cambridge, UK, 1993).

[8] S. Sachdev, *Quantum Phase Transitions* (Cambridge University Press, New York, 2000).

[9] B. den Hertog and M. Gingras, Phys. Rev. Lett. **84**, 3430 (2000).

[10] J. B. Goodenough, Phys. Rev. **100**, 564 (1955).

[11] J. Kanamori, J. Phys. Chem. Solids **10**, 87 (1959).

[12] I. Dzyaloshinskii, J. Phys. Chem. Solids **4**, 241 (1958).

[13] T. Moriya, Phys. Rev. **120**, 91 (1960).

[14] M. Elhajal, B. Canals, R. Sunyer, and C. Lacroix, Phys. Rev. B **71**, 094420 (2005).

[15] A. P. Ramirez, Ann. Rev. Mater. Sci. **24**, 453 (1994).

[16] J. E. Greedan, J. Mater. Chem. **11**, 37 (2001).

[17] P. Chandra and B. Doucot, Phys. Rev. B **38**, 9335 (1988).

[18] E. Dagotto and A. Moreo, Phys. Rev. Lett. **63**, 2148 (1989).

[19] G. Wannier, Phys. Rev. **79**, 357 (1950).

[20] S. T. Bramwell and M. J. P. Gingras, Science **294**, 1495 (2001).

[21] M. J. Harris, S. T. Bramwell, D. F. McMorrow, T. Zeiske, and K. W. Godfrey, Phys. Rev. Lett. **79**, 2554 (1997).

[22] P. Anderson, Mat. Res. Bull. **8**, 153 (1973).

[23] J. S. Helton, K. Matan, M. P. Shores, E. A. Nytko, B. M. Bartlett, Y. Yoshida, Y. Takano, A. Suslov, Y. Qiu, J.-H. Chung, D. G. Nocera, and Y. S. Lee, Phys. Rev. Lett. **98**, 107204 (2007).

[24] T.-H. Han, J. S. Helton, S. Chu, D. G. Nocera, J. A. Rodriguez-Rivera, C. Broholm, and Y. S. Lee, Nature **492**, 406 (2012).

[25] V. Cannella and J. Mydosh, Phys. Rev. B **6**, 4220 (1972).

[26] D. Hueser, L. Wenger, A. van Duyneveldt, and J. Mydosh, Phys. Rev. B **27**, 3100 (1983).

[27] K. Binder and A. P. Young, Rev. Mod. Phys. **58**, 801 (1986).

[28] A. Ogielski and I. Morgenstern, Phys. Rev. Lett. **54**, 928 (1985).

[29] R. Coldea, D. A. Tennant, E. M. Wheeler, E. Wawrzynska, D. Prabhakaran, M. Telling, K. Habicht, P. Smeibidl, and K. Kiefer, Science **327**, 177 (2010).

[30] D. Bitko, T. Rosenbaum, and G. Aeppli, Phys. Rev. Lett. **77**, 940 (1996).

[31] H. M. Ronnow, Science **308**, 389 (2005).

[32] R. Cava, A. Ramirez, Q. Huang, and J. Krajewski, J. Solid State Chem. **140**, 337 (1998).

[33] J. Iida, M. Tanaka, Y. Nakagawa, S. Funahashi, N. Kimizuka, and S. Takekawa, J. Phys. Soc. Jpn. **62**, 1723 (1993).

[34] N. Ikeda, H. Ohsumi, K. Ohwada, K. Ishii, T. Inami, K. Kakurai, Y. Murakami, K. Yoshii, S. Mori, Y. Horibe, and et al., Nature **436**, 1136 (2005).

[35] Y. Chen, J. W. Lynn, Q. Huang, F. M. Woodward, T. Yildirim, G. Lawes, A. P. Ramirez, N. Rogado, R. J. Cava, A. Aharony, O. Entin-Wohlman, and A. B. Harris, Phys. Rev. B **74**, 014430 (2006).

[36] N. Rogado, G. Lawes, D. A. Huse, A. P. Ramirez, and R. J. Cava, Solid State Commun. **124**, 229 (2002).

[37] M. Ramazanoglu, C. P. Adams, J. P. Clancy, A. J. Berlinsky, Z. Yamani, R. Szymczak, H. Szymczak, J. Fink-Finowicki, and B. D. Gaulin, Phys. Rev. B **79**, 024417 (2009).

[38] N. Qureshi, H. Fuess, H. Ehrenberg, T. C. Hansen, C. Ritter, P. Adelmann, C. Meingast, T. Wolf, Q. Zhang, and W. Knafo, J. Phys.: Condens. Matter **20**, 095219 (2008).

[39] N. Qureshi, H. Fuess, H. Ehrenberg, B. Ouladdiaf, J. Rodriguez-Carvajal, T. C. Hansen, T. Wolf, C. Meingast, Q. Zhang, W. Knafo, and H. v Lohneysen, J. Phys.: Condens. Matter **20**, 235228 (2008).

[40] N. R. Wilson, O. A. Petrenko, and L. C. Chapon, Phys. Rev. B **75**, 094432 (2007).

[41] L. Savary, K. A. Ross, B. D. Gaulin, J. P. C. Ruff, and L. Balents, Phys. Rev. Lett. **109**, 167201 (2012).

[42] M. E. Zhitomirsky, M. V. Gvozdikova, P. C. W. Holdsworth, and R. Moessner, Phys. Rev. Lett. **109**, 077204 (2012).

[43] M. J. P. Gingras, in *Introduction to Frustrated Magnetism*, edited by C. Lacroix, P. Mendels, and F. Mila (Springer Series in Solid-State Sciences, Heidelberg, 2011), Chap. Spin Ices.

[44] C. L. Henley, Annu. Rev.: Condens. Matter Phys. **1**, 179 (2010).

[45] C. Castelnovo, R. Moessner, and S. Sondhi, Annu. Rev.: Condens. Matter Phys. **3**, 35 (2012).

[46] S. Lee, S. Onoda, and L. Balents, Phys. Rev. B **86**, 104412 (2012).

[47] S. Onoda and Y. Tanaka, Phys. Rev. Lett. **105**, 047201 (2010).

[48] S. Onoda and Y. Tanaka, Phys. Rev. B **83**, 094411 (2011).

[49] K. A. Ross, L. Savary, B. D. Gaulin, and L. Balents, Phys. Rev. X **1**, 021002 (2011).

[50] R. Applegate, N. R. Hayre, R. R. P. Singh, T. Lin, A. G. R. Day, and M. J. P. Gingras, Phys. Rev. Lett. **109**, 097205 (2012).

[51] L.-J. Chang, S. Onoda, Y. Su, Y.-J. Kao, K.-D. Tsuei, Y. Yasui, K. Kakurai, and M. R. Lees, Nat. Commun. **3**, 992 (2012).

[52] L. Balents, Nature **464**, 199 (2010).

[53] J. S. Gardner, S. R. Dunsiger, B. D. Gaulin, M. J. P. Gingras, J. E. Greedan, R. F. Kiefl, M. D. Lumsden, W. A. MacFarlane, N. P. Raju, J. E. Sonier, I. Swainson, and Z. Tun, Phys. Rev. Lett. **82**, 1012 (1999).

[54] J. S. Gardner, A. Keren, G. Ehlers, C. Stock, E. Segal, J. M. Roper, B. Fåk, M. B. Stone, P. R. Hammar, D. H. Reich, and B. D. Gaulin, Phys. Rev. B **68**, 180401 (2003).

[55] M. J. P. Gingras, B. C. den Hertog, M. Faucher, J. S. Gardner, S. R. Dunsiger, L. J. Chang, B. D. Gaulin, N. P. Raju, and J. E. Greedan, Phys. Rev. B **62**, 6496 (2000).

[56] S. T. Bramwell and M. J. Harris, J. Phys.: Condens. Matter **10**, L215 (1998).

[57] H. R. Molavian, M. J. P. Gingras, and B. Canals, Phys. Rev. Lett. **98**, 157204 (2007).

[58] H. R. Molavian, P. A. McClarty, and M. J. P. Gingras, (2009), arXiv:0912.2957v1 [cond-mat.stat-mech].

[59] P. Bonville, I. Mirebeau, A. Gukasov, S. Petit, and J. Robert, Phys. Rev. B **84**, 184409 (2011).

Chapter 2

Experimental Methods

The successful investigation of new magnetic materials by means of inelastic neutron scattering requires high-quality large single crystals with volumes on the order of $\sim$cm^3, in particular if one wishes to study materials with small magnetic moment sizes or with a low density of magnetic moments. All single crystals studied in this thesis have been grown using the floating zone technique, which is described in Section 2.1 of this chapter. The growth of magnetically dilute $(Co_{1-x}Mg_x)_3V_2O_8$ has been published in Journal of Crystal Growth and is presented as separate section in Chapter 4.1.

Following successful crystal growth, the obtained samples have been characterized by Laue X-ray and neutron diffraction and their magnetic properties have been investigated using magnetization measurements. These measurements are briefly described in Section 2.2, and have been an essential component to the work presented in Chapter 4 in which magnetic phase diagrams as a function of composition (Section 4.2) or as a function of magnetic field (Chapter 4.3) are discussed.

The neutron scattering technique will be presented in some detail in Section 2.3. The theory of neutron scattering has been treated extensively in many excellent textbooks by Squires,[1] Lovesey,[2] and more recently by Shirane *et al.*[3] or by Chatterji.[4] I will therefore restrict myself to the discussion of the main results and their implications for the work described in this thesis, without re-deriving the equations in great detail. I will then go on to discuss the neutron instruments used in this thesis and lay out the reasoning for their use for the projects in this thesis.

2.1 Crystal growth

High-quality single crystals of magnetic oxides of sizes suitable for neutron scattering experiments can be grown using the optical floating zone (OFZ) technique.[5] One of the main advantages of this technique over conventional growth methods stems from the fact that no crucibles are needed, thus eliminating a source of possible contamination. The technique is very versatile and allows for the growth of both congruently or incongruently melting materials with relatively high melting points up to ~ 2200°C. In addition, the growth can be carried out in controlled gas atmospheres or under pressure.

The basic mechanism of OFZ growth involves the melting of ceramic material of the desired composition by focusing intense light from halogen lamps onto a small region using four ellipsoidal mirrors. Crystallization occurs by slowly translating the molten material out of this small, hot region. A schematic drawing of the floating zone furnace is shown in Fig. 2.1(a) along with a pho-

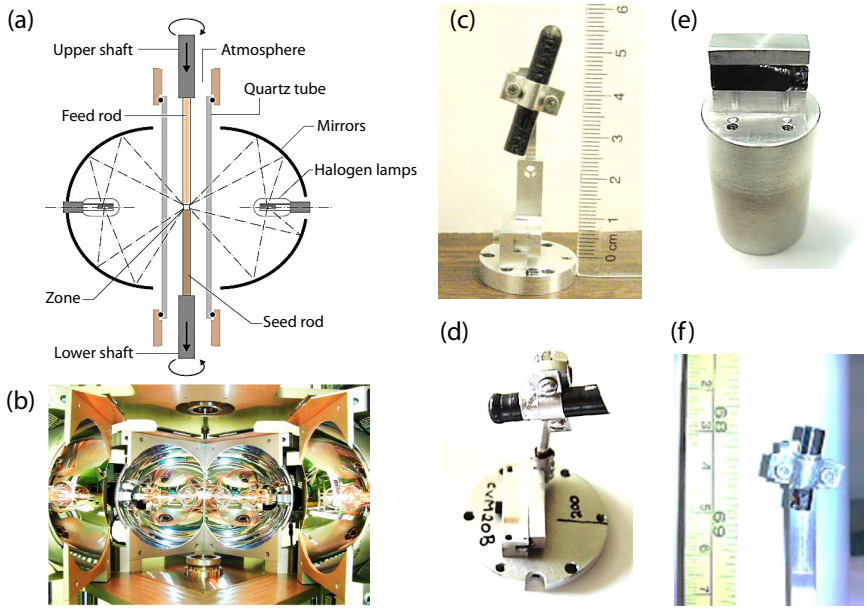

Figure 2.1: (a) A schematic diagram of the optical floating zone, taken from Ref. 5, (b) a photograph showing the inside of the Crystal Systems Inc. four-mirror floating zone furnace used in this thesis for the growth of $LuCoGaO_4$, $Co_3V_2O_8$ and $(Co_{1-x}Mg_x)_3V_2O_8$, (c) through (f) a subset of the samples studied in this thesis on their respective neutron sample mounts: (c) $LuCoGaO_4$ for measurements on SEQUOIA and CNCS, (d) $Co_3V_2O_8$ for measurements in strong transverse (vertical) magnetic fields, (e) $(Co_{1-x}Mg_x)_3V_2O_8$ for zero-field measurements on SPINS and DCS, and (f) $Tb_2Ti_2O_7$ for measurements in a dilution refrigerator magnet insert on DCS.

tograph of the mirror system of the Crystal Systems Inc. furnace employed in this thesis (Fig. 2.1(b)).

Growing crystals by the OFZ method first involves the preparation of ceramics (sintered polycrystalline rods) of the desired material through conventional solid state synthesis. These ceramics should be of uniform composition, density and thickness for an optimal growth outcome. One of the ceramic rods serves as the feed rod, and is suspended inside the floating zone furnace (Fig. 2.1(a)) from a rotating shaft that can be raised or lowered during the

growth. It is this feed rod that supplies material to the zone during the growth process. A second sintered rod or a previously grown single crystal of same or similar composition is used as seed rod on which the crystal growth takes place. This rod is mounted on the lower rotating shaft inside the furnace. For the growth, both feed and seed rods are placed in close proximity in the hot focal point of the mirrors, where a molten zone of material is created that stays suspended between the two solid rods due to surface tension. By translating the mirrors upwards, the molten zone crystallizes on the tip of the seed rod as the material cools. At the same time, the zone gets replenished as more material from the feed rod gets supplied to it. The growth speed or the rate at which the seed rod moves out of the zone determines the stability of the zone and ultimately the quality of the obtained single crystal. It can vary from 0.2 mm/h up to 30 mm/h, depending on the material. While it is generally found that crystals grown at slower speeds have fewer grains and are thus of better quality, it is sometimes necessary to grow samples at a faster growth rate to maintain a stable zone and to limit evaporation of volatile constituents.

The feed and seed rods are counter-rotated at variable speeds of ∼5-50 rpm to thoroughly mix the components in the zone to avoid compositional inhomogeneities or cellular growth and to further help to stabilize the zone. Additional growth parameters that need to be tuned are the lamp power and the feeding or backfeeding rate of the material supplying feed rod. Most of these parameters need to be determined empirically, and can vary from one growth to another based on the quality of the ceramic starting materials.

Under optimized growth conditions, single crystals of $\sim 3-5$ cm length and $\sim 5-7$ mm diameter can be obtained. These are usually cut from the main growth that can be up to ∼10 cm long. The single crystal samples studied in this thesis are shown in Fig. 2.1(c) through (f).

2.2 Magnetization measurements

The bulk magnetization measurements performed in this thesis used a Quantum Design Superconducting Quantum Interference Device (SQUID) magnetometer at McMaster University and a Quantum Design Vibrating Sample Magnetometer (VSM) at HZB. These measurements can be performed as a function of temperature and applied field, and can yield important information about the magnetic properties of the material as sharp changes or anomalies in the magnetization curve are usually used to identify phase transitions.

The basic measurement principle is the same in both instruments. To measure the sample magnetization in response to an externally applied magnetic field, the external field is varied at the sample position. The SQUID used in this thesis contains four pick-up coils connected in series, all surrounding the sample. The two outer coils are placed symmetrically above and below the sample, while the other two pickup coils, wound in the opposite direction, are located in the center of the sample space. This arrangement of the coils allows to filter out any homogeneous external field and to measure the remaining inhomogeneous field of the sample. This sample-dependent field induces an electric field proportional to its magnetization at the two inner coils.

The induced electric field is measured differently in the two instruments. The SQUID magnetometer at McMaster is an rf-SQUID which uses one Josephson junction (compared to the dc-SQUID that uses two) and employs the ac-Josephson effect.[6] As the magnetization of the sample induces a current in the superconductors of the Josephson junction, a voltage difference across the junction is created. This voltage difference is used to drive an inductively coupled tank circuit. The induced voltage in the tank circuit will be periodic with the change in magnetic flux at the Josephson junction, based on the voltage oscillation in the superconducting ring that corresponds to the change in flux by multiples of the flux quantum $\Phi_0 = h/2e = 2.07 \cdot 10^{-15}$ Tm^2.[7] From the tank circuit voltage, the magnetization of the sample can be deduced.

In the vibrating sample magnetometer (VSM), the sample is vibrated at low frequencies ($\sim$40 Hz) in the center of the pick-up coil and the induced current in the pick-up coil is measured by a lock-in amplifier to increase the signal-to-noise ratio. This method is less sensitive than the SQUID detection, but overall faster.

A further difference between the two instruments is their maximum magnetic field capability. At McMaster University, the magnetization up to a magnetic field of 5.5 T can be measured, while the VSM at HZB is able to achieve fields of 14 T. Both instruments are cooled with liquid ^{4}He and thus allow measurements in a temperature range of $\sim$1.5 K - 300 K.

2.3 Neutron scattering

Neutrons are massive, uncharged particles that interact primarily with matter via the strong nuclear force, scattering off of atomic nuclei. As electrically neutral particles, they have a much greater penetration depth than X-rays, and are thus probing the bulk properties of materials. Thermal neutrons have a de Broglie wavelength of $\sim$ 1.8 Å, which is a good match to the size of typical interatomic spacings in solids. Their energies are on the same order of magnitude as typical excitation energies in solids, making it feasible to study lattice excitations (phonons) or magnetic excitations (eg. magnons) by means of inelastic neutron scattering. Moreover, the neutron has a magnetic dipole moment $\boldsymbol{\mu}_n$ and can therefore interact with unpaired electrons in solids, making neutron scattering a powerful probe of magnetism.

2.3.1 Nuclear and magnetic scattering

In a neutron scattering experiment, the quantity being measured is the partial differential cross section $\frac{d^2\sigma}{d\Omega dE_f}$, which represents the number of neutrons scattered per second into a solid angle $d\Omega$ in a given direction with an energy between E_f and $E_f + dE_f$. In its most general form, the partial differential cross section can be obtained from Fermi's golden rule, or equivalently the first Born approximation, and is given by

$$\left.\frac{d^2\sigma}{d\Omega dE_f}\right|_{\sigma_i\lambda_i}^{\sigma_f\lambda_f} = \frac{k_f}{k_i}\left(\frac{m}{2\pi\hbar^2}\right)^2 |\langle \boldsymbol{k}_f\sigma_f\lambda_f|V|\boldsymbol{k}_i\sigma_i\lambda_i\rangle|^2\delta(E_{\lambda_i} - E_{\lambda_f} + \hbar\omega). \quad (2.1)$$

Here the initial (final) neutron states are described by their wave vectors $\boldsymbol{k}_i$ ($\boldsymbol{k}_f$) and their spin states σ_i (σ_f), while the initial (final) crystal states are labeled by λ_i (λ_f), and the interaction potential is given by V. E_i and E_f are the initial and final energies of the crystal state, and $\hbar\omega$ is the energy transfer of the neutron. The δ-function implies that energy is conserved in the scattering process.

As the scattering potential is weak, the incident and scattered neutrons can be treated as plane waves ($\Psi \propto e^{i\boldsymbol{k}\cdot\boldsymbol{r}}$) within the Born approximation, such that the term describing the interactions becomes:

$$\langle \boldsymbol{k}_f \sigma_f \lambda_f | V | \boldsymbol{k}_i \sigma_i \lambda_i \rangle| = \int V(\boldsymbol{r}) e^{i(\boldsymbol{k}_i - \boldsymbol{k}_f)\cdot\boldsymbol{r}} d\boldsymbol{r}. \tag{2.2}$$

This shows that the neutron scattering intensity measured by $\frac{d^2\sigma}{d\Omega dE_f}$ corresponds to the spatial Fourier transform of the crystal potential V. Eqn. 2.2 also reveals the important connection to the scattering vector $\boldsymbol{Q} = \boldsymbol{k}_i - \boldsymbol{k}_f$, which is related to the scattering angle θ measured in the experiment through Bragg's law given by

$$Q = \frac{4\pi}{\lambda}\sin(\theta). \tag{2.3}$$

Bragg's law is well-known from X-ray diffraction and states that for plane waves (such as X-rays or neutrons) incident on a set of lattice planes periodically spaced by a distance d, constructive interference of the scattered waves occurs if the condition $n\lambda = 2d\sin(\theta)$ is fulfilled, where n is an integer corresponding to the harmonics of the incident and scattered wavelength λ, d is the spacing of the lattice planes, and θ is the angle between the plane and the

incident or scattered beam. As $Q = \frac{2\pi}{d}$, the equation above results. A perhaps more revealing, alternate formulation of Bragg's law is the von Laue condition for diffraction, which is given by

$$2\pi n = \boldsymbol{d} \cdot (\boldsymbol{k}_i - \boldsymbol{k}_f), \tag{2.4}$$

in which n is an integer number, $\boldsymbol{d}$ is the displacement vector between two lattice points (or a Bravais lattice vector, $\boldsymbol{R}$) from which the neutrons/X-rays diffract constructively, and which implies that the change in wave vector must be equal to a reciprocal lattice vector $\boldsymbol{G} = \boldsymbol{k}_i - \boldsymbol{k}_f$.

The exact form of the neutron-nucleus interaction potential is not known analytically, but it is generally approximated by the Fermi pseudopotential given by

$$V(\boldsymbol{r}) = \frac{2\pi\hbar^2}{m} b\delta(\boldsymbol{r}), \tag{2.5}$$

which is essentially a delta function at the nucleus with scattering length b. This nuclear scattering length plays a similar role as the atomic form factor in X-ray scattering, however, unlike the X-ray atomic form factor, b varies in a non-systematic fashion from element to element, and even between isotopes of the same element, and it has no apparent Z dependence.

Using Eqn. 2.2 and 2.5, the expression for the partial differential cross section in Eqn. 2.1 can be arranged to give the general expression for nuclear scattering:

$$\frac{d^2\sigma}{d\Omega dE_f} = \frac{k_f}{k_i} \frac{1}{2\pi\hbar} \sum_{jj'} b_j b_{j'} \int \left\langle e^{-i\boldsymbol{Q}\cdot\boldsymbol{r}_{j'}(0)} e^{i\boldsymbol{Q}\cdot\boldsymbol{r}_j(t)} \right\rangle e^{-i\omega t} dt. \tag{2.6}$$

This expression shows that the nuclear scattering cross section essentially depends on the space and time correlation functions of the ions. Part of the above equation is sometimes referred to as the dynamic structure factor $S(\boldsymbol{Q},\omega)$ or the scattering function and given by

$$S(\boldsymbol{Q},\omega) = \frac{1}{2\pi\hbar N}\int \sum_{jj'} \left\langle e^{-i\boldsymbol{Q}\cdot\boldsymbol{r}_{j'}(0)} e^{i\boldsymbol{Q}\cdot\boldsymbol{r}_j(t)} \right\rangle e^{-i\omega t} dt. \tag{2.7}$$

$S(\boldsymbol{Q},\omega)$ is the Fourier transform of the time-dependent pair correlation function and as such the quantity of interest a neutron scattering experiment.

In the above equations, the sum over all individual ions with scattering lengths b_j can be separated in coherent and incoherent scattering contributions, of which only the former are of interest in this thesis. Coherent scattering reflects the periodicity of the crystal structure, giving rise to Bragg scattering with a distinct $\boldsymbol{Q}$ dependence, and arises from the average scattering lengths of particular elements. In contrast, incoherent scattering arises from the random distribution of different isotopes with different scattering lengths in the crystal, and produces a roughly $\boldsymbol{Q}$-independent elastic background.

In the case of magnetic neutron scattering, which is the main topic of this thesis, the interaction potential in Eqn. 2.1 needs to be modified to include the magnetic interaction potential

$$V_m = -\boldsymbol{\mu_n}\cdot\boldsymbol{B}, \tag{2.8}$$

where the neutron magnetic dipole moment is given by $\boldsymbol{\mu_n} = -\gamma\frac{e\hbar}{2m_p}\boldsymbol{\sigma}$. Here, $\boldsymbol{\sigma}$ is the Pauli spin operator with eigenvalues ± 1, γ is gyromagnetic ratio

with value 1.913 and $e\hbar/2m_p$ is the nuclear magneton. The magnetic field $\boldsymbol{B}$ arises from the magnetic dipoles created by unpaired electrons in the system. It is worth noting that this potential is no longer point-like (as the nuclear potential) but long-ranged.

After several manipulations, the partial differential cross section for magnetic scattering can be expressed as follows:

$$\frac{d^2\sigma}{d\Omega dE_f} = \frac{N(\gamma r_0)^2}{2\pi\hbar}\frac{k_f}{k_i}\left|\frac{1}{2}gF(\boldsymbol{Q})\right|^2 \sum_{\alpha,\beta}(\delta_{\alpha\beta} - \hat{Q}_\alpha\hat{Q}_\beta)\times \sum_{\boldsymbol{r}_j} e^{i\boldsymbol{Q}\cdot\boldsymbol{r}_j}\int \left\langle S_0^\alpha(0)S_{\boldsymbol{r}_j}^\beta(t)\right\rangle e^{-i\omega t}dt, \tag{2.9}$$

where r_0 is the classical electron radius and g the Landé splitting factor.

This equation has the following remarkable features that have important implications for the work discussed in this thesis.

The magnetic form factor $F(\boldsymbol{Q})$ is the Fourier transform of the spatial magnetization density associated with unpaired spins of the atomic electrons. As such, the magnetic form factor is seen to decrease at higher $|\boldsymbol{Q}|$ values, reducing the scattering intensity ($\propto |F(\boldsymbol{Q})|^2$) for both elastic and inelastic signals. This $\boldsymbol{Q}$-dependence of the magnetic form factor can be very useful to distinguish magnetic excitations from lattice excitations (phonons) which have an intensity that would increase as $|\boldsymbol{Q}\cdot\hat{\boldsymbol{e}}|^2$, with $\hat{\boldsymbol{e}}$ being the phonon polarization eigenvector.[3] The factor $(\delta_{\alpha\beta} - \hat{Q}_\alpha\hat{Q}_\beta)$ indicates that the cross section is only sensitive to the components of the magnetic moments that are perpendicular or transverse to the direction of $\boldsymbol{Q}$. Because of this factor, statements about the direction of the spin correlations can be made, even when

using an unpolarized neutron experiment that averages over all spin states as done in this thesis.

The time dependent spin-spin correlation function or the magnetic dynamic structure factor

$$S^{\alpha\beta}(\boldsymbol{Q},\omega) = \frac{1}{2\pi}\sum_{\boldsymbol{r}_j} e^{i\boldsymbol{Q}\cdot\boldsymbol{r}_j}\int \left\langle S_0^{\alpha}(0)S_{\boldsymbol{r}_j}^{\beta}(t)\right\rangle e^{-i\omega t}dt \tag{2.10}$$

is again the most important part of the cross section. It describes the time evolution of spin-spin correlations $\left\langle S_0^{\alpha}(0)S_{\boldsymbol{r}_j}^{\beta}(t)\right\rangle$ between a spin at the origin at time zero, and a spin j at position $\boldsymbol{r}_j$ at time t.

The above equations for the partial differential cross sections can be simplified for the case of elastic scattering, for which the initial and final neutron energies are the same.

For the case of coherent nuclear elastic scattering, Eqn. 2.6 reduces to

$$\frac{d\sigma}{d\Omega} = N\frac{(2\pi)^3}{v_0}\sum_{\boldsymbol{G}}\delta(\boldsymbol{Q}-\boldsymbol{G})|F_N(\boldsymbol{G})|^2, \tag{2.11}$$

in which the nuclear structure factor appears as

$$F_N(\boldsymbol{G}) = \sum_j b_j e^{i\boldsymbol{G}\cdot\boldsymbol{r}_j}, \tag{2.12}$$

and is directly related to the real space crystal structure, in analogy to the structure factor in X-ray scattering.

For magnetic coherent elastic scattering, the differential cross section becomes

$$\frac{d\sigma}{d\Omega} = N_m \frac{(2\pi)^3}{V_{0m}} \sum_{\boldsymbol{G}} \delta(\boldsymbol{Q} - \boldsymbol{G}) |F_M(\boldsymbol{G})|^2, \tag{2.13}$$

with the magnetic structure factor given explicitly by

$$F_M(\boldsymbol{G}) = \frac{\gamma r_0}{2} \sum_j g_j f_j(\boldsymbol{Q}) \boldsymbol{S}_j^{\perp}(\boldsymbol{G}) e^{i\boldsymbol{G}\cdot\boldsymbol{r}_j}. \tag{2.14}$$

Here, it becomes once more apparent that only the component of the magnetic moment perpendicular to the scattering vector, $\boldsymbol{S}_j^{\perp}(\boldsymbol{Q})$, contributes to the scattering amplitude along with the $\boldsymbol{Q}$-dependent magnetic form factor $f_j(\boldsymbol{Q})$, for which tabulated expressions for various transition metal and rare-earth ions based on the dipolar approximation exist.[8]

In both the nuclear and magnetic cases, scattering from a long-ranged ordered structure implies that Bragg peaks are only observed when the scattering vector $\boldsymbol{Q}$ is equal to a reciprocal lattice vector $\boldsymbol{G}$, as expressed by the δ-function.

2.3.2 Practical considerations

Because of the Fourier relationship between the correlations in real- and reciprocal space, sharp features in the observed neutron scattering pattern, either in energy or momentum transfer, correspond to long-lived excitations or long-range spatial ordering. Conversely, any broad feature in energy transfer implies a finite lifetime and short-lived excitations. A broad peak in $\boldsymbol{Q}$, usually called "diffuse" scattering, implies short-range spatial correlations. The real-space

correlation length ξ is inversely related to the half-width at half-maximum of the observed broad peak in reciprocal space through $\xi = 1/\text{HWHM}$, while the lifetime τ of an excitation corresponds to the inverse of its energy width via $\tau = 2\pi\hbar/\Delta E$.

In this thesis and neutron scattering experiments in general, scattering is described as elastic, quasielastic or inelastic. Elastic scattering probes the static correlations between spins and is observed as peak in intensity centered around $E = 0$. However, what is called elastic depends crucially on the energy-resolution of the spectrometer. For the state-of-the-art instruments in this thesis, energy resolutions at the elastic line of 1-3% of the incident neutron energy are usually achieved, corresponding to a lowest resolvable frequency of $\sim$5 GHz for cold neutrons with an incident energy of 1.3 meV. Lower frequencies down to the MHz range can be probed by the neutron spin echo technique or by other techniques such as μSR or NMR spectroscopy.

The term quasielastic is used to describe scattering that is still centered around $E = 0$, but wider than the resolution, implying slow fluctuations of nearly static correlations at a timescale shorter than the resolution limit. This distinction is especially important in spin glasses or potential spin liquids, in which no magnetic long-range order occurs and for which an important question to be answered is whether the spins remain dynamic (fluctuating) or whether they "freeze".

Inelastic scattering occurs at non-zero energy transfers and can be resolution-limited, implying infinitely long-lived excitations, or can be broader than the resolution, implying a finite lifetime of the excitation.

2.3.3 Neutron instrumentation

For the work presented in this thesis, two neutron techniques have been used: Triple-axis spectroscopy, first invented by Bertram Brockhouse in 1958 and for which he received part of the Physics Nobel Prize in 1994, and the time-of-flight spectroscopy technique. In particular, the following instruments have been used. At the NIST Center for Neutron Research, we used the cold triple-axis spectrometer SPINS (Chapter 4.2) and the cold time-of-flight spectrometer DCS (Chapter 4.2 and 5). At BER-II at HZB, we used the cold triple-axis spectrometer FLEX (Chapter 4.3). Finally, experiments were performed on the cold time-of-flight spectrometer CNCS (Chapter 3 and 4.3) and the thermal time-of-flight spectrometer SEQUOIA (Chapter 3) at the Spallation Neutron Source, ORNL.

2.3.3.1 Triple-axis spectroscopy

A triple axis spectrometer (TAS) is used on reactor-based neutron sources. Its design allows to independently control the incident and final neutron wave vectors and the momentum transferred to the sample.[3] A schematic diagram of a TAS spectrometer is shown in Fig. 2.2(a) along with a picture taken of the FLEX spectrometer during the experiment described in Chapter 4.3.

The operating principle of this instrument is based on scattering processes occurring at the three positions about which the parts of the instrument can be rotated: Bragg scattering occurs at the monochromator and the analyzer positions, while either Bragg or other scattering (for example, diffuse scattering) is observed at the sample position. The incident neutron wave vector

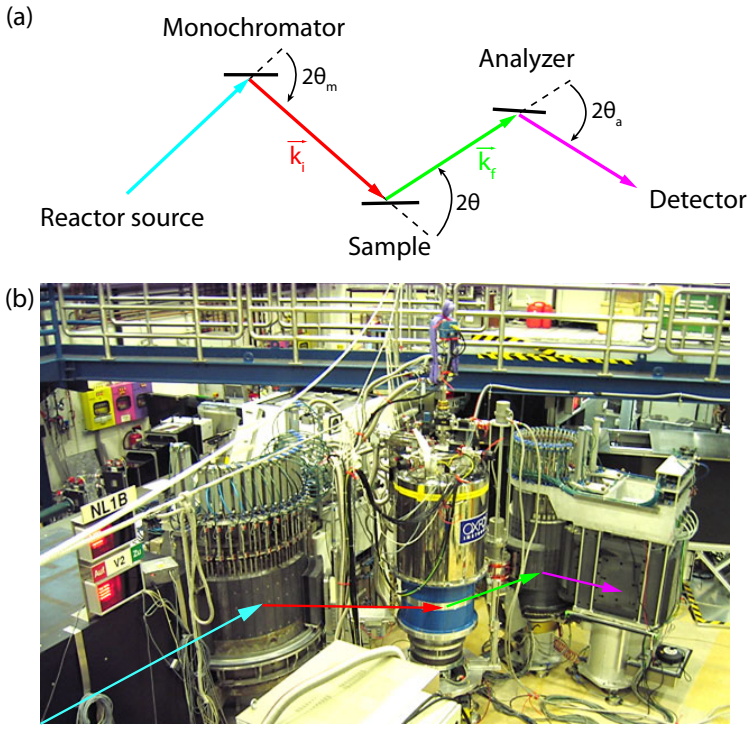

Figure 2.2: (a) Schematic diagram of a triple axis spectrometer (TAS). The instrument makes use of Bragg scattering at each of the three axes of the instrument: the monochromator, the sample, and the analyzer. (b) The FLEX TAS spectrometer at HZB during the experiments described in Chapter 4.3.

is selected through Bragg diffraction by the monochromator crystal, which is typically a large single crystal of known d-spacing oriented along a particular direction. A common monochromator material for cold neutrons is pyrolytic graphite (PG), which strongly reflects at its (0,0,2) Bragg position. The instrument is then rotated around the monochromator crystal, such that the neutrons with $\boldsymbol{k}_i$ can scatter from the sample. The detector arm holding both analyzer crystal and detector is rotated about the sample to select a specific scattering vector $\boldsymbol{Q} = \boldsymbol{k}_i - \boldsymbol{k}_f$. Finally, Bragg scattering at the analyzer crystal is used to select the final scattering wave vector $\boldsymbol{k}_f$ that is scattered in

the direction of the detector, thereby allowing the precise measurement of the scattering intensity at specific $\boldsymbol{Q}$ and energy transfers $\hbar\omega = E_i - E_f$.

Additional components of a TAS setup include collimators and beam filters. Collimators are usually Soller slits with variable slit spacings coated in neutron absorbing material such as Cd or Gd_2O_3. They are placed after each scattering axis: after the monochromator, before the analyzer and before the detector, and they help to further define the resolution of the instrument and to cut out background scattering. Beam filters are used to reduce scattering from higher-order wavelength diffraction that inevitably occurs using single crystal monochromators/analyzers such as PG, where simultaneous Bragg scattering occurs from (0,0,2) and (0,0,4), for example. Thus the beam does not only consist of neutrons with the desired $\boldsymbol{k}_i$, but also of neutrons with $2\boldsymbol{k}_i$ or $3\boldsymbol{k}_i$. To avoid these second or third order reflections, two types of filters are commonly used: PG and nitrogen cooled Be or BeO filters. The PG filter has a varying transmission based on the angle it makes with the incoming neutron wave vector, and it can therefore be tuned to transmit neutrons with specific wavelengths appreciably while suppressing the transmission of others. The Be-filter acts to block transmission of neutrons above $|\boldsymbol{k}| \sim 1.55$ Å^{-1}, making it ideal for the use on cold neutron instruments. Such a filter was used on SPINS and on FLEX for the work presented in Chapters 4.2 and 4.3.

Typically, TAS measurements are performed at constant k_i or constant k_f the latter of which is mostly used for practical reasons. Typical measurement methods involve constant-$\boldsymbol{Q}$ or constant-E scans, which keep some of the angles fixed. In a constant-E scan, both $\boldsymbol{k}_i$ and $\boldsymbol{k}_f$ are kept fixed, and the 2θ

angle at the sample as well as the rotation angle ψ of the sample are varied. In a constant-$\boldsymbol{Q}$ scan the energy transfer is varied, and both $\boldsymbol{k}_i$ and 2θ need to be varied appropriately.

TAS instruments are extremely flexible. However, since only a single detector is used, it may take a long time to collect a complete data set containing dispersion curves E vs $\boldsymbol{Q}$. This is where it become advantageous to use the time-of-flight technique.

2.3.3.2 Time-of-flight neutron scattering

Time-of-flight (TOF) neutron scattering experiments were performed in this thesis by using direct geometry spectrometers. These instruments do not rely on single crystal monochromators to define the incident and final neutron energies. Instead, the neutrons' incident and final wave vectors are determined from the time and distance it takes the neutrons to travel from the source to the sample and from the sample to the detector. Since the analysis of the final neutron energy occurs by the timing of neutron events, a wide range of energy transfers can be measured simultaneously. In addition, the newest state-of-the-art instruments used in this thesis, CNCS[9] and SEQUOIA,[10] are equipped with a wide array of position-sensitive detectors that cover a large portion of solid angle $d\Omega$, extending over ∼90-190° in the horizontal* and up to ±18° in the vertical direction. This combination makes modern TOF spectrometers

* The detectors on CNCS cover a horizontal angular range of -50° to 140°, while on SEQUOIA, the coverage is -30° to 60°.

extremely powerful, in that $S(\boldsymbol{Q}, E)$ can be obtained *simultaneously* for a wide range of $\boldsymbol{Q}$ and E.

TOF instruments are employed on both steady-state and pulsed neutron sources, with very similar operating principles.

The desired incident energy E_i is selected out of the Maxwellian neutron spectrum emitted from the source by a series of rotating choppers placed in the neutron beam. These choppers also define the pulse $t = 0$ (in the case of a steady-state source), and are used to absorb neutrons of unwanted higher energy. By rotating the choppers at specific speeds relative to each other, a narrow, well-defined neutron beam of desired neutron energy is allowed to pass through the chopper openings to the sample position at distance d_S. These neutrons of known velocity scatter off the sample at time t_S, either gaining or losing energy in the scattering process, and travel to the detectors at known distance d, where their time of arrival t_d and their angular position (ie the scattering angle 2θ) get recorded as a timing histogram. From the time of arrival t_d, the final neutron velocity and energy, v_f and E_f, can be determined by simple kinematics. Combining this information with the angular position of the recorded neutron at the detector, the final wave vector $\boldsymbol{k}_f$ can be determined, and thus the momentum transfer. The kinematic range determining the locus of the $(\boldsymbol{Q}, E)$ points that can be attained in the experiment for a given E_i and scattering angle 2θ is obtained from the relations for momentum and energy transfer as

$$
\begin{aligned}
Q^2 &= k_i^2 + k_f^2 - 2k_i k_f \cos 2\theta \\
\frac{\hbar^2}{2m} Q^2 &= E_i + E_f - 2\sqrt{E_i E_f} \cos 2\theta \\
\frac{\hbar^2}{2m} Q^2 &= 2E_i - \hbar\omega - 2\sqrt{E_i(E_i - \hbar\omega)} \cos 2\theta, \qquad (2.15)
\end{aligned}
$$

where the last line followed from $\hbar\omega = E_i - E_f$. It is this kinematic constraint that is responsible for the typical shape of the $S(\boldsymbol{Q}, E)$ slices seen in later chapters.

A schematic diagram of the Disk Chopper Spectrometer (DCS),[12] located at the 20 MW reactor of the NIST Center for Neutron Research, is shown in Fig. 2.3. This instrument uses a series of seven disk choppers to define the incident neutron energy. After scattering from the sample, neutrons travel over a distance of 4 m to the detector, which is formed by a stationary array of 913 ^{3}He detectors grouped in three detector banks. The DCS was used to collect data shown in Chapter 5, and for parts of Chapter 4.2.

The TOF technique is particularly well suited to pulsed neutron sources such as the Spallation Neutron Source (SNS) at ORNL, as it makes efficient use of the timing structure of the neutron beam.[13] The SNS is currently the world's most intense pulsed neutron source. The neutron generation occurs by a multiple-step process that is outlined briefly here.[14] First, negatively charged hydrogen ions are produced by an ion source and are accelerated up to ∼2.5 MeV. These ions are then injected into a linear accelerator where they

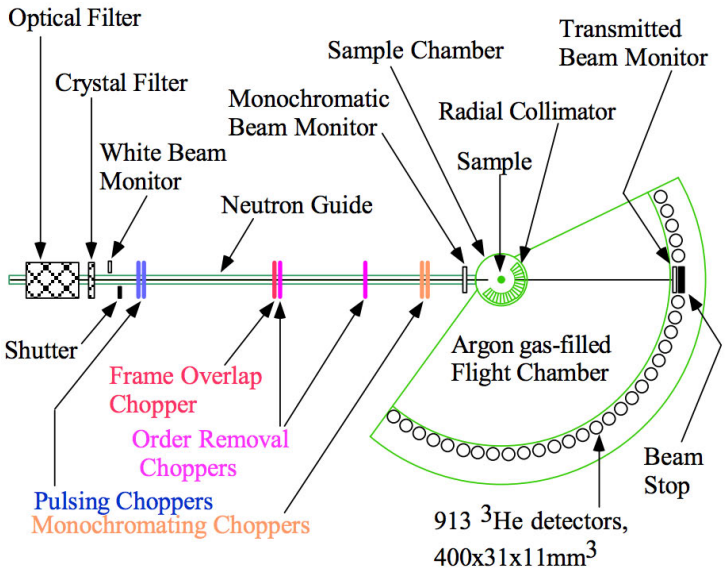

Figure 2.3: Schematic diagram of the Disk Chopper Spectrometer (DCS) at the NCNR, NIST.[11]

are accelerated up to $\sim$ 1 GeV, before being transferred into the accumulator ring. In that ring, the beam is bunched and intensified. The ions are then passed through a stripper foil, which strips off each ion's two outer electrons, creating a high-energy proton beam. The protons are further accumulated and are released as bunch from the ring at a pulse rate of 60 Hz with a pulse width of $\sim$1 μs. The high-energy proton beam pulses then strike a liquid mercury heavy-metal target, where the very efficient spallation process takes place. For every incident proton about 20-30 neutrons are expelled, at a pulsed rate of 60 Hz. (For comparison, in a nuclear reactor, only one to three neutrons are obtained in a single fission process). The neutron pulses are of very high energy and need to be slowed down to usable energies by thermal or cold moderators before arriving at the neutron guides leading to the instruments. The instruments used in this thesis, CNCS and SEQUOIA, are based off a

liquid hydrogen cold moderator and an ambient temperature (thermal) water moderator, respectively.

The TOF process on a pulsed neutron source is shown as timing diagram in Fig. 2.4 for the case of the SEQUOIA spectrometer[10] used in this thesis.

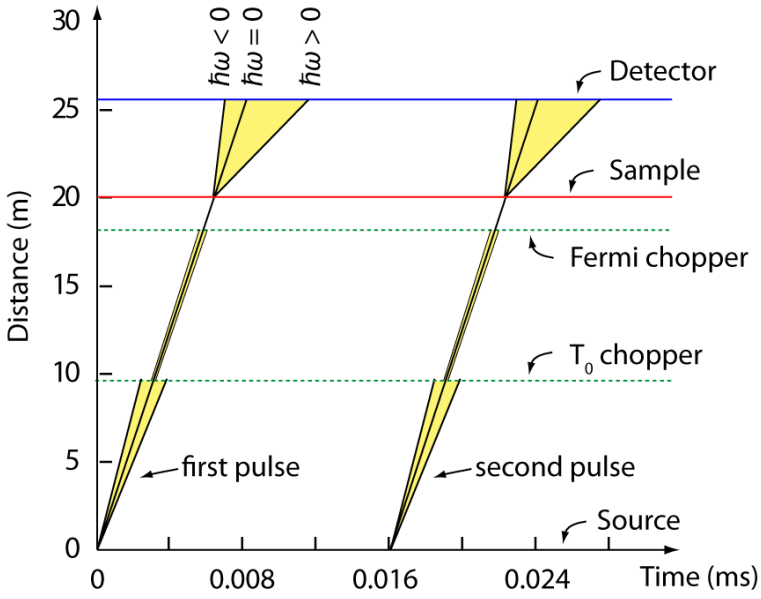

Figure 2.4: Timing diagram for the case of the SEQUOIA instrument showing the neutron flight path as a function of time. Choppers placed at specific distances are used to select the incident neutron energy by cutting out parts of the broad energy range of the neutron pulse (shown in yellow). At the sample, neutrons scatter elastically ($\hbar\omega = 0$) and inelastically ($\hbar\omega \neq 0$), and a range of energy transfers (yellow triangle) is simultaneously recorded by the detectors.

Pulses of neutrons come off the ambient water moderator (not shown here) at time $t = 0$ at a frequency of 60 Hz (or every 0.0167 ms). A first chopper, a so-called T_0 chopper, is located at $\sim$ 10 m from the moderator, and is used to suppress the prompt pulse of the fast neutrons created when the protons strike the liquid mercury target. This chopper is made from a thick piece of Inconel alloy material that scatters the prompt pulse neutrons into the surrounding

shielding. This chopper is rotated at multiples of the source frequency in-phase with the source. Usually, the T_0 chopper is designed to let a relatively broad bandwidth of neutrons through, however, in the case of the SEQUOIA instrument, the T_0 chopper is basically a very sloppy Fermi chopper that only lets a narrow bandwidth of neutrons ($\sim$0.01-2 eV) (yellow triangle) pass through to the next chopper at $\sim$18 m. This chopper is a so-called Fermi chopper, which is used to select a narrow, monochromatic neutron pulse. It consists of a series of closely spaced, curved, neutron-absorbing blades (called slit package) that spin about their vertical axis in the beam path at high frequencies up to 600 Hz. The length, curvature and the spacing of the slit package are important for the determination of the instrumental resolution.

After scattering from the sample positioned a further 2 m downstream, the neutron pulses travel over a distance of 5.5 m to a large array of detectors. Neutrons that have gained energy in the scattering process will travel faster and thus arrive more quickly at the detector, while neutrons that have lost energy to the sample arrive at the detectors at a later time.

A schematic diagram of the fine-resolution Fermi spectrometer SEQUOIA discussed above is shown in Fig. 2.5(a), illustrating the dimensions of the instrument and the actual neutron flight path. This instrument has been used for the experiment discussed in Chapter 3. Viewing the ambient/intermediate temperature H_2O moderator, it has a peak flux at around 80 meV. This instrument is ideally suited for research into magnetism, as it has very good low angle detector coverage down to 2.5°. The experimenter can choose between two Fermi choppers with different slit packages giving different flux and reso-

lution at the sample. These two choppers are mounted on a translation table and can be moved into or out of the beam. At the sample, the neutron beam is relatively wide (up to 5x5 cm), allowing the measurement of large samples.

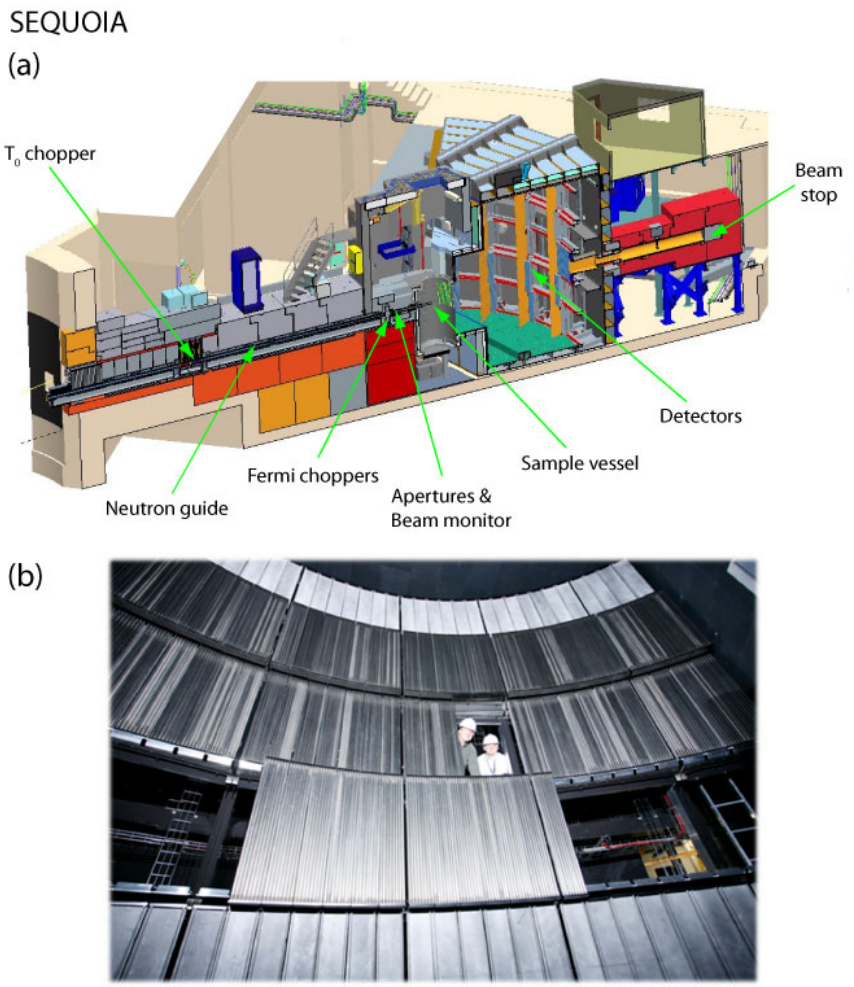

Figure 2.5: Schematic diagram of the fine-resolution Fermi spectrometer SEQUOIA at the SNS, ORNL. Figure courtesy of G. Granroth.

A peculiarity of the SEQUOIA instrument is the fact that the sample and detector vessel volumes are connected and evacuated during the experiment, therefore avoiding the use of neutron windows between sample and detector

that would introduce some additional scattering background. The detectors span a large region of space, extending from -30° to 60° in the horizontal and ±18° in the vertical direction. The detectors themselves are linear position sensitive ^{3}He tubes that are each 1.2 m long and 25 mm wide. They are grouped in packs of 8 and are placed on a cylindrical array 5.5 m away from the sample. A picture of SEQUOIA's detector array taken during the installation of the instrument is shown in Fig. 2.5(b).

The CNCS spectrometer[9] has been used for measurements discussed in Chapter 3 and 4.3. It views the liquid hydrogen cold moderator and is therefore best suited for measurements with cold neutrons with $E_i < 15$ meV. While both instruments have comparable flight paths from source to sample ($\sim 30-35$ m), this instrument differs from SEQUOIA in several ways. CNCS does not have a T_0 chopper, but a Fermi chopper that effectively varies the pulse length. In addition to this pulse-shaping chopper, the instrument has 3 more choppers along the flight path to the sample, the last two of which are used to define the incident energy of the neutrons. A total of 400 position sensitive ^{3}He detector tubes are located in a separate enclosure that is filled with a mixture of mostly argon gas and CO_2, and these cover -50° to 135° in the horizonal scattering plane and ±16° in the vertical direction.

In typical experiments on TOF instruments, the measurement of $S(\boldsymbol{Q}, E)$ is accomplished by rotating the sample in 0.5° or 1° steps around the vertical axis, which corresponds to a change in the direction of $\boldsymbol{k}_i$. For the materials investigated in this thesis, the reciprocal space maps are collected for rotations covering ∼120°. The collection time of a typical data set can range from 4 h

(CNCS data in Chapter 4.3) up to 14 h (SEQUOIA data in Chapter 3), depending on the scattering from the sample and the chosen step size of rotation. More recently, a new mode of measurement ("sweep" mode) has been introduced,[15] which is based on a slow continuous rotation of the sample that is repeated over many cycles. For this, the angular position of the sample must be precisely related to the timing of neutron events. This method has the potential advantage of enabling the experimenter to visualize the scattering from the sample in a much shorter time, helping in the planning of the experiment.

2.4 * References

[1] G. Squires, *Introduction to Thermal Neutron Scattering* (Cambridge University Press, Cambridge, UK, 1978).

[2] S. W. Lovesey, *The Theory of Neutron Scattering from Condensed Matter: Volume I and II (International Series of Monographs on Physics)* (Oxford University Press, USA, New York, 1985).

[3] G. Shirane, S. M. Shapiro, and J. M. Tranquada, *Neutron Scattering with a Triple-Axis Spectrometer: Basic Techniques* (Cambridge University Press, Cambridge, UK, 2002).

[4] T. Chatterji, *Neutron Scattering from Magnetic Materials* (Elsevier Science, Amsterdam, NL, 2006).

[5] H. A. Dabkowska and A. B. Dabkowski, in *Crystal Growth of Oxides by Optical Floating Zone Technique. Experimental Approach to Defects Determination* (Springer Handbook of Crystal Growth, Defects and Characterization, Berlin, Heidelberg, New York, Tokyo, 2010), pp. 367–392.

[6] M. Tinkham, *Introduction to Superconductivity: Second Edition (Dover Books on Physics)* (Dover Publications, New York, USA, 2004).

[7] W. G. Jenks, I. M. Thomas, and J. P. Wikswo, *SQUIDs* (Wiley Blackwell (John Wiley & Sons), New Jersey, USA, 2003).

[8] P. J. Brown, International Tables for Crystallography **C**, 454 (2006).

[9] G. Ehlers, A. A. Podlesnyak, J. L. Niedziela, E. B. Iverson, and P. E. Sokol, Rev. Sci. Instrum. **82**, 085108 (2011).

[10] G. E. Granroth, A. I. Kolesnikov, T. E. Sherline, J. P. Clancy, K. A. Ross, J. P. C. Ruff, B. D. Gaulin, and S. E. Nagler, J. Phys.: Conf. Series **251**, 012058 (2010).

[11] http://www.ncnr.nist.gov/instruments/dcs/PosterNov2002.pdf.

[12] J. Copley and J. Cook, Chem. Phys. **292**, 477 (2003).

[13] C. G. Windsor, *Pulsed Neutron Scattering* (Halsted Press, Wiley & Sons, New York, USA, 1981).

[14] http://neutrons.ornl.gov/facilities/SNS/works.shtml.

[15] R. Osborn, S. Rosenkranz, J. P. Castellan, F. Weber, D. Abernathy, and M. B. Stone, *Progress in Measuring S(Q,ω) in 4 Dimensions Using the Sweep Mode* (Talk presented at the American Conference on Neutron Scattering, Washington, DC, 2012).

Chapter 3

The Triangular Bilayer Spin Glass $LuCoGaO_4$

This chapter incorporates the preprint *"Neutron Scattering Studies on the Quasi-2D Triangular Bilayer Spin Glass $LuCoGaO_4$"*, which is intended for submission to Physical Review B.

This work presents the first time-of-flight neutron scattering study of the dilute antiferromagnetic triangular bilayer system $LuCoGaO_4$, which was grown for the first time as high-quality single crystal at McMaster University. Magnetization measurements revealed a pronounced ZFC/FC splitting of the magnetic susceptibility indicative of a spin glass transition at $T_g \sim 19$ K.

Our neutron scattering measurements allowed us to characterize the static and dynamic spin correlations in this spin glass over wide range of temperatures. In particular, we observe antiferromagnetic short-range two-dimensional correlations that extend over roughly five unit cells below the freezing temperature and a gapped, two-dimensional spin wave-like excitation at an energy of $\sim$12 meV.

3.1 Neutron Scattering Studies of the Quasi Two-Dimensional Antiferromagnetic Triangular Bilayer Spin Glass $LuCoGaO_4$

K. Fritsch,[1] K. A. Ross,[1,2,3] G. E. Granroth,[4] G. Ehlers,[4] H. M. L. Noad,[1] H. A. Dabkowska,[5] and B. D. Gaulin[1,5,6]

[1]*Department of Physics and Astronomy, McMaster University, Hamilton, Ontario, L8S 4M1, Canada*

[2]*Institute for Quantum Matter and Department of Physics and Astronomy, Johns Hopkins University, Baltimore, Maryland 21218, USA*

[3]*NIST Center for Neutron Research, NIST, Gaithersburg, Maryland 20899-8102, USA*

[4]*Quantum Condensed Matter Division, Oak Ridge National Laboratory, Oak Ridge, TN, 37831, USA*

[5]*Brockhouse Institute for Materials Research, Hamilton, Ontario, L8S 4M1, Canada*

[6]*Canadian Institute for Advanced Research, 180 Dundas St. W., Toronto, Ontario, M5G 1Z8, Canada*

Abstract

We present a single crystal time-of-flight neutron scattering study of the static and dynamic spin correlations in $LuCoGaO_4$, a quasi two-dimensional dilute triangular lattice antiferromagnetic spin glass material. This system is based on Co^{2+} ions that are randomly distributed on triangular bilayers within the $YbFe_2O_4$ type, hexagonal crystal structure. Antiferromagnetic short-range two-dimensional correlations at wave vectors $\mathbf{Q}=(1/3, 1/3, L)$ develop within the bilayers at temperatures as high as $|\Theta_{\rm CW}| \sim 100$ K and extend over roughly five unit cells at temperatures below $T_{\rm g} = 19$ K. These two-dimensional static

correlations are observed as diffuse rods of neutron scattering intensity along c^* and reveal a continuous spin freezing process in their energy dependence. Aside from exhibiting these typical spin glass characteristics, this insulating material reveals an unusual gapped magnetic "resonant" spin excitation at $E \sim$12 meV that is reminiscent of the magnetic spin excitations observed in metallic high temperature superconductors or heavy fermion systems. The temperature dependence of this two-dimensional excitation correlates with the evolution of the static correlations into the spin glass state ground state and can potentially be associated with a spin-wave-like excitation arising from the short-range correlated spin regions.

3.1.1 Introduction

Studies of quasi two-dimensional frustrated triangular lattice antiferromagnets have been of intense recent research interest due to their exotic low temperature magnetic properties, embedded within spin glass or spin liquid ground states which can arise in these systems.[1,2] Prominent experimental examples for such states based on two-dimensional frustrated triangular geometries include the site disordered $NiGa_2S_4$,[3] the anisotropic triangular lattice system Cs_2CuCl_4,[4,5] the honeycomb lattice-based system $Ba_3CuSb_2O_9$,[6] and the quantum spin liquid candidates κ-(BEDT-TTF)$_2$Cu$_2$(CN)$_3$[7] and herbertsmithite.[8] The dilute triangular lattice antiferromagnet bilayer system presented in this study serves as an important example in which the interplay of frustration and site disorder can be studied.[9] In $LuCoGaO_4$, the magnetic frustration is realized by antiferromagnetically coupled $S = 3/2$ magnetic mo-

ments on planar triangular bilayers (Fig. 3.1(a)). Site disorder arises from the fact that the Co^{2+} ions are statistically distributed in a 1:1 ratio with nonmagnetic Ga^{3+} ions within the bilayers. $LuCoGaO_4$ belongs to the family of materials with the RFe_2O_4 type structure (Fig. 3.1(a)) and has the composition $R^{3+}M^{2+}M^{3+}O_4$, in which R is a small rare-earth ion such as Yb^{3+}, Lu^{3+}, In^{3+} or Tm^{3+}, and in which the M^{2+} and M^{3+} ions are $3d$ transition metals such as Fe^{2+}, Fe^{3+}, Mn^{2+}, Mg^{2+}, Cu^{2+}, or Co^{2+} and Ga^{3+}. The M ions can either both be magnetic or can be a mixture of magnetic and nonmagnetic ions (dilute case). In addition, the R ion can also be magnetic or nonmagnetic, leading to complex magnetic and/or charge correlations.

The crystal structure, with space group $R\bar{3}m$, is characterized by transition metal ions that form double layers of $M^{3+}O_5$ triangular bipyramids that are connected by triangular layers of RO_6 octahedra, leading to quasi two-dimensional magnetic properties.

Several combinations of these materials with two different M distributed over the same crystallographic site, and which therefore are expected to display frustrated ordering, have been the focus of previous studies. Besides $LuCoGaO_4$, $LuCuGaO_4$, $LuMFeO_4$ (M=Zn, Fe, Co, Cu), $YbMFeO_4$ (M=Mg, Fe, Co, Cu), $YbCuGaO_4$ as well as $YbCoGaO_4$ have been studied.[9–20] In this series, the multiferroic $LuFe_2O_4$ has attracted particular interest due to the observed interplay of cation and magnetic ordering. This material exhibits two- or three-dimensional ferrimagnetic ordering below ∼240 K depending on oxygen stoichiometry,[21,22] and a charge-ordered state below ∼330 K which is thought to underlie the ferroelectricity.[23] The dilute case has been most ex-

tensively investigated for $LuFeMgO_4$.[13–15,17,18,24] $LuCuGaO_4$ has recently been shown to display spin liquid behavior with a gapless spin excitation spectrum down to 50 mK,[25] in contrast to previous expectations of spin glass behavior based on susceptibility measurements.[9] The effects of spin anisotropy on the phase transitions of $YbCoGaO_4$ and $LuCoGaO_4$ have very recently been investigated by Radelytskyi *et al.*.[26]

With the exception of RCuGaO$_4$ (R=Yb, Lu),[25] all other members of this series exhibit a splitting of field-cooled and zero-field-cooled susceptibilities, however on very different temperature scales. The majority of these materials shows no indication of magnetic long-range order, however diffuse magnetic scattering has been observed in neutron diffraction studies on (powder) YFe_2O_4,[10] (powder) $LuCuFeO_4$, (powder) $LuZnFeO_4$, (powder and single crystal) $LuFeMgO_4$[13] and (powder) $LuCoGaO_4$ as a broad peak around $|Q| \sim 1.27$ Å^{-1} at low temperature.

The study of this family of materials has been less comprehensive than it otherwise would have been due to the lack of large, high-quality single crystals. We recently succeeded in growing high-quality samples of $LuCoGaO_4$, for which our x-ray structural refinement shows random occupation of the triangular bilayers by Co^{2+} and Ga^{3+} in a 1:1 ratio, placing this material at the percolation threshold for triangular lattices of p_c=0.5.[27]

In our single crystal of $LuCoGaO_4$, the splitting of the field-cooled and zero-field-cooled susceptibilities occurs at $T_g \sim 19$ K, consistent with spin freezing or a spin glass transition. The determined Curie-Weiss temperature $\Theta_{CW} \sim -100$ K implies antiferromagnetic interactions between the Co^{2+} mo-

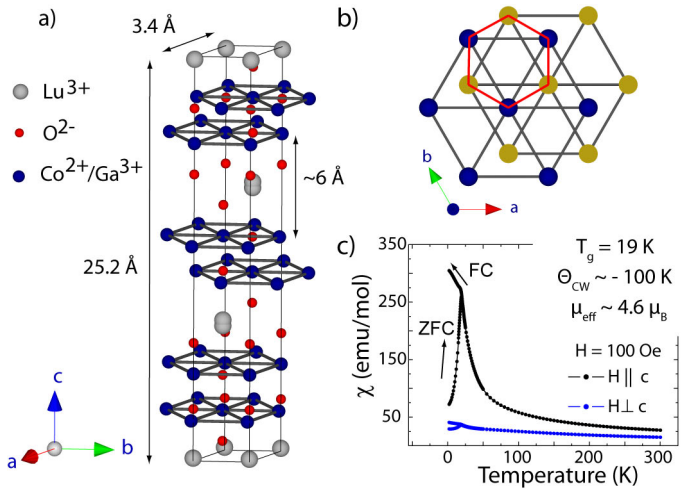

Figure 3.1: (a) Crystal structure of $LuCoGaO_4$ showing the rhombohedral unit cell and the planar triangular bilayers in which the $S = 3/2$ magnetic moments on the Co^{2+} ions are statistically distributed in a 1:1 ratio with nonmagnetic Ga^{3+} ions. The bilayers in the ab plane are well separated along the c axis by triangular layers composed of nonmagnetic LuO_6 octahedra. (b) The two faces of the bilayer shown in blue and orange as viewed down the c axis. Each face has triangular geometry on which the magnetic interactions will be highly frustrated. The two bilayer faces are staggered such that the shortest bonds form between the cations linking the two faces, thereby forming an undulating honeycomb lattice (shown in red). (c) Magnetic dc-susceptibility measured on a single crystal of $LuCoGa_4$ reveals spin glass behavior below the freezing temperature T_g ∼19 K.

ments. These moments are found in the $S = 3/2$ high-spin state based on an effective magnetic moment of $4.6\mu_B$. These results are consistent with previous data from Cava *et al.* obtained on powder samples.[9] The frustration index of $f \sim 5$ indicates moderate frustration. As shown in Fig. 3.1(c), the susceptibility is anisotropic with a large response for applied fields parallel to the stacking direction of the bilayers along the c axis. Interestingly, a cusp in the ZFC/FC curves is observed for both directions of the applied field, signaling a simultaneous freezing of the longitudinal and transverse spin components. This is in contrast to the behavior displayed by most other members of this

family, for example $LuFeMgO_4$ or $LuFeCoO_4$, in which only the longitudinal susceptibility displays freezing.[18,24] It is also different from $YbCoGaO_4$, which is considered an Ising spin glass.[26] It follows that the magnetic nature of the Co^{2+} ions in $LuCoGaO_4$ is Heisenberg-like with relatively strong uniaxial single ion anisotropy. Recent ac-susceptibility measurements[26] also show a frequency dependence for both field directions, and exhibit spin glass characteristics such as activated behavior in form of the Vogel-Fulcher law, possible dynamic scaling and a peak shift per decade frequency of $\sim$0.05, consistent with expectations for conventional spin glass behavior.[28]

3.1.2 Experimental details

A large, high-quality single crystal used for both neutron scattering measurements was, to our knowledge, recently grown for the first time at McMaster University using the optical floating zone technique.[29] For the crystal growth, the preannealed starting materials Lu_2O_3 and Ga_2O_3 were first mixed with CoO in the appropriate stoichiometric ratios, then hydrostatically pressed at 60 MPa and the resulting rods were subsequently sintered in air at 1300°C for 24 hours. The so obtained polycrystalline rods were used as seed and feed rods in the actual crystal growth, which for the crystal used in this study, was performed in a Crystal Systems Inc. floating zone furnace at a growth speed of $\sim$ 9 mm/hour.[30]

Magnetization measurements shown in Fig. 3.1(c) were performed using a conventional SQUID magnetometer at McMaster University. A small single crystal sample of mass $\sim$10 mg was cut from the main crystal growth and

aligned to within 3° for magnetization measurements with the magnetic field applied parallel or transverse to the plane of the bilayers. The neutron scattering experiments were carried out on a ∼5 cm long cylindrical single crystal sample of $LuCoGaO_4$ using the time-of-flight spectrometers SEQUOIA [31,32] and CNCS[33] at the SNS, ORNL. The sample was aligned in the $[H, H, L]$ horizontal scattering plane. SEQUOIA measurements employed an incident energy of $E_i = 35$ meV, spinning Fermi chopper 1 at 240 Hz and the bandwidth-limiting T_0 chopper at 60 Hz, giving an energy resolution of 1 meV. Data from CNCS were obtained using two settings of the incident energy E_i, 10 meV and 25 meV, resulting in energy resolutions of 0.3 meV and 1.0 meV, respectively. The sample was mounted in a standard Orange cryostat with a base temperature of ~ 1.5 K. Measurements were performed over a wide range of temperatures up to 300 K.

3.1.3 Static correlations

The static and dynamic correlations in $LuCoGaO_4$ have been studied using the time-of-flight neutron scattering instruments SEQUOIA and CNCS, which allow the simultaneous measurement of the four-dimensional dynamic structure factor $S(\mathbf{Q}, E)$ over a large range of reciprocal space in both horizontal and vertical directions. The evolution of the static correlations with temperature using SEQUOIA is shown in Fig. 3.2. In the top row, elastic diffuse scattering intensity (E=[-1,1] meV, [0,0,L]=$[-2.75, 2.75]$ r.l.u.) within the plane of the bilayers is clearly observed at wave vectors $\mathbf{Q} = (1/3, 1/3, L)$. This type of scattering has similarly been observed in single crystals and par-

ticularly in powder samples as a broad peak centered at $Q \sim 1.27$ Å^{-1} for several other members of the $YbFe_2O_4$ family.[10,13] It is typical for antiferromagnetically interacting moments in a triangular geometry and suggests a $\sqrt{3} \times \sqrt{3}$ structure. In the bottom row of Fig. 3.2, the elastic scattering in the $[H, H, L]$ plane is shown after integrating the data over the vertical $[H, -H, 0]$ direction. Here, the diffuse scattering is observed as rods of scattering, a clear signature of two-dimensional correlations in the a^*-b^* plane perpendicular to the rod direction. The extent of the rod-like scattering along $[0, 0, L]$ implies the absence of correlations between bilayers along $c*$ and therefore confirms the two-dimensional character of this system.

This elastic diffuse scattering is seen to persist up to at least 120 K, showing that the freezing process develops noticeably at temperatures as a high as the Curie Weiss temperature ($\Theta_{\mathrm{CW}} \sim -100$ K). The isotropic diffuse scattering profile can be well described by a Ornstein-Zernike (Lorentzian) lineshape at all temperatures, which allows us to extract the correlation length $\xi = 1/\mathrm{HWHM}$ in the plane of the bilayers as a function of temperature, as shown in Fig. 3.2 for SEQUOIA and CNCS data. For SEQUOIA data, longitudinal and transverse cuts through the elastic scattering (-1 meV $< E <$ 1 meV) through the six observed peak positions were fit to a Lorentzian lineshape. The elastic scattering was integrated along the length of the rod for $[0, 0, L] = [-2.75, 2.75]$ r.l.u.. The resulting correlation lengths were averaged and are shown in Fig. 3.3. For CNCS data, the elastic scattering intensity at $(-1/3, -1/3, L)$ for E_i=10 and 25 meV was integrated over $[0, 0, L] = [-2, 2]$ r.l.u. and $[0, 0, L] = [-0.25, 0.25]$ r.l.u., respectively, and again fit to a Lorentzian lineshape to extract the correlation length. The difference in absolute values of the correlation length is a

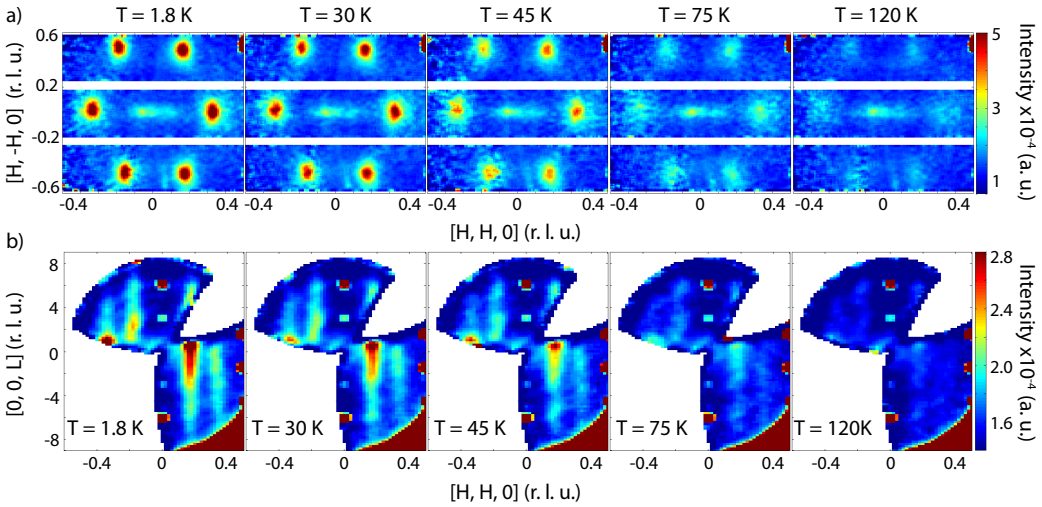

Figure 3.2: Elastic scattering maps $S(\mathbf{Q}, E = 0)$ as a function of temperature obtained on the fine resolution chopper spectrometer SEQUOIA show the short-range antiferromagnetic spin correlations as diffuse scattering intensity at wave vectors $\mathbf{Q}$=$(1/3, 1/3, L)$ in the plane of the bilayers (top row) and in the plane perpendicular to it (bottom row). Rods of neutron scattering intensity along the $[0, 0, L]$ direction (bottom row) indicate the absence of magnetic correlations along that direction and reveal the two-dimensional character of the magnetic interactions in the bilayer planes. It is seen that short-range correlations begin to develop at $T \sim |\Theta_{\rm CW}|$ and gradually evolve into the low temperature glass phase, without going through a conventional phase transition. The data have been corrected for detector efficiency only.

result of the coarser $\mathbf{Q}$-resolution at higher incident energy and of the different binning range in the $[0, 0, L]$ direction.

These two independent measurements are consistent and reveal qualitatively identical behavior, showing a strong build-up of the magnetic correlations below 100 K and a rather gradual increase of the correlation length from 30 K towards its saturation value of $\xi \sim 6.5 - 7.5$ Å below the freezing temperature $T_{\rm g} \sim 19$ K (indicated by an arrow in Fig. 3.2). This correlation length implies a correlated regions of spins of ~ 16 Å or roughly 5 unit cells.

It is noteworthy that no sharp anomaly is observed at T_g, in contrast to the ZFC/FC susceptibility which displays a clear cusp at the freezing temperature. This feature appears to be common to all spin glass materials in this family.

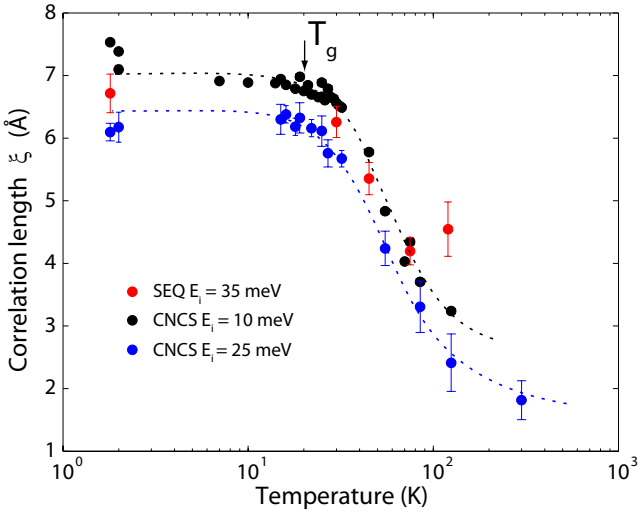

Figure 3.3: The correlation length within the plane of the bilayers extracted from cuts through the elastic scattering at $\mathbf{Q}$=$(1/3, 1/3, L)$ for both SEQUOIA and CNCS data. The short-range spin correlations gradually develop at temperatures as high as the Curie Weiss temperature at $\sim$ 100 K and increase to their maximum value of $\xi \sim 6.5 - 7.5$ Å below the freezing temperature T_g. There is no sharp anomaly at T_g in contrast to the observed cusp in the ZFC susceptibilty, typical for this family of materials. Note that the difference in absolute values of the correlation length from CNCS data for E_i = 10 and 25 meV is a result of the coarser $\mathbf{Q}$-resolution at higher incident energy and a different binning range in L. For details of the fitting, see text. The error bars are $\pm 1\sigma$.

An alternative method of extracting an approximate correlation length was proposed by Wiedenmann *et al.* who fitted powder data of $LuFeMgO_4$ to a

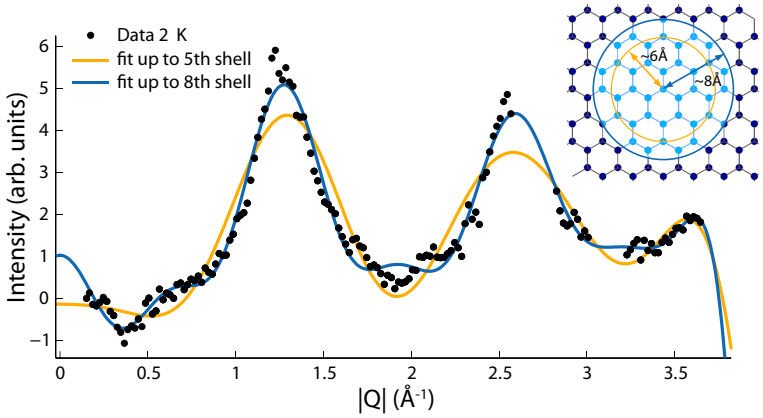

Figure 3.4: Powder-averaged data of $LuCoGaO_4$ at $T = 1.8$ K as measured on CNCS with $E_i = 10$ meV. Fits to Eqn. 3.1 show good agreement with short-range two-dimensional magnetic correlations extending beyond the 5th nearest neighbor shell at ~ 6 Å. The best fit to the data is obtained including magnetic correlations extending up to the 8th nearest neighbor shell at ~ 8 Å, fully consistent with the correlation length determined from the lineshape analysis in Fig. 3.2. The 300 K data set has been subtracted from the data as paramagnetic background. The top right figure illustrates how the magnetic correlations are built up in the quasi two-dimensional shell model.[13]

model of short-range, quasi two-dimensional correlations using the following expression for the scattering neutron intensity $I(Q)$:[13]

$$I\left(Q\right) \propto f^2\left(Q\right) \times \sum_l c_l \left[a_l \frac{\sin(Qr_l)}{Qr_l} + b_l \left(\frac{\sin(Qr_l)}{(Qr_l)^3} - \frac{\cos(Qr_l)}{(Qr_l)^2} \right) \right]. \qquad (3.1)$$

where $f^2\left(Q\right)$ is the form factor, c_l is the number of spins connected to a given spin l at distance r_l, and the a_l and b_l are coefficients describing correlations between spins. In this model, spin correlations build up for successive nearest neighbor shells within the triangular bilayer, assuming that no correlations between adjacent bilayers are formed. The fitting results to Eqn. 3.1 for powder-averaged CNCS data at 1.8 K using E_i=10 meV are shown in Fig. 3.4 for correlations within two shell radii, $r_5 = 5.89$ Å and $r_8 = 8.21$ Å (see small

figure on top right of Fig. 3.4). The data are best described by including spins correlated at distances up to the 8th neighbor shell at $\sim$ 8 Å, which is fully consistent with the above determined correlation length of $\sim$7.5 Å at 1.8 K.

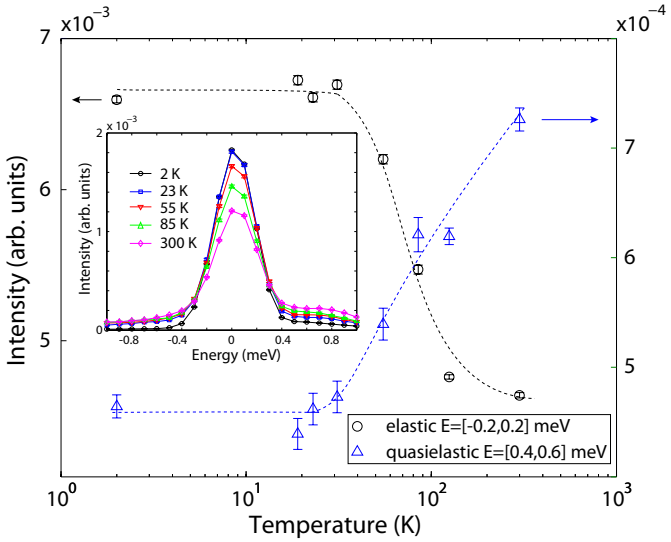

Figure 3.5: Energy dependence of the diffuse scattering as measured on CNCS with $E_i = 10$ meV. The temperature evolution of the scattering intensity at the elastic line $-0.2 < E < 0.2$ meV is contrasted to that at the quasielastic position ($0.4< E < 0.6$ meV). The observed behavior is consistent with a continuous freezing process on cooling and slowly fluctuating spin correlations that freeze out below $\sim T_g$. The inset shows representative cuts. Error bars are $\pm 1\sigma$.

The freezing process can be characterized by examining the energy dependence of the diffuse scattering peaks. For that purpose, we have taken cuts in energy through the diffuse peaks in our high resolution CNCS data ($E_i = 10$ meV) by integrating in $[H, H, 0] = [-0.5, -0.16]$ and $L = [-0.5, 0.5]$ r.l.u. Fits to a Lorentzian lineshape did not prove to be useful due to a small temperature-independent quasielastic feature at $\sim$0.8 meV that did not reproduce in higher-resolution scans, so we parametrize the energy dependence

by looking at the evolution of the scattering intensities at the elastic (-0.2 $< E <$ 0.2 meV) and the low-energy quasielastic (0.4 $< E <$ 0.6 meV) positions. The results are shown in Fig.3.5. One can clearly see the build-up of scattering intensity at the elastic position over a wide range of temperatures that reaches a constant value below $\sim T_{\mathrm{g}}$. Simultaneously, the weaker quasielastic scattering reveals a gradual decrease in intensity as the system is cooled down to $\sim T_{\mathrm{g}}$. Both the build-up of elastic and the simultaneous decrease in quasielastic scattering intensity can be associated with a freezing of spin fluctuations that would result in a sharpening of the diffuse peak in energy. This is shown in the inset of Fig. 3.5 for a subset of scans at representative temperatures. The fact that this scattering does not change below $\sim T_{\mathrm{g}}$ and that the peaks appear resolution-limited furthermore indicates that the spins are frozen on the time scale of this measurement, $\sim \tau \leq 10^{-10}$ s, at temperatures below T_{g}. This slowing down of spin fluctuations over a wide range of temperatures is typical of conventional spin glass behavior.[28]

3.1.4 Dynamic correlations

Using the time-of-flight neutron scattering technique allowed us to study the inelastic scattering spectrum of $LuCoGaO_4$. To our knowledge, only the magnetically ordered $LuFe_2O_4$[34] (single crystal) and, recently, the spin liquid material $LuCuGaO_4$[25] (powder) have been investigated in detail by inelastic neutron scattering over a wide range of $\mathbf{Q}$-E space.

The magnetic excitation spectrum at 1.8 K using SEQUOIA is shown in Fig. 3.6(a) for scattering as a function of momentum $[H, H, 0]$. For this mea-

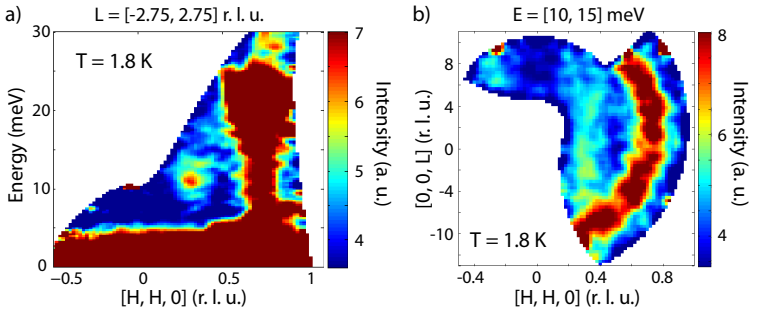

Figure 3.6: Two-dimensional spin excitation spectrum observed on SEQUOIA at 1.8 K. (a) Inelastic scattering integrated over $L = [-2.75, 2.75]$ and $[H, -H, 0] = [-0.2, 0.2]$ r.l.u. is shown. A gapped spin excitation positioned at $\mathbf{Q} = (1/3, 1/3, L)$ is observed at ∼12 meV. It has a bandwidth of ∼ 8 meV. Note the strong scattering intensity at higher $\mathbf{Q} \sim [0.7, 0.7, 0]$ r.l.u. that extends up in energy transfer up to ∼ 25 meV, which is associated to scattering from Al sample environment and the Al phonon density of states. (b) Constant energy slice within the $[H, H, L]$ scattering plane, integrated from $E = [10, 15]$ meV. The spin excitation is well localized and has two-dimensional, rod-like character, positioned at $\mathbf{Q} = (1/3, 1/3, L)$. Its $\mathbf{Q}$-width is comparable to the width of the diffuse elastic scattering.

surement, we integrated over $L = [-2.75, 2.75]$ and $[H, -H, 0] = [-0.2, 0.2]$ r.l.u.. We clearly observe a "resonant" magnetic excitation, that appears at wave vector $\mathbf{Q} = (1/3, 1/3, L)$ centered an energy of ∼12 meV, gapped by ∼9 meV from the elastic line. The excitation has a large bandwidth of ∼8 meV and appears to be dispersionless. Panel (b) shows a constant energy slice within the $[H, H, L]$ plane for$[H, -H, 0] = [-0.2, 0.2]$ r.l.u. and $E = [10, 15]$ meV that reveals the two-dimensional character of the excitation, that appears as inelastic rod of scattering along the $[0, 0, L]$ direction at both $\mathbf{Q} = (-1/3, -1/3, L)$ and $\mathbf{Q} = (1/3, 1/3, L)$.

A similar resonant feature has been observed in the layered iron pnictide superconductors[35,36] as well as in certain heavy fermion compounds.[37,38],

however, to our knowledge, this is the first time such an excitation has been observed in an *insulating* magnetic material.

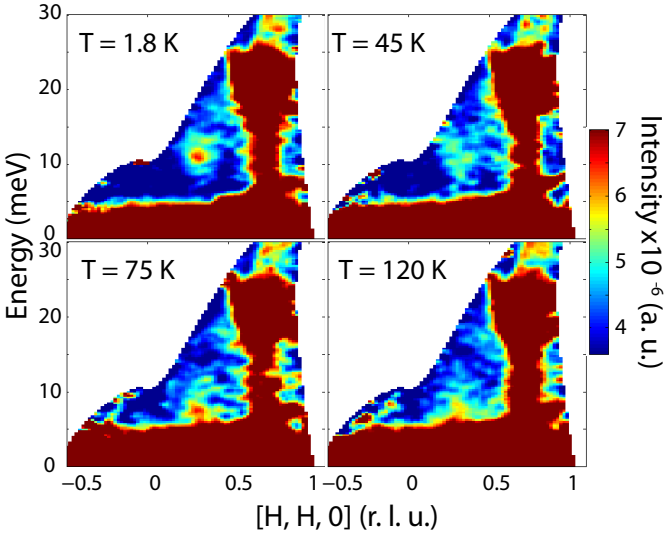

Figure 3.7: Temperature evolution of the magnetic excitation from SEQUOIA. Inelastic scattering intensity using an integration range of $L = [-2.75, 2.75]$ and $[H, -H, 0] = [-0.2, 0.2]$ r.l.u. is shown for selected temperatures of $T = 1.8$ K, $T = 45$ K, $T = 75$ K, and $T = 120$ K. A spin gap of $\sim$9 meV gradually opens below $\sim$ 85 K.

We present the temperature evolution of this scattering as observed on SEQUOIA in Fig. 3.7. With increasing temperature, the excitation is fairly temperature independent up to $\sim$ 45 K and then starts to soften at a temperature scale $\sim \Theta_{\mathrm{CW}}/2$. It collapses by $\sim$ 120 K at the wave vector $\mathbf{Q} = (1/3, 1/3, L)$. Figure 3.8 shows the same scattering as obtained on CNCS for finer temperature steps, allowing us to characterize the scattering in a more quantitative fashion. However, some conclusions can already be drawn from slices of inelastic scattering, for example, the temperature at which the gap develops can be estimated to be around $T \sim$85 K. We present cuts through the inelastic spectrum in Fig. 3.9 in the top panel. In the bottom panel of Fig. 3.9, we show

the temperature dependence of integrated intensities at two different energy transfers that characterize the evolution of the gap ($E = [3.25, 6.75]$ meV and the build-up of the magnetic excitation at 12 meV ($E = [8.25, 16.75]$ meV).

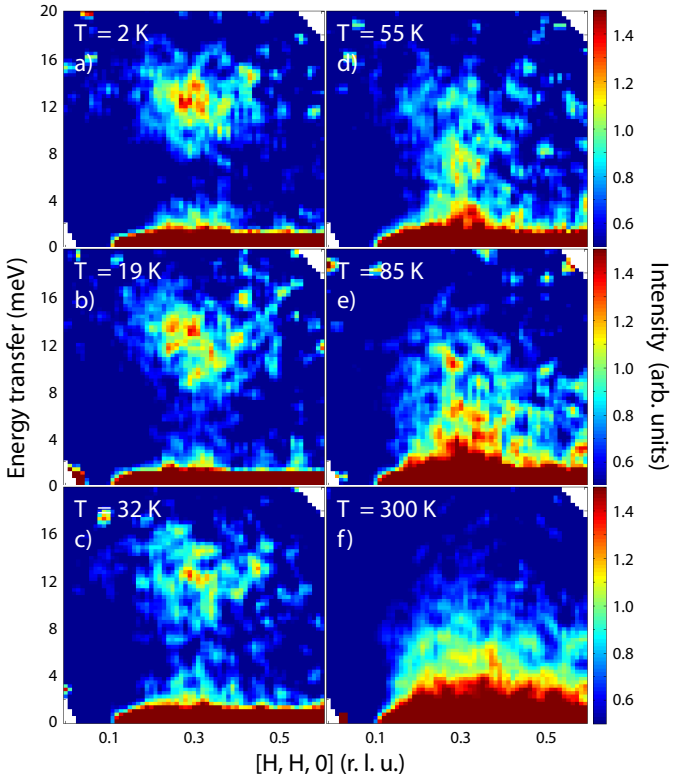

Figure 3.8: Temperature evolution of the magnetic excitation from CNCS. Inelastic scattering intensity for an integration range of $L = [-2, 13]$ r.l.u. and $[H, -H, 0] = [-0.2, 0.2]$ r.l.u. is shown for (a), $T = 2$ K, (b) $T = 19$ K, (c) $T = 32$ K, (d) $T = 55$ K, (e) $T = 85$ K, and (f) $T = 300$ K. A spin gap of ∼9 meV gradually opens below ∼85 K and is fully developed below the freezing temperature $T_g \sim 19$ K. The gap correlates with the short-range static spin correlations shown as in Figs. 3.2 and 3.3. Note that the data has been corrected for detector efficiency only.

The behavior clearly correlates with the development of the static correlations, as shown in Fig. 3.3. An onset of the static (short-range diffuse scattering) and dynamic correlations (resonant spin excitation) is observed at

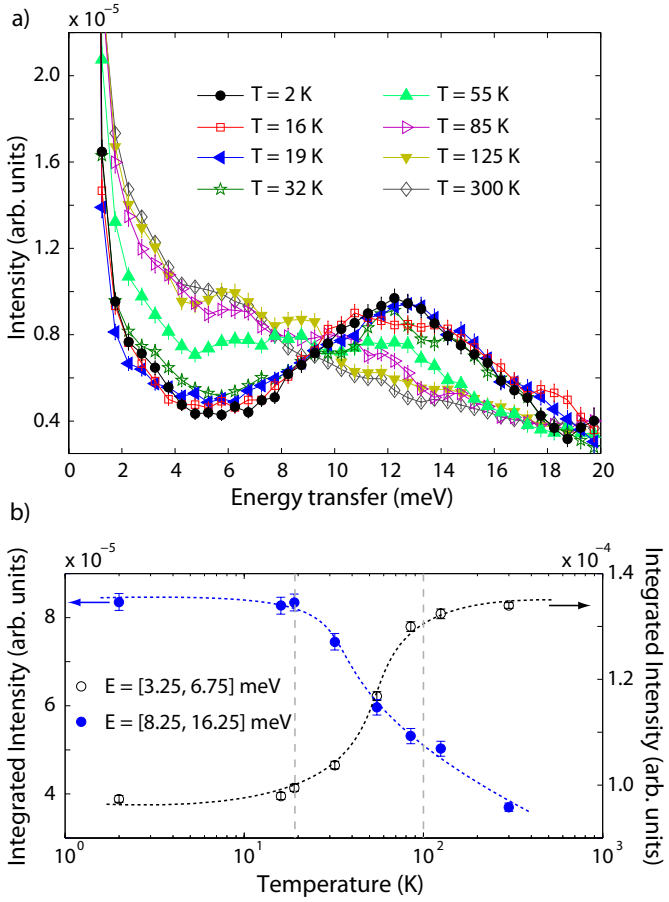

Figure 3.9: (a) Neutron scattering intensity vs energy transfer for various temperatures shown for $[0, 0, L] = [-2, 13]$ r.l.u. and $[H, H, 0] = [0.1, 0.5]$ r.l.u., using CNCS. (b) Temperature dependence of the integrated scattering intensity associated with the formation of the spin gap at $E = [3.25, 6.75]$ meV (black curve), and integrated intensity at the excitation $E = [8.25, 16.75]$ meV (blue curve), are shown to characterize the magnetic excitation in Figs. 3.8 and 3.9(a). The spin gap and the related spin excitation at 12 meV start to form below $|\Theta_{\rm CW}| \sim 85$ K and appear to be fully developed below $T_{\rm g}$, consistent with the evolution of the static spin correlations.

relatively high temperatures just around Θ_{CW}, followed by a dramatic build-up in correlations down to temperatures in the vicinity of the freezing temperature T_{g} at 19 K, below which both static and dynamic correlations are fully developed.

The observation of such a localized (in energy and wave vector) excitation at relatively large energy transfers raises the question about its origin. Reports of spin waves in spin glasses in the literature are quite rare.[39–42] For example, in the diluted uniaxial spin glass system $Fe_{1-x}Mg_xCl_2$, for a specific range of doping, broad spin wave features have been observed for wavelengths smaller than the correlation length. In addition, Wong *et al.* report long wavelength spin waves at considerably lower frequencies that they explained as being due to the precession of spin clusters around the easy axis at an energy determined by the anisotropy field. This low frequency precession is possible as the transverse spin components in $Fe_{1-x}Mg_xCl_2$ do not freeze - different from what we observe in $LuCoGaO_4$. However, their report of broad spin wave features for $\lambda < \xi$ - akin to cluster modes - is possibly in agreement with our measurements. Such modes have also been reported for the quasi two-dimensional XY system $Rb_2Mn_xCr_{1-x}Cl_4$.[42] The energy scale of our excitation can be understood in terms of the single ion anisotropy (taken as $A = \chi_{\parallel} - \chi_{\perp}$), which displays a similar temperature dependence as the energy gap in our sample.

The fact that the excitation, at low temperatures where it is well developed, seems to be localized in reciprocal space, may be understood as a consequence of the gapped spin excitation spectrum in combination with the relatively short correlation length below T_{g}. The short correlation length can be thought of as

giving a zone centre which is only defined to $\frac{1}{\xi}$. The superposition of gapped spin wave bands over this "effective" zone center will show strong scattering near the minimum of the band, where the dispersion is flat, but weak, or unobservable inelastic intensity away from the "effective" zone centre, where the spin excitations are dispersive.

3.1.5 Conclusion

We performed the first time-of-flight neutron scattering measurements on the triangular bilayer spin glass $LuCoGaO_4$ over a wide range of temperatures in zero field. We observe diffuse elastic scattering at wave vectors $\mathbf{Q}=(1/3, 1/3, L)$ that appear as rods of scattering along the c^*-direction. This is consistent with short-range antiferromagnetic correlations with a correlation length $\xi \sim 6.5 - 7.5$ Å within decoupled bilayers in the a^*b^* plane, confirming the two-dimensional character of this system. The energy dependence of this diffuse scattering exhibits slowing down of the spin fluctuations in a manner consistent with a typical spin glass freezing process. These features are consistent with expectations for a conventional two-dimensional spin glass. In addition, we observe a rather unusual magnetic excitation which consists of a well localized, "resonant" gapped ∼12 meV spin excitation in our inelastic neutron scattering data. This excitation is reminiscent of that observed in high temperature superconducting materials or certain heavy fermion compounds, however, $LuCoGaO_4$ is an *insulating* material therefore the underlying mechanism must be different. One can speculate that this excitation results from the combination of a gapped spin wave band and short-range spin correlations at

low temperatures. The temperature dependence of the gap evolves similarly to the anisotropy determined from magnetization measurements.

Work at McMaster University was supported by NSERC of Canada. The research at Oak Ridge National Laboratory's Spallation Neutron Source was sponsored by the Scientific User Facilities Division, Office of Basic Energy Sciences, U.S. Department of Energy. The data were reduced using Mantid[43] and analysed using the HORACE software package.[44] The powder average of the single crystal data was performed in DAVE.[45]

3.2 * References

[1] C. Lacroix, P. Mendels, and F. Mila, in *Introduction to Frustrated Magnetism* (Springer Series in Solid-State Sciences, Heidelberg, 2011).

[2] L. Balents, Nature **464**, 199 (2010).

[3] S. Nakatsuji, Y. Nambu, H. Tonomura, O. Sakai, S. Jonas, C. Broholm, H. Tsunetsugu, Y. Qiu, and Y. Maeno, Science **309**, 1697 (2005).

[4] R. Coldea, D. A. Tennant, and Z. Tylczynski, Phys. Rev. B **68**, 134424 (2003).

[5] R. Coldea, D. A. Tennant, A. M. Tsvelik, and Z. Tylczynski, Phys. Rev. Lett. **86**, 1335 (2001).

[6] S. Nakatsuji, K. Kuga, K. Kimura, R. Satake, N. Katayama, E. Nishibori, H. Sawa, R. Ishii, M. Hagiwara, F. Bridges, T. U. Ito, W. Higemoto, Y. Karaki, M. Halim, A. A. Nugroho, J. A. Rodriguez-Rivera, M. A. Green, and C. Broholm, Science **336**, 559 (2012).

[7] Y. Shimizu, K. Miyagawa, K. Kanoda, M. Maesato, and G. Saito, Phys. Rev. Lett. **91**, 107001 (2003).

[8] J. S. Helton, K. Matan, M. P. Shores, E. A. Nytko, B. M. Bartlett, Y. Yoshida, Y. Takano, A. Suslov, Y. Qiu, J.-H. Chung, D. G. Nocera, and Y. S. Lee, Phys. Rev. Lett. **98**, 107204 (2007).

[9] R. Cava, A. Ramirez, Q. Huang, and J. Krajewski, J. Solid State Chem. **140**, 337 (1998).

[10] S. Katano, T. Matsumoto, S. Funahashi, J. Iida, M. Tanaka, and J. Cable, Physica B: Condens. Matter **213-214**, 218 (1995).

[11] K. Yoshii, N. Ikeda, Y. Matsuo, Y. Horibe, and S. Mori, Phys. Rev. B **76**, (2007).

[12] K. Yoshii, N. Ikeda, Y. Okajima, Y. Yoneda, Y. Matsuo, Y. Horibe, and S. Mori, Inorg. Chem. **47**, 6493 (2008).

[13] A. Wiedenmann, W. Gunsser, J. Rossat-Mignod, and M. Evrard, J. Magn. Magn. Mater. **31-34**, 1442 (1983).

[14] N. Ikeda, K. Kohn, E. Himoto, and M. Tanaka, J. Phys. Soc. Jpn. **64**, 4371 (1995).

[15] M. Tanaka, E. Himoto, and Y. Todate, J. Phys. Soc. Jpn. **64**, 2621 (1995).

[16] M. Tanaka, H. Iwasaki, K. Siratori, and I. Shindo, J. Phys. Soc. Jpn. **58**, 1433 (1989).

[17] Y. Todate, C. Kikuta, E. Himoto, M. Tanaka, and J. Suzuki, J. Phys.: Condens. Matter **10**, 4057 (1998).

[18] Y. Todate, E. Himoto, C. Kikuta, M. Tanaka, and J. Suzuki, Phys. Rev. B **57**, 485 (1998).

[19] H. A. Dabkowska, A. Dabkowski, G. M. Luke, and B. D. Gaulin, J. Cryst. Growth **234**, 411 (2002).

[20] R. Szymczak, H. A. Dabkowska, A. Dabkowski, G. M. Luke, P. Aleshkevych, J. Fink-Finowicki, and H. Szymczak, J. Phys.: Conf. Series **303**, 012064 (2011).

[21] J. Iida, M. Tanaka, Y. Nakagawa, S. Funahashi, N. Kimizuka, and S. Takekawa, J. Phys. Soc. Jpn. **62**, 1723 (1993).

[22] A. Christianson, M. Lumsden, M. Angst, Z. Yamani, W. Tian, R. Jin, E. Payzant, S. Nagler, B. Sales, and D. Mandrus, Phys. Rev. Lett. **100**, (2008).

[23] N. Ikeda, H. Ohsumi, K. Ohwada, K. Ishii, T. Inami, K. Kakurai, Y. Murakami, K. Yoshii, S. Mori, Y. Horibe, and et al., Nature **436**, 1136 (2005).

[24] T. Sunaga, M. Tanaka, N. Sakai, and Y. Tsunoda, J. Phys. Soc. Jpn. **70**, 3713 (2001).

[25] S. Calder, S. Giblin, D. Parker, P. Deen, C. Ritter, J. Stewart, S. Rols, and T. Fennell, arXiv:1002.0975v2 [cond-mat.mtrl-sci] (2010).

[26] I. Radelytskyi and R. Szymczak, private communication, 2013.

[27] M. F. Sykes and J. W. Essam, J. Math. Phys. **5**, 1117 (1964).

[28] J. A. Mydosh, *Spin Glasses: An Experimental Introduction* (CRC Press, Bristol, PA, 1993).

[29] H. A. Dabkowska and A. B. Dabkowski, in *Crystal Growth of Oxides by Optical Floating Zone Technique. Experimental Approach to Defects De-*

termination (Springer Handbook of Crystal Growth, Defects and Characterization, Berlin, Heidelberg, New York, Tokyo, 2010), pp. 367–392.

[30] H. M. L. Noad, H. A. Dabkowska, and G. M. Luke, manuscript in preparation.

[31] G. Granroth, D. Vandergriff, and S. Nagler, Physica B: Condens. Matter **385-386**, 1104 (2006).

[32] G. E. Granroth, A. I. Kolesnikov, T. E. Sherline, J. P. Clancy, K. A. Ross, J. P. C. Ruff, B. D. Gaulin, and S. E. Nagler, J. Phys.: Conf. Series **251**, 012058 (2010).

[33] G. Ehlers, A. A. Podlesnyak, J. L. Niedziela, E. B. Iverson, and P. E. Sokol, Rev. Sci. Instrum. **82**, 085108 (2011).

[34] H. J. Lewtas, Ph.D. thesis, Oxford University (2010).

[35] A. D. Christianson, E. A. Goremychkin, R. Osborn, S. Rosenkranz, M. D. Lumsden, C. D. Malliakas, I. S. Todorov, H. Claus, D. Y. Chung, and M. G. Kanatzidis, Nature **456**, 930 (2008).

[36] M. D. Lumsden, A. D. Christianson, D. Parshall, M. B. Stone, S. E. Nagler, G. J. MacDougall, H. A. Mook, K. Lokshin, T. Egami, D. L. Abernathy, E. A. Goremychkin, R. Osborn, M. A. McGuire, A. S. Sefat, R. Jin, B. C. Sales, and D. Mandrus, Phys. Rev. Lett. **102**, 107005 (2009).

[37] G. Friemel, Y. Li, A. Dukhnenko, N. Shitsevalova, N. Sluchanko, A. Ivanov, V. Filipov, B. Keimer, and D. Inosov, Nat. Commun. **3**, 830 (2012).

[38] C. Stock, C. Broholm, J. Hudis, H. J. Kang, and C. Petrovic, Phys. Rev. Lett. **100**, 087001 (2008).

[39] P.-Z. Wong, H. Yoshizawa, S. Shapiro, J. Mydosh, J. van den Berg, and T. Palstra, Phys. Rev. Lett. **58**, 1276 (1987).

[40] P.-Z. Wong, H. Yoshizawa, and S. M. Shapiro, J. Appl. Phys. **61**, 4077 (1987).

[41] D. Sieger, H. Tietze, R. Geick, S. Bates, R. Cowley, W. Treutmann, and U. Steigenberger, Solid State Commun. **60**, 847 (1986).

[42] D. Sieger, H. Tietze, R. Geick, P. Schweiss, G. Heger, and W. Treutmann, J. Appl. Phys. **63**, 3729 (1988).

[43] http://www.mantidproject.org/ (2012).

[44] T. G. Perring, R. A. Ewings, and J. V. Duijn, http://horace.isis.rl.ac.uk, and unpublished (2009).

[45] R. T. Azuah, L. R. Kneller, Y. Qiu, P. L. W. Tregenna-Piggott, C. M. Brown, J. R. D. Copley, and R. M. Dimeo, J. Res. Natl. Inst. Stan. Technol. **114**, 341 (2009).

Chapter 4

The Kagome Staircase Material $Co_3V_2O_8$

This chapter contains three research articles on different aspects of the kagome staircase material $Co_3V_2O_8$ and is divided in three sections as follows.

The first section incorporates the article *"Crystal Growth and Characterization of the Magnetically Dilute Kagome Staircase System $(Co_{1-x}Mg_x)_3V_2O_8$"*, which has been published in Journal of Crystal Growth. The full reference is given below:

K. Fritsch, M. Ramazanoglu, H.A. Dabkowska, and B.D. Gaulin. Journal of Crystal Growth, **327**, 205 (2011).*

Figures 4.1-4.5, as well as tables 4.1 and 4.2 are reproduced from that article with permission.

This work showed that high-quality single crystals of $(Co_{1-x}Mg_x)_3V_2O_8$ could be grown. A structural refinement further revealed almost random sub-

* ©(2011) Elsevier B.V.

stitution of the Mg^{2+} ions at the Co^{2+} sites with slight preference for the Mg to occupy the less symmetric spine site.

Following this work, detailed neutron scattering measurements on two of these magnetically dilute single crystals as well as a detailed study of the magnetic phase diagram as a function of doping concentration based on magnetization measurements on polycrystalline $(Co_{1-x}Mg_x)_3V_2O_8$ have been performed and are presented in Section 4.2.

This second section consists of the article *"Magnetic Order and Fluctuations in the Presence of Quenched Disorder in the Kagome Staircase System $(Co_{1-x}Mg_x)_3V_2O_8$"*, which has been published in Physical Review B. The full reference is given below:

K. Fritsch, Z. Yamani, S. Chang, Y. Qiu, J.R.D. Copley, M. Ramazanoglu, H.A. Dabkowska, and B.D. Gaulin. Physical Review B, **86**, 174421 (2012).[†]

Figures 4.6-4.18 are reproduced from the above article with permission.

The magnetic phase diagram obtained from magnetization measurements revealed a strong sensitivity of $(Co_{1-x}Mg_x)_3V_2O_8$ to disorder, in which a dilution level of only 19% was sufficient to suppress any long-range order down to below 1.5 K. The elastic and inelastic neutron scattering measurements we performed were in agreement with this picture, showing the existence of short-range order in the form of diffuse elastic scattering that could be related to a correlated region of spins of ~ 25 Å in diameter, and corresponding short-range spin excitations in the form of broad diffuse spin waves with a finite lifetime. As a further important result of this paper, we present a two-

[†] ©(2011) The American Physical Society

dimensional percolation model that is able to explain the magnetic response of $(Co_{1-x}Mg_x)_3V_2O_8$ to quenched nonmagnetic disorder by means of combined site and bond percolation appropriate to the random disorder and the absence of significant spine-spine exchange interactions. This model predicts a zero-temperature percolation threshold for a Mg concentration of $x = 0.26$, in agreement with our phase diagram that extrapolates the suppression of long-range magnetic order to zero temperature at just that doping concentration. We were therefore able to show that $Co_3V_2O_8$ can effectively be approximated as a two-dimensional system.

The last section in this chapter incorporates the preprint *"Quantum Fluctuations in the Kagome Staircase System $Co_3V_2O_8$ in a Transverse Magnetic Field"*, which is intended for publication in Physical Review B.

This paper describes magnetization measurements as well as a very comprehensive set of elastic and inelastic neutron scattering measurements of $Co_3V_2O_8$ in a transverse magnetic field. This magnetic field, which is applied transverse to the easy axis of the ferromagnetically coupled spins, perpendicular to the stacking direction of the kagome layers, is shown to introduce quantum fluctuations that lead to quantum phase transitions at 6.25, 7 and 13 T, which are associated with changes in the magnetic structure and in the magnetic excitation spectrum. While it is at present not clear how the low-temperature high-field "quantum paramagnetic" phase for $\mu_0 H > 13$ T connects to the zero-field high-temperature "thermal paramagnet", be it through a crossover or a real thermodynamic phase transition at intermediate temperatures, these measurements are an important contribution to the field of

quantum criticality, showing for the first time the realization of quantum phase transitions induced by a transverse field in a quasi two-dimensional system. What is more, our measured spin wave spectra should enable a motivated theorist to put forward a microscopic description of the magnetic interactions in the system, ie. a Hamiltonian relevant to $Co_3V_2O_8$, for at least the zero-field and the high-field phases.

4.1 Crystal Growth and Characterization of the Magnetically Dilute Kagome Staircase System $(Co_{1-x}Mg_x)_3V_2O_8$

K. Fritsch,[1] M. Ramazanoglu,[1] H. A. Dabkowska,[5] and B. D. Gaulin[1,5,6]

[1] *Department of Physics and Astronomy, McMaster University, Hamilton, Ontario, L8S 4M1, Canada*

[5] *Brockhouse Institute for Materials Research, Hamilton, Ontario, L8S 4M1, Canada*

[6] *Canadian Institute for Advanced Research, 180 Dundas St. W., Toronto, Ontario, M5G 1Z8, Canada*

Abstract

High-quality single crystals of the magnetically dilute kagome staircase system $(Co_{1-x}Mg_x)_3V_2O_8$ ($x = 0.029(3)$ and $x = 0.194(4)$) have been grown by the optical floating zone technique. A pure $Co_3V_2O_8$ single crystal was used as seed material in the growth process. The crystals obtained were characterized by X-ray diffraction (XRD) and refined in space group *Cmca*. Single crystal refinement shows preferential substitution of the Mg ions at the Co(2) site. Magnetization measurements show a drastic suppression of the ferromagnetic transition temperature of $T = 6.1$ K observed in the pure material, attributed to the dilution with non-magnetic Mg ions.

The kagome staircase $M_3V_2O_8$ oxides (M = Ni, Co, Cu, Mn) have recently generated considerable interest because of their magnetic and magnetoelectric properties at low temperatures.[1–4] Their crystal structure differs from the well known two-dimensional, flat, kagome lattice in that the kagome layers containing the magnetic M^{2+} ions are buckled in and out of the kagome plane. This property partially relieves the geometric frustration and allows for several incommensurate long range ordered magnetic phases at low temperatures in the case of $Ni_3V_2O_8$ (which possesses antiferromagnetic kagome-plane exchange).[2] The isostructural compound $Co_3V_2O_8$ displays predominantly ferromagnetic coupling within the kagome planes, and exhibits a complex series of incommensurate and commensurate antiferromagnetic phases below $T \sim 11$ K that culminate in a simple ferromagnetic long range ordered ground state for $T < T \sim 6.1$ K.[3,5]

In $Co_3V_2O_8$, the kagome staircase structure is characterized by edge-sharing $M^{2+}O_6$ octahedra (shown in red and blue in Fig. 4.1(a) that are situated slightly above and below the a-c plane to form the kagome staircase. These buckled layers are stacked along the crystallographic b-axis, separated by nonmagnetic $V^{5+}O_4$ tetrahedra (shown in pink). The kagome layers within the a-c plane (Fig. 4.1 (b) are composed of $S = 3/2$ magnetic moments that reside on two crystallographically inequivalent Co^{2+} sites; high-symmetry crystallographic (4a) cross-tie sites (red) link the less symmetric (8e) spine sites (blue) that form chains along the a-axis.

In this work, we report the growth of very high-quality Mg-doped $Co_3V_2O_8$ (CVO) crystals by the optical floating zone technique, using a pure CVO

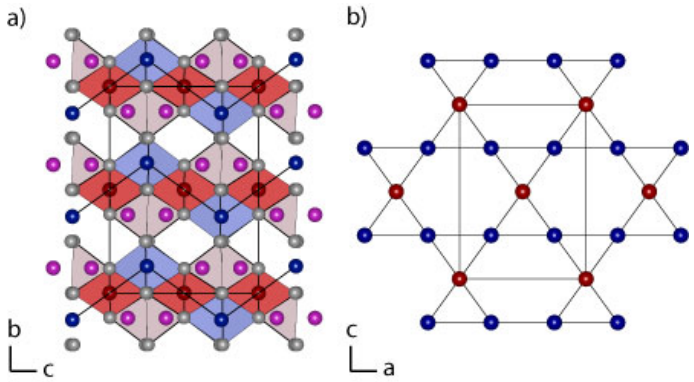

Figure 4.1: Crystal structure of $Co_3V_2O_8$. (a) View of the kagome staircase formed by $Co^{2+}O_6$ octahedra (red and blue), stacked along the b-axis separated by non-magnetic $V^{5+}O_4$ tetrahedra (pink). (b) View of the kagome plane projected on the ac plane with the crystallographically inequivalent cross-tie (red) and spine sites (blue).

crystal as seed for the growth. We discuss the basic structural and magnetic properties of the magnetically dilute Mg-CVO crystals.

CoO (99.999%, Alfa Aesar), MgO ($\geq$ 99.6%, Fisher Scientific Company) and V_2O_5 (99.9%, CERAC) were used as starting materials for the preparation of feed rods. The MgO powder was pre-annealed at 1000°C before mixing it with CoO and V_2O_5 (pre-annealed at 200°C) in stoichiometric ratios according to the reaction

$$3(1\text{-x})\text{CoO} + 3\text{xMgO} + V_2O_5 \rightarrow (Co_{1-x}Mg_x)_3V_2O_8$$

for two different nominal dopant concentrations ($x = 0.05, 0.20$). The compound was initially reacted in air at 925°C for a day, followed by two more heatings for 24 hours at 950°C and 975°C, respectively. Good homogeneity of the mixture was ensured through intermediate grindings. The formation of the correct phase in the resulting polycrystalline powder was verified using

X-ray powder diffraction. The powder was then loaded in a rubber tube and hydrostatically pressed at 60 MPa to produce a 10-13 cm long feed rod of 0.7-0.8 cm diameter. This polycrystalline rod was finally sintered in air at 1050°C for 24 hours. The resulting feed rod was mounted in a Crystal Systems Inc. image furnace. A pre-grown pure $Co_3V_2O_8$ (CVO) crystal was mounted as the seed for the growth of the doped material, providing a "lattice template" to the feed material to grow on in order to facilitate high-quality growth at an early stage in the growth process. To establish the floating zone, the ends of both seed and feed rod were melted. The growth was then performed at slightly lower temperatures in ambient atmosphere and pressure. A growth rate of 2 mm/h was found to produce the highest-quality crystals. At higher growth rates, zone stability could not be maintained. Throughout the growth, the seed crystal and feed rod were rotating in opposite directions at 30 rpm. Additional back-feeding of the feed rod between ∼0.3 mm/h and ∼0.9 mm/h helped to reduce multiple grain growth at early stages of the growth and to establish stable growth conditions.

Through appropriate tuning of the growth conditions, 5-6 cm long single crystal boules with ∼0.6-0.7 cm in diameter were obtained (Fig. 4.2).

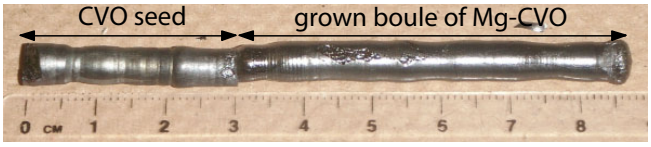

Figure 4.2: As-grown crystal of $(Co_{1-x}Mg_x)_3V_2O_8$ with nominal Mg concentration of $x = 0.20$ and the pre-grown pure $Co_3V_2O_8$ seed crystal.

Laue X-ray diffraction (Fig. 4.3) was used to determine the growth direction of the crystals which was found to be $\sim 4^\circ$ and $\sim 12^\circ$ off of the a-axis for nominal Mg dopings of $x = 0.05$ and $x = 0.20$, respectively. This suggests that the growth direction shifts from nearly-[100] in the pure CVO to the perpendicular [010] or [001] directions with an increase of Mg concentration from $x = 0.0$ ($Co_3V_2O_8$) to $x = 1.0$ ($Mg_3V_2O_8$), consistent with the previously reported growth direction of $Mg_3V_2O_8$ along the [010] direction.[6]

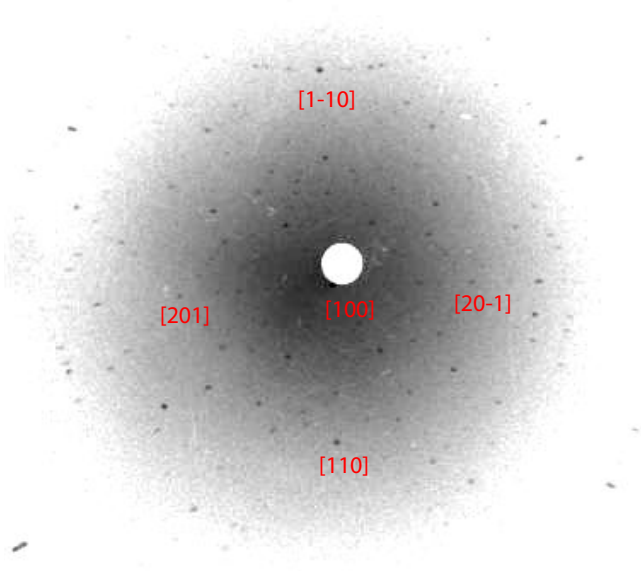

Figure 4.3: Laue X-ray diffraction on $(Co_{1-x}Mg_x)_3V_2O_8$ for nominal $x = 0.05$ indexes the crystal growth direction as being $\sim 4^\circ$ off [100].

EDX measurements on small parts of the grown crystals were performed at the CCEM at McMaster University using a field-emission SEM (JEOL 7000F) at 20 keV incident electron energy. Qualitative analysis of the spectra taken at eight different points on each sample confirms the chemical composition of the samples, with Mg, V and Co being the only metal elements present.

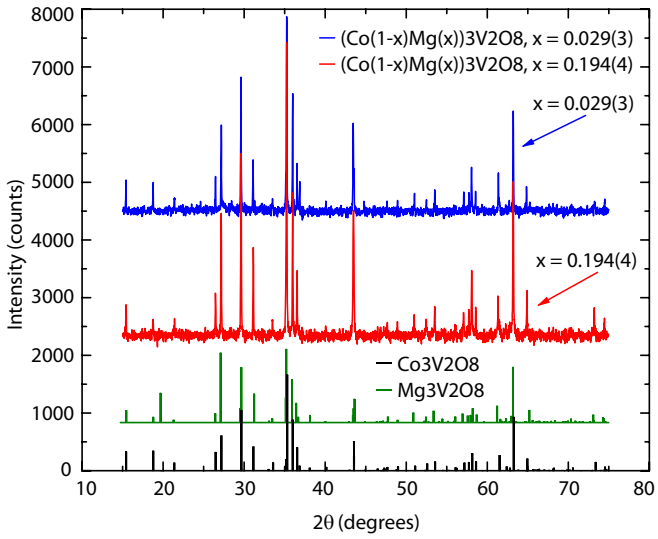

Figure 4.4: XRD powder patterns on crushed single crystals of $(Co_{1-x}Mg_x)_3V_2O_8$ with $x = 0.029(3)$ and $x = 0.194(4)$, and reference spectra for pure $Co_3V_2O_8$[7] and $Mg_3V_2O_8$.[8]

Small parts of the grown crystals were ground and examined using a PANalytical X-ray powder diffractometer with Cu K_α radiation. The powder patterns (Fig. 4.4) confirm the phase purity for both the nominal $x = 0.05$ and nominal $x = 0.20$ Mg concentrations, and the relative intensities of the peaks shift in agreement with the Mg doping levels.

Single crystal XRD data were collected at room temperature using a Bruker Smart APEX2 diffractometer equipped with a Mo K_α rotating anode source. The crystal sizes used for the measurements were 0.134 x 0.222 x 0.357 mm^3 for the nominal concentration of $x = 0.05$ and 0.144 x 0.212 x 0.427 mm^3 for the nominal concentration of $x = 0.20$. The structural refinement was performed on ∼1100 unique reflections using the SHELXL-97 program in space group *Cmca* and *R*-factors of 0.028 and 0.044 were obtained for $x = 0.05$ and $x = 0.20$, respectively, after the application of absorption and extinction cor-

rections. The values of the lattice parameters obtained from the single crystal refinement are shown in Table 4.1 and are compared to those of pure CVO single crystals previously obtained by Chen *et al.*[3] and Szymczak *et al.*.[4] The refined atomic positions are given in Table 4.2. The resulting Mg dopant concentration has been determined as $x = 0.029(3)$ and $x = 0.194(4)$ for nominal concentrations of $x = 0.05$ and $x = 0.20$, respectively. The site substitution by Mg ions on the Co site is preferential to the (8e) Co(2) site for both Mg concentrations of $x = 0.029(3)$ and $x = 0.194(4)$. The site occupancy factors for the $x = 0.029(3)$ sample were obtained as Co(1):Mg(1)=0.984:0.016 and Co(2):Mg(2)=0.965:0.035, while for the sample with $x = 0.194(4)$ Mg concentration, the occupancy factors were determined as Co(1):Mg(1)=0.841:0.159 and Co(2):Mg(2)=0.788:0.212. In both cases a preference is shown for the Mg ions to substitute for Co at the less symmetric (8e) site. This site preference has also been reported by Wang *et al.*[9] in mixed Co-Mg orthovanadate solid solutions grown by slow cooling from high temperature solutions.

A SQUID magnetometer was used to characterize the magnetic properties of the grown single crystals. The temperature dependence of the mass susceptibility measured along the crystallographic a-axis in an applied field of $H = 50$ Oe is shown in Fig. 4.5. These measurements show two well-defined magnetic transitions at $T \sim 10$ K and $T \sim 5.2$ K for $x = 0.029(3)$. We associate the higher temperature transition with a transition from the paramagnetic to an antiferromagnetic phase that has been observed in the pure compound at $T \sim 11.2$ K,[4] while we associate the lower transition temperature of $T \sim 5.2$ K with the transition to a ferromagnetic ground state. Interestingly, this transition occurs at a $\sim 20\%$ lower temperature than observed in the pure CVO

Table 4.1: Lattice parameters of $(Co_{1-x}Mg_x)_3V_2O_8$, space group Cmca (No. 64)

a (Å)	b (Å)	c (Å)	V (Å^3)	comment
6.045	11.517	8.316	579.0	$Co_3V_2O_8$, flux growth[3]
6.034(7)	11.488(8)	8.300(4)	575.3	$Co_3V_2O_8$, floating zone[4]
6.0147(4)	11.5116(9)	8.3174(6)	578.5(1)	$(Co_{(1-x)}Mg_x)_3V_2O_8$, $x = 0.029(3)$, floating zone, this work
6.0492(6)	11.4938(11)	8.3162(7)	578.2(2)	$(Co_{(1-x)}Mg_x)_3V_2O_8$, $x = 0.194(4)$, floating zone, this work

Table 4.2: Structural parameters for $(Co_{1-x}Mg_x)_3V_2O_8$ for concentrations of $x = 0.029(3), 0.194(4)$

Atom	x		y		z	
	$x = 0.029(3)$	$x = 0.194(4)$	$x = 0.029(3)$	$x = 0.194(4)$	$x = 0.029(3)$	$x = 0.194(4)$
Co(1)/Mg(1)	0		0		0	
Co(2)/Mg(2)	0.25		0.13269(2)	0.13297(3)	0.25	
V	0		0.37735(2)	0.37771(3)	0.12057(4)	0.12060(5)
O(1)	0		0.2501(1)	0.2502(2)	0.2289(2)	0.2281(2)
O(2)	0		0.0009(1)	0.0015(2)	0.2448(2)	0.2448(2)
O(3)	0.2707(2)	0.2717(2)	0.11850(9)	0.1184(1)	0.9982(2)	0.9982(2)

compound ($T_C = 6.1$ K[3,5]) which shows that the effect of disorder introduced by a Mg-doping concentration of only $x = 0.029(3)$ is quite drastic.

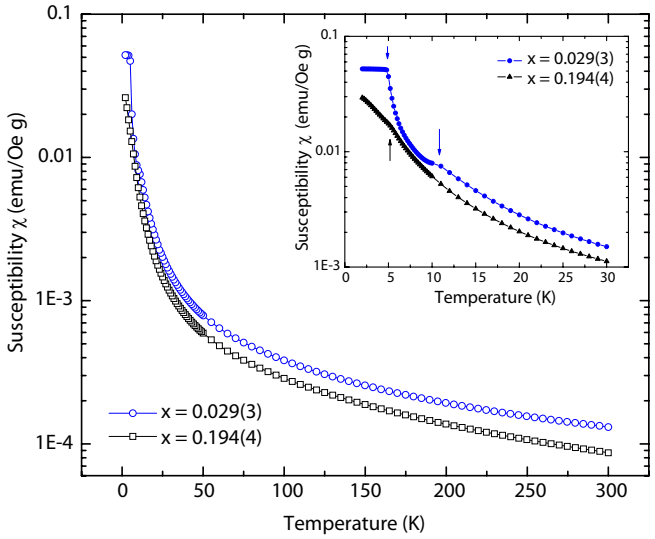

Figure 4.5: Temperature dependence of the mass susceptibility of $(Co_{1-x}Mg_x)_3V_2O_8$ single crystals for an applied field of $H = 50$ Oe along the a-axis. The inset shows the low-temperature range. Arrows indicate the location of magnetic phase transitions.

This is even more evident in the susceptibility data for the $x = 0.194(4)$ Mg-doped crystal, which shows that this magnetic phase transition is completely absent at least down to $T = 2$ K. A broad anomaly at ~ 5 K is likely related to ferromagnetic fluctuations, but there is no evidence of a long range ordered state above $T = 2$ K. Considering that $Co_3V_2O_8$ is a 3D magnetic system based on 2D kagome motifs, these results are rather unusual as the theoretical percolation threshold for the destruction of long range order in these structures is estimated as $x \sim 0.35$.[10] The response of this system to disorder is thus more sophisticated than one would estimate from simple ferromagnetic percolation.

High-quality single crystals of $(Co_{1-x}Mg_x)_3V_2O_8$ with Mg concentrations of $x = 0.029(3)$ and $x = 0.194(4)$ have been grown using the floating zone method, using a single crystal of pure $Co_3V_2O_8$ as the seed for the growth. Structural and magnetic properties have been presented in detail. The size of the crystals is suitable for inelastic neutron scattering experiments that are currently being performed, and will be the basis for a complete characterization of the low temperature ground state in this magnetically dilute kagome staircase system.

This work was supported by NSERC of Canada. The authors wish to acknowledge G. de Silveira for EDX measurements, J. Britten for structure refinement and A. Dabkowski for helpful discussions.

4.2 Magnetic Order and Fluctuations in the Presence of Quenched Disorder in the Kagome Staircase System $(Co_{1-x}Mg_x)_3V_2O_8$

K. Fritsch,[1] Z. Yamani,[2] S. Chang,[3] Y. Qiu,[3,4] J. R. D. Copley,[3]
M. Ramazanoglu,[1] H. A. Dabkowska,[5] and B. D. Gaulin[1,5,6]

[1]*Department of Physics and Astronomy, McMaster University, Hamilton, Ontario, L8S 4M1, Canada*

[2]*Canadian Neutron Beam Centre, National Research Council, Chalk River Laboratories, Chalk River, Ontario, K0J 1P0, Canada*

[3]*NIST Center for Neutron Research, NIST, Gaithersburg, Maryland 20899-8102, USA*

[4]*Department of Materials Science and Engineering, University of Maryland, College Park, Maryland 20742, USA*

[5]*Brockhouse Institute for Materials Research, Hamilton, Ontario, L8S 4M1, Canada*

[6]*Canadian Institute for Advanced Research, 180 Dundas St. W., Toronto, Ontario, M5G 1Z8, Canada*

Abstract

$Co_3V_2O_8$ is an orthorhombic magnet in which $S = 3/2$ magnetic moments reside on two crystallographically inequivalent Co^{2+} sites, which decorate a stacked, buckled version of the two-dimensional kagome lattice, the stacked kagome staircase. The magnetic interactions between the Co^{2+} moments in this structure lead to a complex magnetic phase diagram at low temperature, wherein it exhibits a series of five transitions below 11 K that ultimately culminate in a ferromagnetic ground state below $T \sim 6.2$ K. Here we report magnetization measurements on single- and polycrystalline samples of

$(Co_{1-x}Mg_x)_3V_2O_8$ for x <0.23, as well as elastic and inelastic neutron scattering measurements on single crystals of magnetically dilute $(Co_{1-x}Mg_x)_3V_2O_8$ for x=0.029 and x=0.194, in which nonmagnetic Mg^{2+} ions substitute for magnetic Co^{2+}. We find that a dilution of 2.9% leads to a suppression of the ferromagnetic transition temperature by ∼15% while a dilution level of 19.4% is sufficient to destroy ferromagnetic long-range order in this material down to a temperature of at least 1.5 K. The magnetic excitation spectrum is characterized by two spin wave branches in the ordered phase for $(Co_{1-x}Mg_x)_3V_2O_8$ (x=0.029), similar to that of the pure x=0 material, and by broad diffuse scattering at temperatures below 10 K in $(Co_{1-x}Mg_x)_3V_2O_8$ (x=0.194). Such a strong dependence of the transition temperatures on long-range order in the presence of quenched nonmagnetic impurities is consistent with two-dimensional physics driving the transitions. We further provide a simple percolation model that semi-quantitatively explains the inability of this system to establish long-range magnetic order at the unusually low dilution levels which we observe in our experiments.

4.2.1 Introduction

Geometrically frustrated materials that are based on magnetic moments which decorate a lattice of triangular networks have been of great recent interest due to their intriguing low temperature magnetic properties and a rich variety of exotic ground states such as spin glasses, spin ices, and spin liquids which they exhibit.[11,12]

$Co_3V_2O_8$ belongs to the $M_3V_2O_8$ family (M=Co, Ni, Cu, Mn)[13–15] which incorporates into its structure an anisotropic variation of the ideal two dimensional (2D) kagome lattice. The kagome lattice is itself a network of corner-sharing triangles. Within this structure, the magnetic moments are carried by $3d$ transition metal M^{2+} ions that decorate kagome layers. These layers buckle in and out of the plane, forming the kagome staircase structure. $Co_3V_2O_8$ (CVO) crystallizes in the orthorhombic space group $Cmca$.[7] Edge-sharing $Co^{2+}O_6$ octahedra are situated slightly below and above the a-c plane, stacked along the crystallographic b axis and are separated by nonmagnetic $V^{5+}O_4$ tetrahedra. A representation of the structure including only the Co^{2+} ions is shown in Fig. 4.6(a). The magnetic interactions between the Co^{2+} $S = 3/2$ moments are mediated by Co-O-Co superexchange; the resulting magnetic exchange pathways are indicated in Fig. 4.6(a) as grey bonds. Within the buckled kagome layers that form the a-c plane [Fig. 4.6(b)] the $S = 3/2$ magnetic moments reside on two crystallographically inequivalent Co^{2+} sites: crystallographic (8e) spine (s) sites (blue) run in chains along the a axis, and these chains are linked by (4a) cross-tie (c) sites (red).

The low temperature magnetic phase diagrams of all known members of the kagome staircase family are complex and show considerable diversity in their rich behavior, despite their isostructural nature.[13–15] For example, $Ni_3V_2O_8$ displays 4 different magnetically ordered states below 10 K and has attracted much interest due to the discovery of multiferroic behavior in one of its incommensurate phases at low temperature. [2,13,16] The low-temperature phase diagram of $Co_3V_2O_8$ (CVO) has been studied by neutron diffraction in both zero[3,5,17,18] and in finite applied magnetic fields.[19,20] It has also been studied

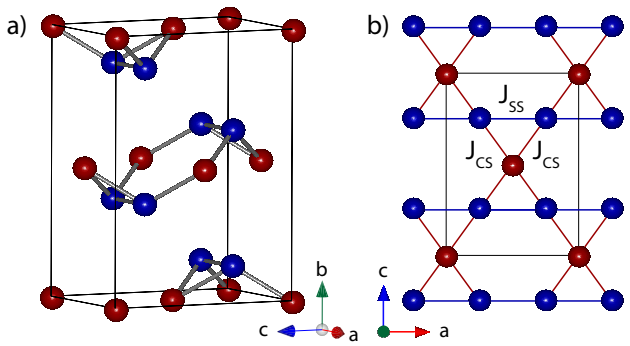

Figure 4.6: The crystal structure of $Co_3V_2O_8$. (a) View of the kagome staircase considering only the Co^{2+} ions (red and blue) which are stacked along the b axis. (b) View of the kagome plane projected on the ac plane with the crystallographically inequivalent cross-tie (red) and spine sites (blue). The magnetic exchange interactions discussed in the text are indicated.

by optical spectroscopy,[21,22] by heat capacity and magnetization[4,13] as well as by μSR[23] and by NMR techniques.[24,25] This extensive set of measurements has revealed a series of 5 different magnetic phase transitions below 11.2 K in zero applied magnetic field. These ultimately culminate in a ferromagnetic ground state below $T \sim 6.2$ K. All five of the magnetic states display a preferred direction of the spins parallel to the a axis, the easy axis of this system. From previous inelastic neutron scattering measurements, the exchange parameters of the microscopic Hamiltonian in the ground state of CVO have been extracted to some approximation, using linear spin wave theory.[5] These calculations approximate the CVO system as two-dimensional and reveal that the exchange between magnetic moments on the cross-tie and spine sites is ferromagnetic and $J_{cs} \sim$1.25 meV, while the exchange between adjacent spine sites [J_{ss} in Fig. 4.6(b)] is negligible. Significant uniaxial anisotropy terms in

the Hamiltonian have also been found (∼1-2 meV), consistent with the easy a direction.

Previous work has examined stacked kagome staircase magnets in the presence of disorder, specifically $(Co_{1-x}Ni_x)_3V_2O_8$, where random mixtures of Ni^{2+} and Co^{2+} reside on the M^{2+} site.[26,27] The phase behavior of such systems is expected to be complex, as both Ni^{2+} and Co^{2+} are magnetic, and a minimum of three exchange interactions would be necessary to describe the system, even if only a single M^{2+} site was crystallographically relevant.

Here we report on $(Co_{1-x}Mg_x)_3V_2O_8$ which can be thought of in terms of $Co_3V_2O_8$ in the presence of quenched magnetic vacancies, as Mg^{2+} does not carry a magnetic moment. As the ultimate ground state in $Co_3V_2O_8$ is a uniaxial ferromagnet, one would expect this to represent an excellent model for a quasi-two-dimensional Ising system in the presence of quenched disorder. As such, one would expect to be able to understand its phase diagram and ground state properties in some detail.

Dilution studies of other Ising magnets have been carried out over a long period of time.[28] In most cases, these can be understood in the context of percolation theory. However, there are interesting examples where this is not the case. One such example is the case of the stacked triangular lattice Ising-like antiferromagnet in the presence of quenched nonmagnetic impurities, $CsCo_{1-x}Mg_xBr_3$, wherein the combination of antiferromagnetic exchange and triangular coordination leads the quenched magnetic vacancies to couple to the relevant order parameter as a random field.[29]

In this paper, we present magnetization measurements on both polycrystalline and single-crystalline samples of $(Co_{1-x}Mg_x)_3V_2O_8$ as well as elastic and inelastic neutron scattering measurements on single- crystal $(Co_{1-x}Mg_x)_3V_2O_8$ with $x = 0.029$ and $x = 0.194$. We study the phase diagram as a function of Mg^{2+} doping, x, and show how a simple two-dimensional percolation model can provide an explanation for the drastic suppression of the magnetic ordering at low temperatures in this material. In addition, we study the spin correlations and dynamics at low temperature as a function of doping, and show the existence of a Griffiths-like phase[30] in the presence of quenched disorder, when $T_C(x) < T < T_C(x = 0)$.

4.2.2 Experimental Details

Two large high-quality single crystals of $(Co_{1-x}Mg_x)_3V_2O_8$ with concentrations of x=0.029(3) and 0.194(4) were grown at McMaster University using an optical floating-zone image furnace.[31] Details of these growths and a subsequent X-ray structural refinement for these crystals are reported in Ref. 32.[32] This work allows us to both quantify x, and to determine that the site dilution of the magnetic Co^{2+} ions by nonmagnetic Mg^{2+} is almost random. The single crystals resulting from these growths had a mass of $\sim$ 8 g and had approximately cylindrical shapes, with dimensions of 50 mm in length and 7 mm in diameter. Magnetization measurements were performed using a conventional SQUID magnetometer at McMaster University on several polycrystalline samples with a range of Mg concentrations ($x = 0 - 0.23$) as well as on three single crystals (x=0, x=0.029 and x=0.194). These single crystal samples were cut

from the main crystal growths to a rectangular shape (∼2.5 mm x 2 mm x 2 mm), and were aligned such that magnetization and susceptibility measurements could be performed with the magnetic field aligned along particular directions. All three single crystal samples used in these magnetization measurements had a mass of ∼10 mg. Neutron scattering measurements, using both triple-axis and time-of-flight techniques, were performed at the NIST Center for Neutron Research (NCNR). The experiments were performed on two ∼25 mm long cylindrical $(Co_{1-x}Mg_x)_3V_2O_8$ samples with x=0.029 and x=0.194, which were aligned such that the $[H, 0, L]$ plane in reciprocal space was coincident with the horizontal scattering plane.

Detailed elastic neutron scattering measurements were carried out using the cold triple-axis spectrometer SPINS at the NCNR, NIST. These measurements employed a vertically focusing PG-002 monochromator and flat PG-002 analyzer crystal with fixed final energy of E_f=5 meV. The collimation used was [open, 80', 80', 80'] with an in-pile, cooled Be filter placed in the incident neutron beam incident in order to eliminate higher order wavelength contamination. Inelastic neutron scattering measurements were carried out on the time-of-flight disk chopper spectrometer (DCS)[33] at the NCNR, NIST, employing a fixed incident wavelength of $\lambda_i = 2.5$ $\AA$, which allowed for the measurement of magnetic excitations up to energy transfers of ΔE $\sim$ 10 meV. In this configuration of DCS, a resolution of $\sim$ 0.9 meV was obtained at the elastic position. The samples were placed in a conventional ILL Orange cryostat with a base temperature of 1.5 K for both the SPINS and DCS experiments.

4.2.3 Magnetization Measurements

We performed magnetization measurements using a SQUID magnetometer on a series of $(Co_{1-x}Mg_x)_3V_2O_8$ samples with different doping concentrations in the range ($x = 0 - 0.23$). Measurements were carried out on polycrystalline samples as well as on single crystal samples ($x = 0$, $x = 0.029$ and $x = 0.194$).

The temperature-dependent molar susceptibility χ(T) was measured in a field-cooled (FC) mode in an applied field of $\mu_0 H = 0.005$ T and this is shown in the inset of Fig. 4.7 for selected values of x. For the measurements on single crystals (open symbols), the crystals were aligned with their easy a axis parallel to the applied magnetic field. We note here that the $\chi(T)$ curves for the doped single crystal samples ($x = 0.029$ and $x = 0.194$) display highly anisotropic behavior [34] for the magnetic field applied along the different crystal axes, similar to what has been observed in the pure compound [35].

Measurements on pure $Co_3V_2O_8$ show two well-defined magnetic transitions at $T_N \sim 11.2$ K and at $T_C \sim 6.2$ K as indicated by arrows in the inset. We associate the higher temperature transition with a transition from the paramagnetic to an incommensurate antiferromagnetic phase, and the lower temperature transition at $\sim$6.2 K with the transition to the ferromagnetic ground state, as has been reported previously.[3] These two transition temperatures were extracted from $\chi(T) \cdot T$ curves, shown for a subset of the data in Fig. 4.8, resulting in the phase diagram shown in Fig. 4.7.

These measurements reveal a suppression of both transition temperatures with increasing x, and the complete suppression of any magnetic ordering at $T = 0$ can be extrapolated to a critical doping concentration of $x_c \sim 0.26$.

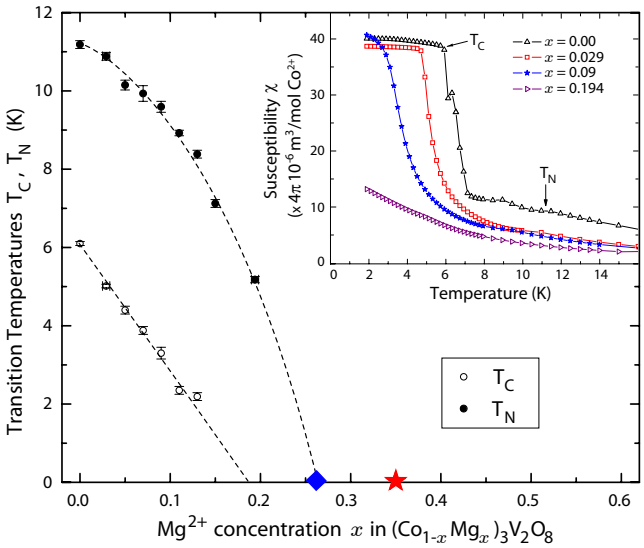

Figure 4.7: The phase diagram of $(Co_{1-x}Mg_x)_3V_2O_8$ as a function of x obtained from magnetization measurements described in the text. The error bars result from the determination of the transition temperatures using data in Fig.4.8. The phase boundaries (dashed lines) are guides to the eye and are extrapolated to $T = 0$ K. The theoretically expected site percolation limit for the perfect 2D kagome lattice ($x_c \sim 0.35$)[10] is shown as red star. The critical doping concentration x_c above which any magnetic ordering gets suppressed at $T = 0$ corresponds to the determined percolation limit discussed later in the text and is shown as blue diamond. The inset shows representative scans of the field-cooled molar susceptibility χ(T) for an applied field of $\mu_0 H = 0.005$ T, and the phase transition temperatures T_C and T_N for data points in the phase diagram.

This result is somewhat unexpected since this doping level is lower than the theoretical percolation threshold for the destruction of long-range order for the ideal 2D kagome lattice, for which $x_c \sim 0.35$ (indicated as red star in the phase diagram). [10,36] It is also much lower than the percolation threshold for any three-dimensionally ordered system where x_c ~0.68-0.80. [37–39] Note that the percolation threshold p_c reported in the literature is related to x_c discussed here by $x_c = 1 - p_c$. While p_c describes the critical concentration of *magnetic*

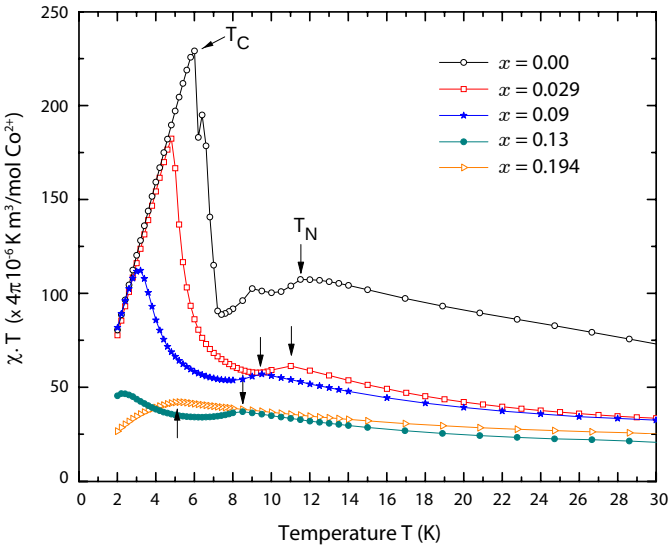

Figure 4.8: Representative scans of the susceptibility $\chi(\mathrm{T}) \cdot T$ in a field of μ_0H=0.005 T reveal anomalies at the phase transition temperatures $\mathrm{T_C}$ and $\mathrm{T_N}$ (indicated by arrows). These transition temperatures are used to construct the phase diagram shown in Fig. 4.7. Closed symbols refer to data obtained from polycrystalline samples, while open symbols represent measurements on single crystals with μ_0H aligned parallel to the a-axis of the system. Note that the maximum in the $\chi(\mathrm{T}) \cdot T$ curve in the x=0.194 doped sample is indicated as phase transition with a $\mathrm{T_N} \sim 5$ K in Fig. 2, however, elastic neutron scattering data shows no clear evidence for long range magnetic correlations at any temperature above 1.5 K in this sample.

ions below which magnetic long range order ceases to exist, x_c is used for the complementary description of the critical concentration of *nonmagnetic* ions above which long range order is impossible. We choose to speak of the percolation threshold x_c in this paper instead of p_c as it is directly related to the concentration of nonmagnetic Mg^{2+} ions in our doped CVO.

From the phase diagram in Fig. 4.7, it can be seen that the ferromagnetic transition temperature T_C is very sensitive to magnetic dilution and changes almost linearly with x. It is lowered by ∼20% from T_C ∼6.2 K in the pure

material to T_C ∼5.2 K for a doping level of x=0.029, and for x=0.194 it is suppressed below the lowest accessible temperature for our SQUID measurements. In contrast, the higher temperature Néel transition changes more gradually with dilution, exhibiting downwards curvature as a function of x. The reason for this difference is not clear, although we do note that while the transition at T_N appears to be continuous, that at T_C is clearly discontinuous even in the presence of quenched disorder, as we will discuss below.

4.2.4 Elastic Neutron Scattering Results

Elastic neutron scattering measurements were performed on two doped single crystal samples (x=0.029 and x=0.194) using the cold triple-axis spectrometer SPINS at the NCNR, NIST. The temperature dependence of the elastic magnetic scattering was followed around the (0,0,2) Bragg peak, which exhibits a weak nuclear component, and a strong ferromagnetic component to the Bragg peak below T_C ∼6.2 K in the pure, x=0, material. The strength of this magnetic Bragg peak follows as the form of the magnetic neutron scattering cross section is sensitive to the component of moment perpendicular to $\mathbf{Q}$. Its strength indicates that the ordered moment points along a. A color contour plot constructed from elastic longitudinal (0,0,L) scans through (0,0,2) as a function of temperature for both samples is presented in Figs. 4.9(a) and 4.9(c). Representative scans are shown in Figs. 4.9(b) and 4.9(d). Note that the intensity appropriate to the color contour plots in Figs. 4.9(a) and 4.9(c) is on a logarithmic scale.

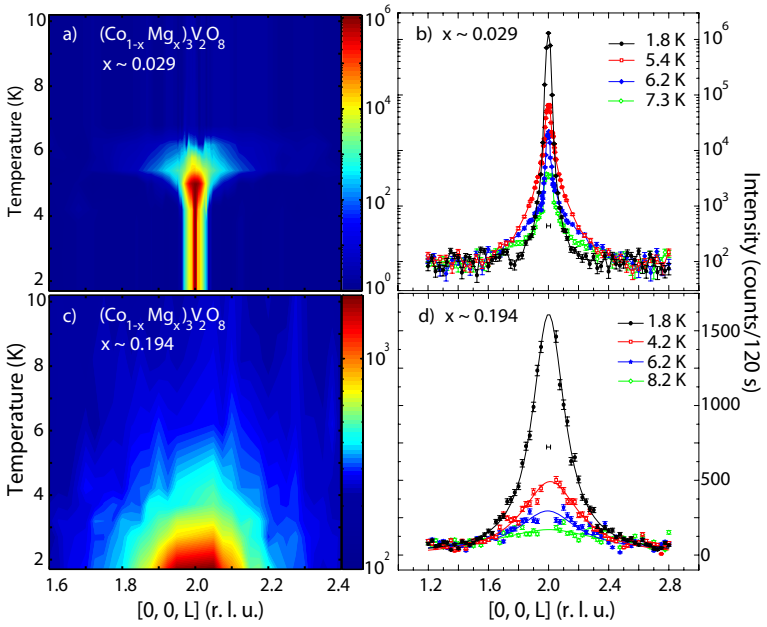

Figure 4.9: Contour plots showing the temperature evolution of the elastic magnetic scattering $S(\mathbf{Q}, E = 0)$ around the $\mathbf{Q}$=(0,0,2) Bragg peak position for (a) $x = 0.029$ and (c) $x = 0.194$. A background data set within the paramagnetic state at T = 20 K has been subtracted from the individual (0,0,L) scans so as to eliminate the weak nuclear component to the (0,0,2) Bragg scattering. Representative scans making up the contour plots are shown in panels (b) and (d). The instrumental resolution of SPINS is indicated in panels (b) and (d) as the black horizontal bar. The error bars represent one standard deviation in this and the following figures.

In the data sets for both x=0.029 and x=0.194, a high temperature data set at $T = 20$ K (in the paramagnetic phase) has been subtracted, so as to eliminate the temperature-independent, nuclear scattering from the lower temperature data sets, and hence to isolate the magnetic scattering. It can easily be seen that the scattering profiles for the two samples are in striking contrast to each other. As the temperature is lowered below $T \sim T_{\rm C}(x = 0) \sim 6.2$ K in the x=0.029 Mg-doped sample [Figs. 4.9(a) and 4.9(b)], diffuse scattering intensity characteristic of the development of short-range correlations builds

up, increasing in strength down to a temperature of $T_C(x = 0.029)$ ∼5.2 K. Below ∼5.2 K it gives way to a dramatic increase in elastic scattering intensity which is now sharper in **Q** and characteristic of long-range order. It is therefore associated with a phase transition to the ferromagnetic ground state. This can be seen more clearly in Fig. 4.10, which displays the temperature dependence of the net scattered intensity upon warming and cooling measured at the Bragg peak position (0,0,2) associated with the order parameter, and at a **Q** position slightly away from the Bragg peak, at (0,0,1.8), allowing for the parametrization of the diffuse scattering characteristic of the short-range order. Based on the sharpness of the transition and the observed hysteresis in the order parameter, this transition is clearly of first-order nature.

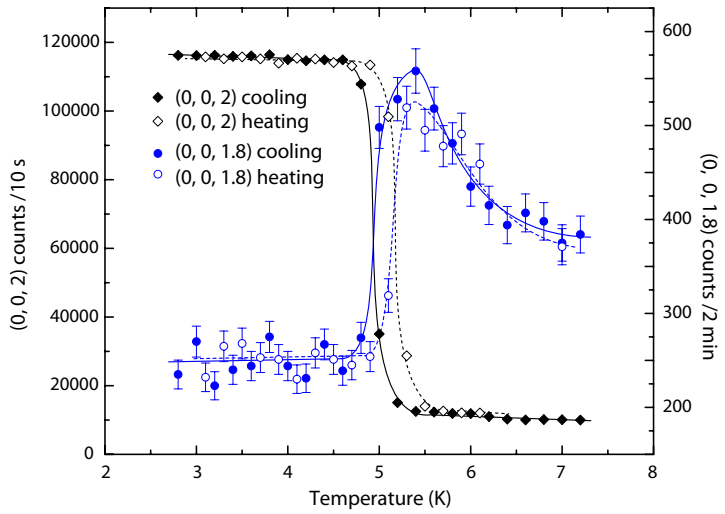

Figure 4.10: The order parameter and diffuse scattering as a function of temperature measured near the (0,0,2) magnetic Bragg peak in the x=0.029 sample. Note the different intensity scales and counting times.

The diffuse critical scattering in the wings of the elastic Bragg peak is observed to be drastically enhanced in a Griffiths-phase-like fashion[30,40] in the

temperature region between $T_C(x = 0.029)$ ∼5.2 K and $T < T_C(x = 0)$ ∼6.2 K. Such a Griffiths phase shows enhanced spin correlations due to relatively rare, large correlated spin droplets[41] that arise as a consequence of the random quenched disorder.[30] The effect of thermal fluctuations is such that the system would be long-range ordered in the absence of quenched disorder, and large percolating networks of spins display enhanced correlations somewhat akin to long-range order.

The (0,0,L) scans of the magnetic scattering from this x=0.029 sample are best described by a two-component lineshape consisting of a Lorentzian lineshape characterizing the short-range correlations and a resolution-limited Gaussian lineshape which describes the onset of long-range magnetic order.

The results of this lineshape analysis are given in Fig. 4.11, wherein the integrated intensities of the Gaussian and Lorentzian components of the magnetic scattering at (0,0,2) for the x=0.029 sample are shown in panel (a). A representative elastic scan with corresponding fits at T = 5.8 K, in the Griffiths-like phase, between $T_C(x = 0)$ and $T_C(x = 0.029)$ is displayed in the inset of panel (a).

For the higher doping level of the x=0.194 sample, the scattering profile is in sharp contrast to that at x=0.029, as shown in the color contour maps in Fig. 4.9 and with the data we now discuss in Fig. 4.11. In agreement with the magnetization data, no magnetic long-range order is evident down to the lowest temperature measured, ∼1.5 K. Instead, the scattering profile is entirely dominated by a broad diffuse scattering component around the (0,0,2) Bragg position, indicative of very short-ranged correlations. After subtraction

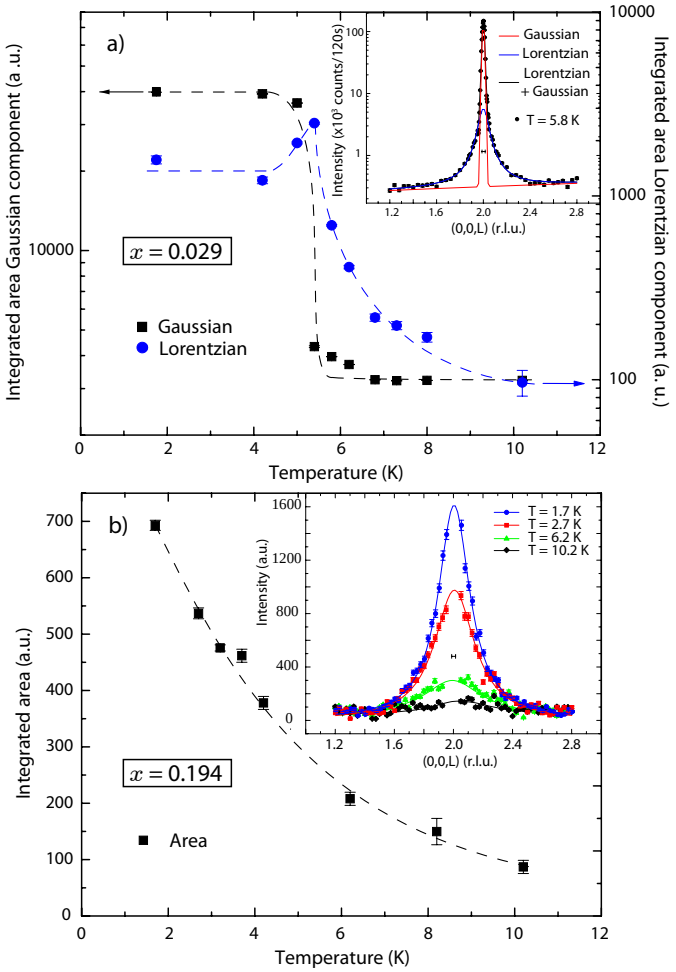

Figure 4.11: Elastic scattering in the (a) x=0.029 and (b) x=0.194 doped $(Co_{1-x}Mg_x)_3V_2O_8$ samples. (a) The integrated intensities of the Gaussian (black) and Lorentzian (blue) components to the lineshape used to describe the magnetic scattering in the x=0.029 sample discussed in the text are shown. A representative scan with corresponding fits in the Griffiths-like phase at $T = 5.8$ K is shown in the inset. (b) The integrated intensity of the Lorentzian lineshape used to describe the magnetic scattering in the x=0.194 doped sample is shown, while the inset displays representative scans in L along the (0, 0, 2) direction for different temperatures with fits to the Lorentzian lineshape as described in the text. For both panels (a) and (b) a $T = 20$ K high temperature nonmagnetic background has been subtracted to isolate the magnetic scattering. Note that the peaks for the x=0.194 doped sample in the inset of panel (b) are much wider than the instrumental resolution at SPINS, which is shown as black horizontal bar.

of the high-temperature nuclear Bragg intensity, it was found that a Lorentzian lineshape alone was appropriate to describe the magnetic scattering profile at all temperatures. Figure 4.11(b) shows the integrated intensity of the magnetic diffuse scattering around (0,0,2) and the inset shows several representative scans and the corresponding Lorentzian fits to this scattering for x=0.194. One can clearly see that the diffuse scattering is very weak at 10 K and that it develops noticeably below $T_{\rm C}(x = 0)$ ∼6.2 K, again consistent with a Griffiths-like phase between $T_{\rm C}(x = 0)$ and zero temperature, increasing monotonically on cooling down to 1.5 K.

The full widths at half maximum (FWHMs) of the Lorentzian components characterizing the short-range correlations in both the $(Co_{1-x}Mg_x)_3V_2O_8$ samples with x=0.029 and x=0.194 are compared in Fig. 4.12. It is clear that the FWHM of the $x = 0.029$ sample drops approximately to 0 at $T_{\rm C}(x = 0.029) \sim$ 5.2 K, consistent with resolution-limited scattering and long-range magnetic order. In contrast, the magnetic scattering from the x=0.194 sample maintains a finite width to the lowest temperatures measured, $T = 1.5$ K. At this temperature, the (0,0,2) peak displays a FWHM of ∼0.25 r.l.u., corresponding to a real-space spin-correlated-droplet within the kagome plane of about 24 Å in diameter, approximately the size of two to three unit cells. While no phase transition to long-range order is observed for x=0.194, the trend for the evolution of the FWHM of this magnetic scattering approximately extrapolates to 0 at $T = 0$, indicating that x=0.194 is close to a quantum critical point. We also note that the FWHM for both samples approach each other at the highest temperature measured ∼10 K, as we anticipate should occur. At these

high temperatures, thermal fluctuations are expected to dominate the effects of the quenched disorder.

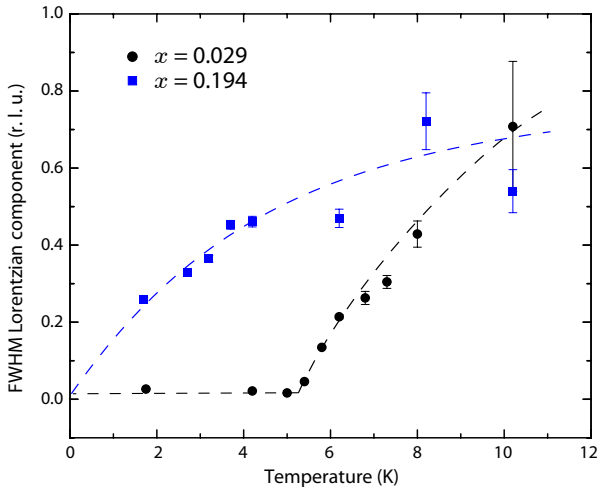

Figure 4.12: FWHM of the Lorentzian components shown for both doped single crystal samples. The dashed lines are guides to the eye. While for x=0.029, the FWHM of the scattering near (0,0,2) drops to 0 at 5.2 K as the sample develops long-range order, for the higher doping of x=0.194, the scattering maintains a finite **Q**-width to the lowest temperatures measured. The trend for the evolution of the FWHM for x=0.194 however, extrapolates approximately to 0 at $T = 0$.

We further investigated the nature of the elastic scattering using TOF neutron data taken on DCS at NCNR, NIST. The obtained maps of elastic scattering $S(\mathbf{Q}, E = 0)$ are shown in Figs. 4.13(a) and 4.13(c) for x=0.029 and in Figs. 4.13(b) and 4.13(d) for x=0.194, each for two different temperatures, $T = 1.5$ K and $T = 5.5$ K.

One notes that the net elastic scattering at $T = 1.5$ K, following subtraction of a $T = 20$ K data set, is different for the x=0.194 sample than for either the pure x=0 (not shown here), or the lightly doped x=0.029 sample. Figure 4.14 shows that Bragg-like scattering is observed for the x=0.194 sample around

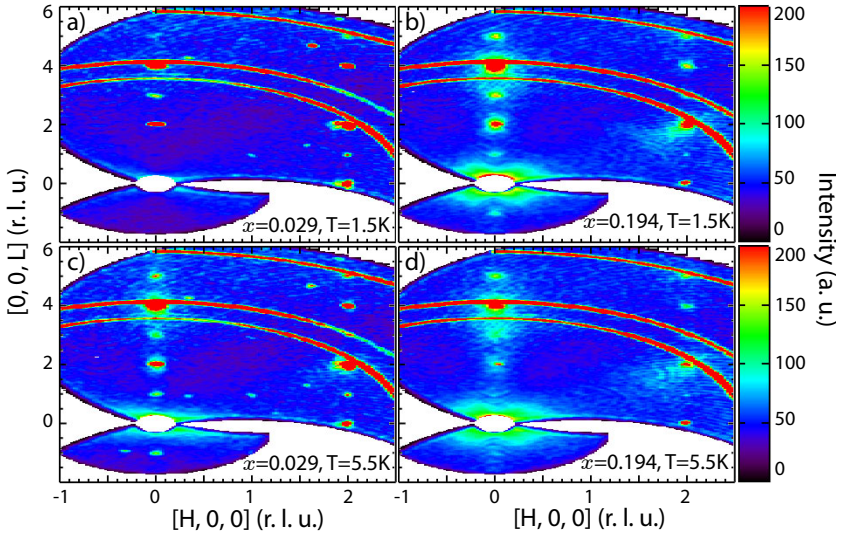

Figure 4.13: Maps of the elastic scattering intensity $S(\mathbf{Q}, E = 0)$ for $(Co_{1-x}Mg_x)_3V_2O_8$ with $x = 0.029$ and $x = 0.194$ and for two different temperatures, $T = 1.5$ K (top row) and $T = 5.5$ K (bottom row).

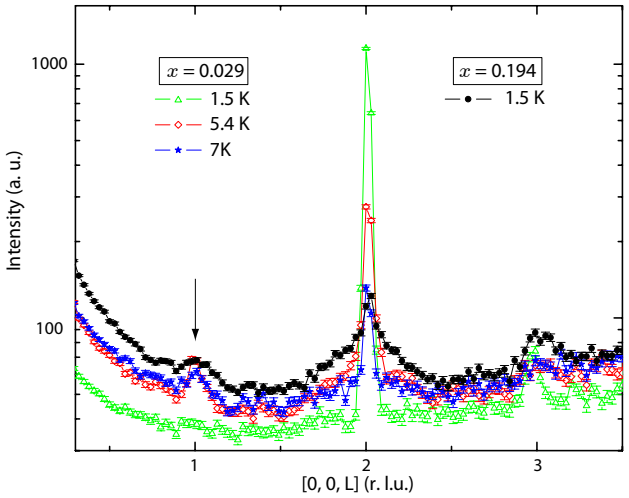

Figure 4.14: Cuts through the color contour maps maps shown in Fig. 8 along [0,0,L]. The observed (0,0,1) peak at $T = 1.5$ K in the x=0.194 sample is a clear signature of incommensurate fluctuations of the form (0,δ,L) that are observed in the x=0.029 sample at $T = 5.5$ K and $T = 7$ K. This is consistent with the phase diagram presented in Fig. 4.7.

all of the (0,0,L) Bragg positions for integer L, likely originating from short-range incommensurate elastic magnetic scattering of the form (0, δ, L). This scattering, which does not lie in our horizontal scattering plane, is picked up in our DCS experiment due to the finite acceptance of the scattered neutrons out of the horizontal plane, and is consistent with the placement of the x=0.194 single crystal sample on the phase diagram for $(Co_{1-x}Mg_x)_3V_2O_8$ as shown in Fig. 4.7.

4.2.5 Inelastic Neutron Scattering Results

We investigated the evolution of the dynamic spin correlations in $(Co_{1-x}Mg_x)_3V_2O_8$, the excitations out of the ground state, using inelastic neutron scattering measurements carried out on DCS at NCNR, NIST. Figure 4.15 shows $S(\mathbf{Q}, E)$ observed in the three x=0, x=0.029, and x=0.194 single crystal samples along two perpendicular directions in reciprocal space.

Panels (a) and (b) in the top row of Fig. 4.15 show $S(\mathbf{Q}, E)$ for the pure, $x = 0$, sample at $T = 200$ mK, panels (c) and (d) correspond to the x=0.029 sample at $T = 1.5$ K, and (e) and (f) correspond to x=0.194. The respective 20 K, high-temperature data sets for each x have been subtracted for all data sets shown. The spin wave spectrum in all three samples consists of two bands of spin excitations, a relatively narrow band near ~ 2 meV and a broader band between $\sim$3 and 6.5 meV. These are consistent with earlier spin wave results on the pure x=0 sample.[5]

As expected from the elastic neutron scattering results discussed above, the inelastic spectrum for the pure and the x=0.029 samples look similar within

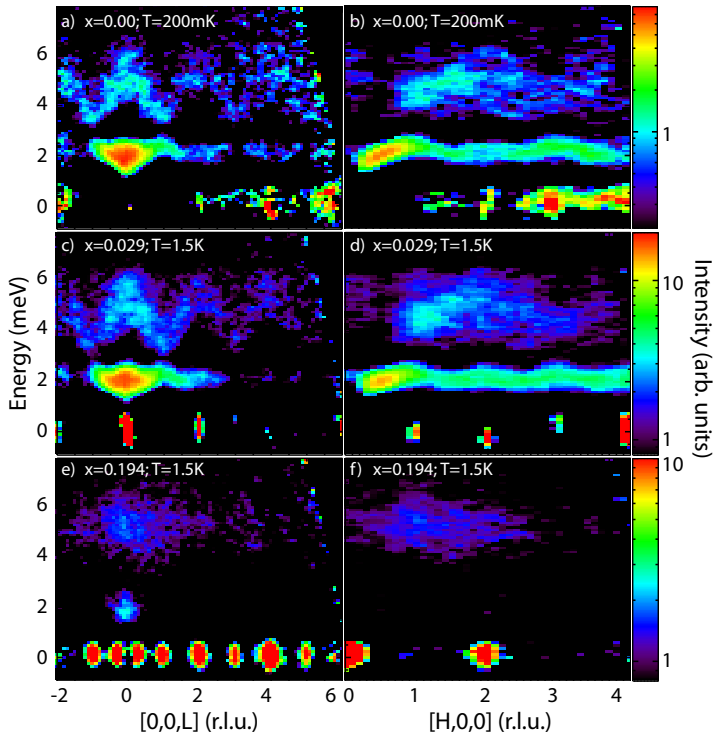

Figure 4.15: $S(\mathbf{Q}, E)$ in x=0 (top), x=0.029 (middle) and x=0.194 (bottom row) samples along two perpendicular directions in reciprocal space. All data shown has had its respective high temperature T = 20 K background data set subtracted. Note that the data has been taken at the base temperatures appropriate to each experiment, which was 200 mK for x=0 and T = 1.5 K for both x=0.029 and x=0.194.

their ordered states, although broadening of the spin wave excitations in energy is clear on doping, corresponding to shorter spin wave lifetimes in the presence of quenched impurites for the x=0.029 sample. The inelastic scattering from the most heavily doped x=0.194 sample shows poorly defined bands of spin excitations which are most easily observable in the vicinity of $\mathbf{Q}$=0. These are typical of the magnetic inelastic spectrum within the incommensurate phases or paramagnetic state at elevated temperatures.

The inelastic magnetic spectrum can be further compared between the three x=0, x=0.029, and x=0.194 samples by taking cuts through the color contour maps of $S(\mathbf{Q}, E)$ shown in Fig. 4.15, and normalizing to the incoherent elastic scattering. This normalization should account for the somewhat different volumes of sample within the neutron beam. This is shown in Fig. 4.16, where we have shown an approximate constant-$\mathbf{Q}$=(1.5, 0, 0) scan, which has been constructed by integrating in H between 1.4 and 1.6 and in L between $\pm$ 0.2 r.l.u.. The spectral weight of the sharp spin excitations falls off dramatically with increased concentration of quenched nonmagnetic disorder.

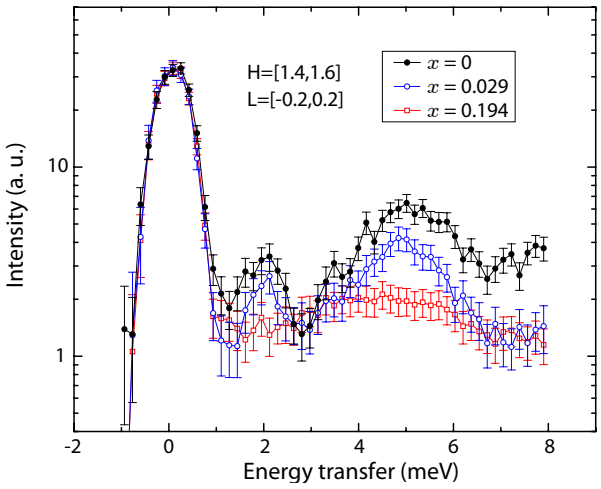

Figure 4.16: Cuts through scattering intensity around (1.5,0,0) and integrating over a narrow range in H=[1.4,1.6] and L=[-0.2,0.2] r.l.u. on a logarithmic intensity scale. To facilitate the comparison between these two sets of measurements, the scattered intensity has been normalized to the incoherent elastic scattering of the pure sample.

Further, we investigated the temperature evolution of the inelastic scattering in the two doped samples, x=0.029 and 0.194, as shown in Fig. 4.17 which shows $S(\mathbf{Q}, E)$ along the [0,0,L] direction in reciprocal space. This is consistent with our elastic scattering studies, which placed the x=0.194 doped

sample at 1.5 K in a region of the phase diagram that is characterized by incommensurate elastic magnetic order and rather diffuse spin wave excitations. This corresponds to the same region of the phase diagram in which one finds the x=0.029 sample at elevated ($T = 5.5$ K and $T = 7$ K) temperatures. Note also the ressemblance of (b) and (c) with(e), which are all placed in the incommensurate antiferromagnetic phase in the phase diagram of diluted CVO.

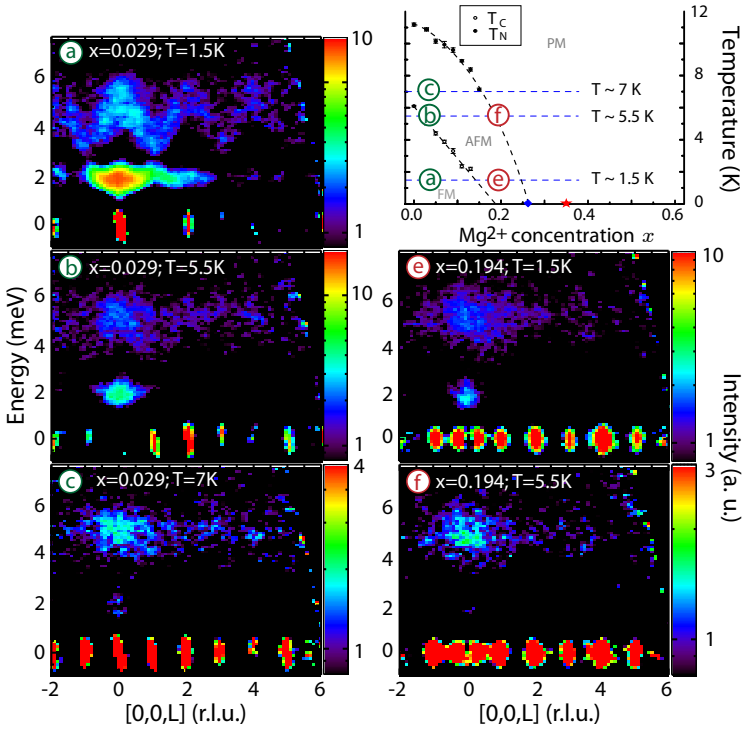

Figure 4.17: The temperature evolution of the inelastic scattering $S(\mathbf{Q}, E)$ along [0,0,L], contrasting the x=0.029 and x=0.194 samples. Panels (a), (b) and (c) correspond to the x=0.029 sample at the temperatures indicated in phase diagram in the top right panel. Panels (e) and (f) correspond to the x=0.194 sample with temperatures as shown in the phase diagram.

4.2.6 Percolation Calculations and Discussion

In light of the phase diagram obtained for $(Co_{1-x}Mg_x)_3V_2O_8$, shown in Fig. 4.7, and both the elastic and inelastic neutron scattering in the presence of quenched disorder, one can raise the question as to why dilution with quenched magnetic vacancies is so effective in destroying the magnetic order in this system. Figure 4.7 shows the ferromagnetic transition to be suppressed to zero temperature at $x \sim 0.19$, while all vestiges of incommensurate magnetic order have been suppressed to zero temperature by $x \sim 0.26$. This is far below the percolation threshold for any three-dimensional cooperative system, where critical concentrations of $x_c \sim 0.7$ ($p_c \sim 0.3$) are typical.[39,42] In and of itself, this shows that the weak three-dimensional interactions along the third, stacking dimension, b, do not determine this criticality. These interactions are certainly weak compared to the strong interactions within the kagome-staircase plane, but they may also be frustrated as a consequence of the triangular coordination of spins on cross-tie sites which neighbor the spine-site spins along the b axis.

To further examine this question, we carried out a simple two-dimensional, zero temperature percolation calculation relevant to $(Co_{1-x}Mg_x)_3V_2O_8$. Our starting point for a calculation of the percolation limit in this system was a two-dimensional projection of the magnetic moments within a single buckled kagome layer. For the calculations, a lattice of 100×100 unit cells was used, from which we randomly removed magnetic sites (either cross-tie or spine positions) with probability x. As Ramazanoglu et al.'s [5] linear spin wave theory on the pure CVO material showed the magnetic interactions between magnetic

moments on the spine sites to be negligible, we then *excluded* magnetic interaction pathways between spine sites for the remaining steps in the calculation. We calculated the number of sites contained in the largest cluster, that is the number of sites contained in the largest near-neighbor connected region of the lattice, and checked whether any continuously connected path through the lattice (chosen arbitrarily from the left to the right edge of the lattice) could be found. If several such connected paths were found, the length of the shortest path through the lattice between sites making up the largest lattice-spanning cluster was calculated. We ran this simulation up to 30 times for each dilution probability x to get a good estimate of the percolation threshold, which we find to be at $x_c \sim$0.26. A calculation for the full connectivity of the site-diluted lattice was performed as well, by *including* the interaction pathways between spine sites. This calculation recovers the well-known percolation threshold for the two-dimensional kagome lattice of $x_c \sim$0.35 (p_c=0.65). Though the finite size of the system smears out the actual percolation threshold x_c, the threshold for the original kagome lattice is well reproduced.[10] Increasing the lattice size does not change the result for x_c significantly, and we therefore conclude that our estimate of $x_c \sim 0.26$ for the case of $(Co_{1-x}Mg_x)_3V_2O_8$, where the magnetic interactions between spine sites is negligible, is accurate.

A summary of both simulations is shown in Fig. 4.18. In the top panel, the number of sites within the largest cluster, normalized to the total number of sites occupied by magnetic moments (which depend on x), is shown. The black squares denote the data for the case of full kagome connectivity, while data in blue circles represents the case in which spine-spine connectivity (ss-ss correlations) is excluded, corresponding to the physical picture relevant to

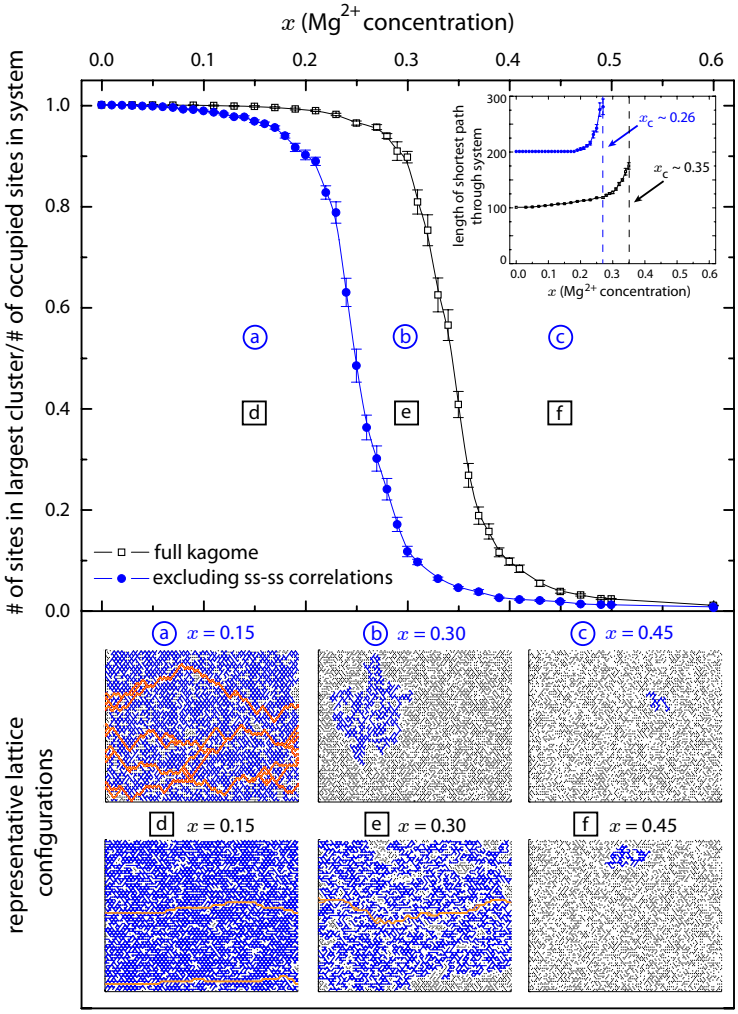

Figure 4.18: Percolation calculations showing the evolution of the largest cluster size in a lattice containing 100x100 unit cells as a function of site dilution x. The inset shows the length of the shortest path through the system connecting the edges of the lattice, if it exists. Above the percolation threshold, the lattice edges cannot be connected, and there is no shortest path. Note that the evolution of the largest cluster size is normalized to its value at zero site dilution (x=0). Error bars in the normalized largest cluster sizes are determined from the standard error. The determination of the shortest path through the system was based on only those data sets that showed connectivity of the lattice, and the error bars are given by the standard error of these data sets.

$(Co_{1-x}Mg_x)_3V_2O_8$. In the inset, the length of the shortest path, if it exists, is shown for both cases. The point x_c for which the lattice cannot be connected and thus no shortest path can be found, is indicated by a dashed line and is determined as $x_c \sim 0.35$ for the full kagome connectivity and as $x_c \sim 0.26$ for the case appropriate to $(Co_{1-x}Mg_x)_3V_2O_8$. It is interesting to note that the length of the shortest path increases relatively gradually for the full kagome connectivity, while excluding spine-spine connections leads to a flat dependence on the length of the shortest path through the system, until a dilution level of about $x \sim 0.20$ is reached, beyond which the length of the shortest path rises rapidly towards $x_c \sim 0.26$. This seems reasonable as the random removal of cross-tie and spine sites is equivalent in the fully connected kagome case, while the removal of cross-tie sites, which make up 1/3 of all sites is more effective than the removal of the majority spine sites, for the case where magnetic interactions between spine sites is negligible. This is because removal of a cross-tie site "disables" a possible path to 4 spine sites, while removal on a spine site only "disables" the interaction path between 2 cross-tie sites.

Representative lattice configurations at dilution levels of x=0.15, x=0.30 and x=0.45 are shown in the bottom panel of Fig. 4.18, for both cases. The largest cluster in the lattice is colored in blue and the shortest lattice spanning path(s) are shown in orange. As one can clearly see, at a dilution level of $x = 0.30$, there exists a largest, lattice spanning cluster in the case of full kagome connectivity (bottom middle panel), while for the case of excluding spine-spine connectivity as is relevant for $(Co_{1-x}Mg_x)_3V_2O_8$, only a finite-sized cluster exists, which does not span the full lattice and thus does not allow for long-range magnetic order.

4.2.7 Conclusions

We have presented the low temperature phase diagram of the kagome staircase system CVO in the presence of quenched disorder, showing the transition temperatures T_{N} and T_{C} as function of nonmagnetic Mg^{2+} doping in $(Co_{1-x}Mg_x)_3V_2O_8$. We have found that the magnetic properties of this material at low temperatures are very susceptible to quenched disorder and that a doping level of $x \approx 0.26$ is large enough to suppress any long-range order to below 1.5 K.

Based on the geometric arrangement of the magnetic Co^{2+} moments within the kagome plane, a simple two-dimensional percolation model has been used to understand the effect of magnetic dilution on the possible exchange paths. For that purpose, we considered a flat, two-dimensional kagome lattice with site dilution x, and calculated the percolation threshold. Based on previous inelastic neutron scattering on CVO, which found the spine-spine magnetic interactions to be negligible compared with the cross-tie-spine interactions,[5] we calculated the percolation threshold of $x_c \sim 0.26$ for the case of cross-tie-spine connectivity (excluding spine-spine bonds). As a reference, we confirmed the percolation threshold for the kagome lattice as $x_c \sim 0.35$ ($p_c \sim 0.65$). The calculation of the percolation threshold excluding spine-spine connectivity is found to be in good agreement with the observed phase diagram that puts the percolation threshold at $\sim$26% doping level.

For two samples with doping levels of x=0.029 and x=0.194, respectively, we have performed elastic and inelastic neutron scattering measurements. The elastic neutron scattering measurements could be understood in terms

of Griffiths-like phase fluctuations appearing between $T_C(x = 0)$ and $T_C(x)$, wherein enhanced short-range order is observed. For the case of the lightly doped x=0.029 sample, such short-range correlations collapse into a long-range ordered ferromagnetic state via a first order phase transition at T_C ∼5.2 K. The more heavily doped x=0.194 sample displays only ferromagnetic short-range order to the lowest temperatures measured, and shows the co-existence of incommensurate fluctuations at base temperature, consistent with the phase diagram for $(Co_{1-x}Mg_x)_3V_2O_8$ described above.

Our inelastic neutron scattering measurements on the lightly doped x=0.029 sample show spin waves comparable to those observed in pure, $x = 0$, CVO, albeit with finite energy widths, and hence spin wave lifetimes within its low temperature state. The equivalent magnetic excitation spectrum observed in the x=0.194 sample shows magnetic spectral weight in the same energy regime, but no well-defined spin wave excitations at any wave vector.

This work utilized facilities supported in part by the National Science Foundation under Agreement No. DMR-0944772, and was supported by NSERC of Canada. The DAVE software package[43] was used for data reduction and analysis of DCS data. The authors would like to thank A. B. Dabkowski and C. Majerrison for assistance with sample preparation and P. Dube for assistance with the magnetization measurements.

4.3 Quantum Fluctuations in the Kagome Staircase System $Co_3V_2O_8$ in a Transverse Magnetic Field

K. Fritsch,[1] K. C. Rule,[2] G. Ehlers,[3] K. Habicht,[2] K. Kiefer,[2]
M. Ramazanoglu,[1] H. A. Dabkowska,[5] and B. D. Gaulin[1,5,6]

[1]*Department of Physics and Astronomy, McMaster University, Hamilton, Ontario, L8S 4M1, Canada*

[2]*Helmholtz Zentrum Berlin für Materialien und Energie, D-14109 Berlin, Germany*

[3]*Neutron Scattering Science Division, Oak Ridge National Laboratory, Oak Ridge, Tennessee 37831-6475, USA*

[5]*Brockhouse Institute for Materials Research, Hamilton, Ontario, L8S 4M1, Canada*

[6]*Canadian Institute for Advanced Research, 180 Dundas St. W., Toronto, Ontario, M5G 1Z8, Canada*

Abstract

We present magnetization and single crystal time-of-flight neutron scattering measurements in the kagome staircase material $Co_3V_2O_8$ in a transverse magnetic field. The field is applied along the stacking direction of the kagome layers, transverse to the easy axis of the Ising-like moments in this quasi two-dimensional magnet, introducing quantum fluctuations that lead to quantum phase transitions at $H_{c1} \sim 6.25$ T, $H_{c2} \sim 7$ T and $H_{c3} \sim 13$ T. These quantum critical points are associated with an abrupt change in magnetic structure at the two lowest transitions, while a rather gradual change is observed at

the higher field transition at $\sim$ 13 T. The spin excitation spectra and their associated energy gaps are discussed.

4.3.1 Introduction

The study of strongly correlated electron materials displaying quantum phase transitions (QPTs) has attracted great recent interest due to their relevance in understanding the unconventional properties of heavy fermion systems[44,45] or high temperature superconductors.[45] In contrast to conventional phase transitions, QPTs are driven by quantum mechanical fluctuations in the absence of thermal fluctuations. These quantum fluctuations can be controlled by external parameters such as pressure,[46] doping[47,48] or magnetic field.[49,50] One of the simplest examples of a QPT occurs for Ising spins in a transverse magnetic field, for which the Hamiltonian can be written as

$$\mathcal{H} = -\sum_{ij} J_{ij} S_i^z S_j^z + \sum_i D\left(S_i^z\right)^2 - g\mu_{\mathrm{B}} H \sum_i S_i^x. \tag{4.1}$$

Here, the J_{ij} exchange term couples the z-components of the spin operators S at sites i and j, while the magnetic field $g\mu_{\mathrm{B}}H$ acts on the *transverse*, x-component of the spins only, mixing the spin states and ultimately leading to the destruction of long range order at a critical field H_c, which occurs independently of temperature. The term $D\left(S_i^z\right)^2$ describes the single-ion anisotropy responsible for an energy gap in the magnetic excitation spectrum of the system in zero field. Prominent examples for the experimental realization of

this model include the three-dimensional dipolar-coupled uniaxial ferromagnet $LiHoF_4$,[51,52] and the weakly coupled S=1/2 Ising chain system $CoNb_2O_6$.[53]

In this paper, we report on transverse field induced QPTs in the quasi two-dimensional Ising-like $S = 3/2$ system $Co_3V_2O_8$ that we investigated using magnetization and neutron scattering techniques.

$Co_3V_2O_8$ (CVO) is a member of the kagome staircase family of materials with formula $M_3V_2O_8$ (M=Co, Ni, Cu, Mn),[13–15] which are characterized by a stacked arrangement of buckled kagome layers representing an anisotropic version of the well known two-dimensional (2D) kagome lattice. The magnetic moments in these structures reside on divalent $3d$ transition metal ions that occupy two crystallographically inequivalent sites within the buckled kagome layers. In CVO, the magnetism arises from $S = 3/2$ moments associated with the Co^{2+} ions. A representation of the structure including only the magnetic Co^{2+} ions and their different crystal sites is shown in Fig. 4.19a). Within the buckled kagome layers that lie in the a-c plane (Fig. 4.19b), the magnetic moments on the spine sites (s) form chains along the a axis, and these chains are linked by the cross-tie sites (c). These layers are well separated from each other along the b direction by nonmagnetic vanadium (V^{5+} $3d^0$) oxide layers (not shown), giving rise to the quasi two-dimensional nature of this system.

The low temperature magnetic phase diagrams of all known members of the kagome staircase family are fairly complex and show different behavior despite their isostructural nature.[13–15] In $Ni_3V_2O_8$, for example, four different magnetically ordered states are observed below 10 K. This material has also

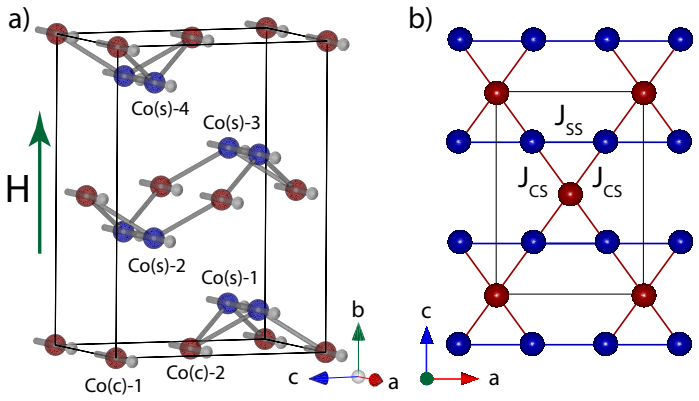

Figure 4.19: The crystal structure of $Co_3V_2O_8$. For clarity, only the magnetic Co^{2+} ions are shown. (a) View of the kagome staircase considering only the Co^{2+} ions (red and blue) which are stacked along the b axis. The positions of the six Co positions in the unit cell are shown. (b) View of the kagome plane projected on the ac plane with the crystallographically inequivalent cross-tie (red) and spine sites (blue). The magnetic exchange interactions discussed in the text are indicated. The magnetic field is applied in the b direction, transverse to the magnetic easy axis (a) in the kagome plane of the system.

been the focus of research based on the discovery of multiferroic behavior in one of its incommensurate phases.[2,13,16,54]

The low temperature zero-field phase diagram of CVO has been studied by neutron diffraction, [3,5,17,18] by optical spectroscopy,[21,22] by heat capacity and magnetization[4,13] as well as by μSR[23] and by NMR techniques.[24,25] In zero field, CVO is found to enter a series of four different incommensurate and commensurate antiferromagnetic phases below 11.2 K that ultimately terminate in a ferromagnetic ground state below T ~6.2 K. All five of the magnetic states display a preferred direction of the spins parallel to the a axis, the easy axis of this system. The phase diagram is highly anisotropic, and from magnetization measurements it is found that the susceptibility along the easy a axis is almost two orders of magnitude larger than that along the hard axis in the

b direction.[4,17,55] The susceptibility along c is intermediate between that along a and b, and we therefore expect CVO to effectively approximate a quasi two-dimensional Ising system. A complication to this simple picture arises from the fact that within the ferromagnetic phase, the moments on the cross-tie and spine sites behave differently, with the moment size on the cross-tie sites being reduced by almost a factor of two from the full moment size of $3\mu_B$ on the spine sites.[17]

From previous inelastic neutron scattering measurements in zero field,[5] the exchange parameters of the microscopic Hamiltonian have been extracted by approximating CVO as two-dimensional system and using linear spin wave theory to describe the spin dynamics. The resulting exchange parameters between magnetic moments on the cross-tie and spine sites are found to be ferromagnetic and rather small with $J_{cs} \sim 1.25$ meV, while the exchange between adjacent spine sites [J_{ss} in Fig. 4.19(b)] is found to be negligible. Uniaxial anisotropy terms on the order of ∼1-2 meV are also found, in agreement with the easy axis anisotropy. The influence of small magnetic fields ($\mu_0 H < 2.5$ T) on the ground state of CVO and its temperature dependence have been investigated by single crystal neutron diffraction for fields applied along the a axis[20] and along the a and c axes.[19] These sets of measurements mainly focused on the complex evolution of the magnetic structure in the different commensurate and incommensurate antiferromagnetic field-induced phases. To date, the excitation spectrum of CVO has only been studied in the initial zero-field triple-axis work by Ramazanoglu *et al.*,[5] and in the presence of quenched disorder using time-of-flight data by Fritsch *et al.*[55]

The work presented here is therefore the first to investigate the magnetic structure and excitation spectrum of CVO in a transverse magnetic field, and more importantly, the first work to study the experimental realization of transverse field induced quantum phase transitions in a quasi two-dimensional Ising system.

4.3.2 Experimental Details

A high-quality single crystal of $Co_3V_2O_8$ was grown at McMaster University using an optical floating-zone image furnace.[31] The single crystal used for the neutron scattering measurements was cut to a rectangular shape of 18 mm x 5 mm x 5 mm and carefully aligned to less than 0.5° in the horizontal $[H, 0, L]$ scattering plane. It was held in a custom made aluminum sample mount to prevent sample rotation in strong transverse magnetic fields. Magnetization measurements were performed on a smaller crystal (∼2.5 mm x 2 mm x 2 mm) cut from the main crystal growth, which was again aligned to within 0.5° so that magnetization measurements could be performed along the magnetically hard (b) axis. These magnetization measurements were run at MagLab at HZB, using the 14 T high magnetic field vibrating sample magnetometer (VSM) option of the PPMS. Initial cold triple-axis neutron scattering measurements were performed at HZB using the FLEX spectrometer with focussing PG monochromator and analyzer at fixed final wave vector k_f=1.3 Å^{-1} (E_f=3.5 meV). For these inelastic measurements, the collimation was set to 60'-open-open (using the convention: monochromator to sample-sample to analyser-analyser to detector), and a cooled Be filter was used on the scat-

tered side to reduce higher order wavelength contamination. The sample was mounted in a dilution refrigerator with a base temperature of 50 mK and a 14.5 T vertical field magnet. A comprehensive set of neutron scattering data was obtained on the cold time-of-flight spectrometer CNCS[56] at the Spallation Neutron Source (SNS), Oak Ridge National Laboratory (ORNL), employing E_i =12 meV neutrons that gave an energy resolution of ∼0.5 meV at the elastic line. The magnetic field was supplied by the 16 T vertical field magnet cryostat "FatSam" with a base temperature of 1.6 K. Radial collimators were placed between magnet and the detectors to minimize scattering from the sample environment.

4.3.3 Magnetic Phase Diagram

Magnetization measurements were carried out over a temperature range of ∼3-15 K, in two ways: as a function of temperature at fixed field and as a function of field at fixed temperature. Critical fields and temperatures have been extracted from both sets of measurements from anomalies in the differential susceptibilities $\mathrm{d}M/\mathrm{d}T|_{\mathrm{H_{fix}}}$ and $\mathrm{d}M/\mathrm{d}H|_{\mathrm{T_{fix}}}$. The resulting phase diagram is shown in Fig. 4.20. In agreement with previous reports, we find zero-field transitions at 11.2 K (paramagnetic (PM) to incommensurate antiferromagnetic (IC AFM II)), 8.3 K (IC AFM II to IC AFM I), and 6.2 K (IC AFM I to ferromagnetic (FM)). While we are not sensitive to small details of the zero-field temperature dependence, which is beyond the scope of this paper, we largely reproduce the previously reported low field region of the phase diagram.[17,57] Our measurements extend the phase diagram for $H \parallel b$ previously reported

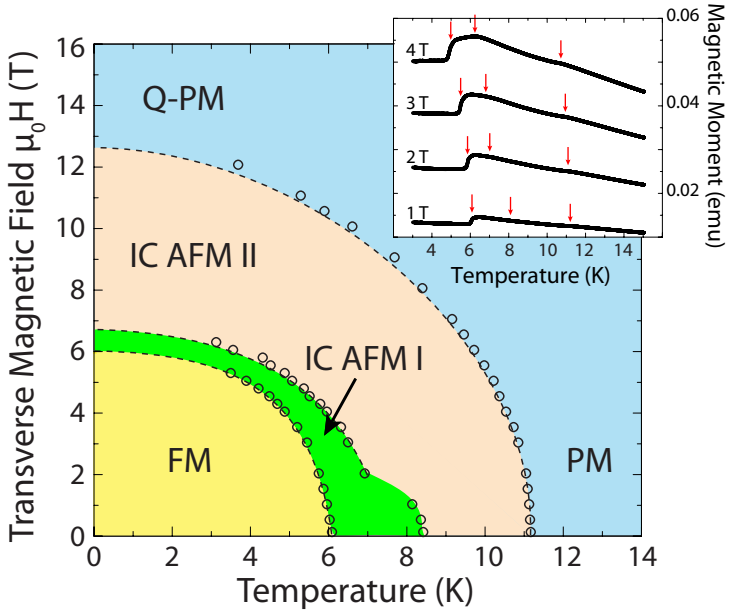

Figure 4.20: Magnetic phase diagram for $Co_3V_2O_8$ for $H \parallel b$ determined from magnetization measurements. The low temperature, low field ferromagnetic (FM) phase extends to 6.2 K and ∼6.25 T. Incommensurate antiferromagnetic phase I (IC AFM I) extends over a narrow region up to 7 T at 1.6 K and up to 8.2 K in zero field. A second incommensurate phase (IC AFM II) extends from 8.2 K to 11.2 K in zero field, and from 7 T up to ∼13 T at 1.5 K. Above 13 T, the system is in a partially field induced polarized quantum paramagnetic (Q-PM) phase that appears to connect smoothly to the paramagnet (PM) phase above 11.2 K in zero field. The inset shows representative magnetization data obtained at the MagLab at HZB.

by Wilson *et al.* up to higher fields up to 14 T and to lower temperatures, indicating three phase transitions at 1.5 K as a function of magnetic field. By connecting these phase transitions to those observed at higher temperature, we find transitions from ferromagnetic to IC antiferromagnetic phase I ($\sim$ 6.2 T), IC antiferromagnetic I to IC antiferromagnetic II ($\sim$ 7 T) and from IC antiferromagnetic II to a "quantum paramagnetic" phase at $\sim$ 13 T.

4.3.4 Neutron Scattering measurements and Discussion

Time-of-flight neutron scattering measurements were carried out on the Cold Neutron Chopper Spectrometer (CNCS) at SNS, which allows to map out both the elastic (static) and inelastic (dynamic) scattering function $S(\mathbf{Q}, E)$. Figure 4.21 shows an overview of the evolution of the elastic scattering for $-0.4 < E < 0.4$ meV within (a) the horizontal $[H, 0, L]$ scattering plane, binning over the vertical direction from $K = [-0.2, 0.2]$ r.l.u., and (b) slightly above the horizontal scattering plane, binning over $K = [0.2, 0.4]$ r.l.u., which is equivalent to probing elastic peaks of the form (H, δ, L) with $\delta = 0.3$. The data shown in these scattering maps has been corrected for detector efficiency and has a high temperature background taken at $T = 30$ K from within the paramagnetic regime subtracted from it. The resulting scattering intensities are therefore predominantly magnetic in origin.

In zero field, the in-plane scattering shows strong magnetic intensity at (0,0,$\pm$2), (0,0,4) and (2,0,4) positions, a smaller intensity at (2,0,2), but no scattering intensity is observed in the vertical detector banks ($\delta \sim 0.3$). In a field of 6.25 T, which corresponds to just above the first transition in the magnetic phase diagram to the IC AFM I phase, the elastic scattering is characterized by the appearance of the (2,0,1) peak in the horizontal plane, and by the appearance of scattering at (0,δ, $\pm$1), (0,δ, $\pm$2), (0,δ,3), (0,δ,4), as well as (2,δ,1), (2,δ,2), and (2,δ,4) positions with $\delta \sim 0.3$. Upon raising the field to 7 T, the line of reflections at $(0, \delta, L)$ disappears and new reflections of type $(1, \delta, L)$ with integer L emerge. At the same time, the intensity of the (2,0,1) reflection further increases while the intensity at $(0, 0, 2)$ drops

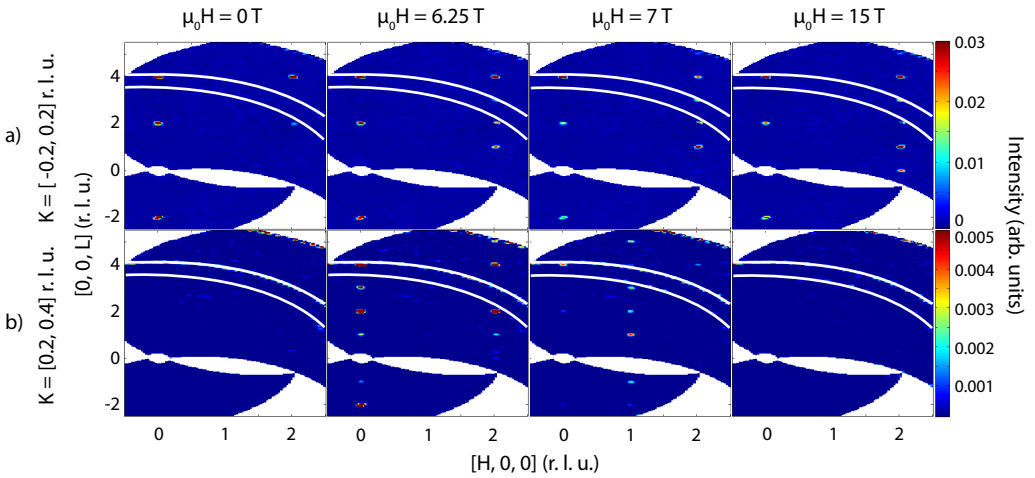

Figure 4.21: Elastic scattering for $-0.4 < E < 0.4$ meV in the horizontal scattering plane $K = [-0.2, 0.2]$ r.l.u. and slightly above the scattering plane in the vertical direction $K = [0.2, 0.4]$ r.l.u.. In an applied transverse field, the magnetic scattering intensities show a large change at the phase transitions of 6.25 T and 7 T determined from the phase diagram. Note the different intensity scales for the two scattering planes. The scattering out of plane is roughly an order of magnitude weaker than the in-plane scattering. A 30 K background from within the high temperature paramagnetic phase has been subtracted from all data that were also corrected for detector efficiency. The white rings are powder lines from the Aluminum sample mount and environment.

significantly compared to that at 6.25 T, signaling another phase transition just below 7 T. In the high-field state at 15 T, the incommensurate peaks have disappeared, and the in-plane scattering is dominated by the $(2, 0, 4)$, $(0, 0, 2)$ and $(2, 0, 1)$ reflections, as well as an additional $(2, 0, 0)$ peak.

The detailed field dependence of the magnetic elastic scattering has been extracted for all measured fields using the integrated intensities of the relevant peaks which are shown in Fig. 4.22. All of the intensities have had their 30 K analogue subtracted off to reveal only magnetic scattering. The zero-field scattering at strong $(0, 0, 2)$ and $(2, 0, 4)$ peaks (the other peaks at $(0, 0, 4)$ and

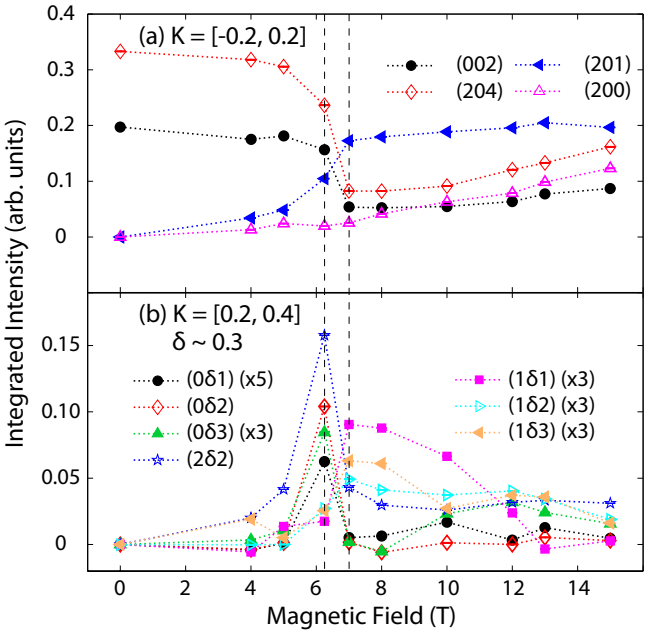

Figure 4.22: Integrated areas of the elastic peaks shown in Fig. 4.21 for peak positions that appear (a) in the horizontal plane for $K = [-0.2, 0.2]$ r.l.u. and (b) above the horizontal plane for $K = [0.2, 0.4]$ r.l.u., giving an approximate incommensuration of $\delta = 0.3$. As a function of field, a change of the magnetic structure at critical fields of 6.25 T and 7 T (indicated by dashed vertical lines) is clearly observable.

$(2, 0, 2)$ are not considered here because of their proximity to the Aluminum powder lines) indicates a ferromagnetic structure in which the moment size on the cross-tie sites is about half of the full moment of $\sim 3\mu_B$ present on the spine sites. All moments are aligned along the a axis. This is consistent with previous reports of the zero-field magnetic structure.[3,17] For 6.25 T and 7 T, the magnetic structure can only be partially understood on the basis of the collected data. Based on the nuclear structure factor of CVO, which allows reflections only at even integer L reflections, the scattering at 6.25 T and 7 T can be associated with a complicated magnetic structure that involves a) a doubling of the unit cell along the c direction and b) an incommensuration

of $\delta \sim 0.3$ along b. Including the observed strong $(2, 0, 1)$ peak and an absence of scattering at $(0, 0, 1)$ in the horizontal plane, one can deduce that a subset of the moments align antiferromagnetically along the c-axis. Upon increasing the field beyond 7 T, a gradual increase in intensity at the $(2, 0, 4)$ and $(2, 0, 0)$ positions is observed, while the intensity of $(0, 0, 2)$ shows little additional field dependence. What is more, the scattering intensity at $(2, 0, 1)$ appears to be fully developed by 7 T and it too shows little field dependence beyond 7 T. In the scattering plane sensitive to the incommensurate wave vector, the scattering intensity is seen to gradually decrease and vanish by 15 T. This could indicate that the incommensuration vanishes or slowly evolves to $\delta > 0.4$, moving this scattering intensity out of our field of view. The elastic scattering in the high-field structure at 15 T displays no obvious incommensurate scattering and all scattering resides in the horizontal scattering plane. Surprisingly, the scattering at our highest field is not consistent with a magnetic structure based on all moments pointing along the direction of the applied field (b axis) - as would be expected for a polarized paramagnet - and it clearly indicates more complex behavior. In fact, magnetic scattering at $(2, 0, 1)$ and $(2, 0, 0)$ positions and an absence of scattering at $(0, 0, 1)$ are found for an antiferromagnetic arrangement of the cross-tie moments aligned along the c axis, with all spine moments polarized along the b axis in the field direction. The scattering intensities for this magnetic structure are well reproduced assuming the moment sizes on cross-tie and spine sites to be different; the cross-tie sites appear to have their full moment of $\sim 3\mu_{\mathrm{B}}$, but the spine sites display only about half of their full zero-field moment. The two spin sites (cross-tie and spine) then form two decoupled subsystems, with moments

normal to the easy-magnetization axis: along c for the antiferromagnetically-correlated cross-tie sites, and along the hard, b axis for the field-polarized spine sites. Such a state suggests that antiferromagnetic interactions, which presumably compete with the dominant near-neighbor ferromagnetic interactions in this system and give rise to the incommensurate phases at intermediate temperatures, exist primarily on the cross-tie spin sublattice, and are therefore next-near neighbor exchange interactions. These spins "flop" along the intermediate c axis, rather than field-polarize along the hard b direction in the presence of a 15 T magnetic field, as the spine spins do, in order to minimize this antiferromagnetic exchange.

While we do not attempt to construct the real-space spin arrangement from the scattering at intermediate fields of 6.25 and 7 T, it is interesting to note that the elastic scattering at 1.6 K, 6.25 T for both in-plane and out-of-plane scattering is consistent with the zero-field and 1.5 T data at $T = 7$ K (not shown here) in the previously observed incommensurate phase I.[3] In contrast, the elastic scattering at 1.6 K and 7 T is found to be inconsistent with the data in 7 T at 7 K, the latter of which displays no obvious incommensurate scattering. As the incommensurate scattering is already weak at 1.6 K and 7 T, it is likely that it is weaker still at higher temperature, especially above T_{C}, but it could also be an indicator for an additional phase transition within the incommensurate antiferromagnetic phase II at non-zero field and temperatures > 1.6 K.

Inelastic scattering maps $S(\mathbf{Q}, E)$ are shown in Fig. 4.23 for several directions in reciprocal space, as a function of applied magnetic field. All of

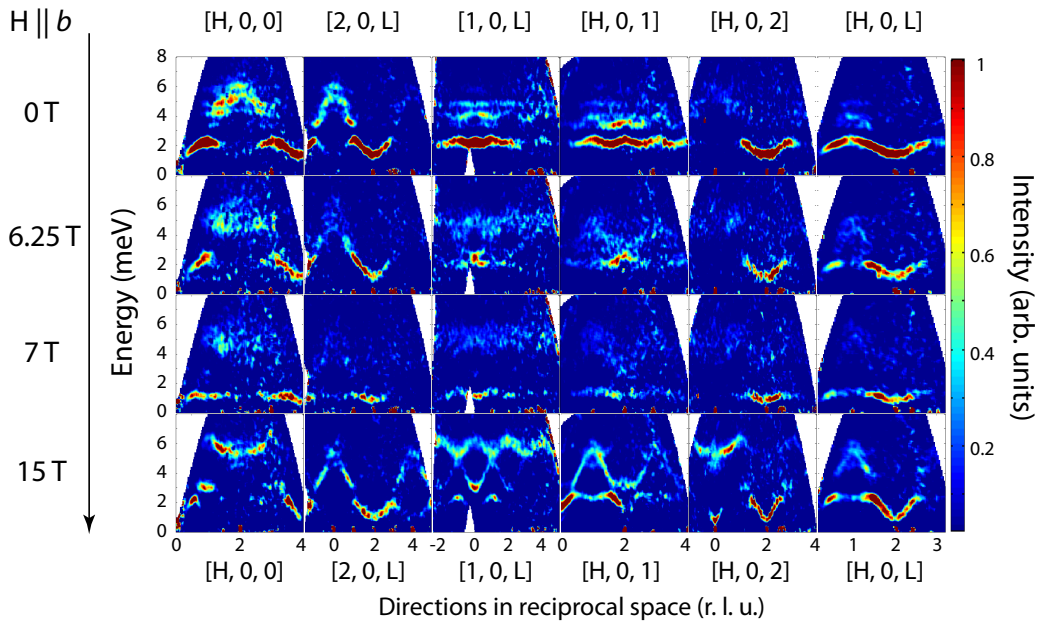

Figure 4.23: Representative Energy vs wave vector $\mathbf{Q}$ slices for various directions in reciprocal space. The integration range for each of these sets is ± 0.4 r.l.u. in K and ± 0.25 r.l.u. in either H or L direction. A $T = 30$ K high temperature paramagnetic background is subtracted from the data, which are corrected for detector efficiency. The measurements are shown for four different fields: 0, 6.25, 7 and 15 T (top to bottom row). Each of these fields characterizes one phase in the phase diagram.

these data shown have had the 30 K high temperature, zero field, paramagnetic background subtracted from them, and have been corrected for detector efficiency. The E vs $\mathbf{Q}$ maps were obtained by integration in the vertical K direction from ± 0.4 r.l.u. and in the horizontal by ± 0.25 r.l.u. in H and L around the position of interest. The complete spin wave spectrum has been mapped out, revealing the existence of at least six spin wave modes below 8 meV.

In zero field (top row of Fig. 4.23), the spectrum can be described in terms of two relatively broad bands of scattering, one at low energies of ~ 2 meV

containing two modes that are gapped from the elastic line by ~ 1.4 meV, and another one, gapped by ~ 1 meV from the lower energy set of modes is centered at higher energies, ~ 5 meV. This broad band displays fine structure within it related to another four spin wave branches.

The low energy modes exhibit appreciable softening down to $\Delta E \sim 1.4$ meV at the ferromagnetic Brillouin zone (BZ) centers at $(2,0,0)$, $(4,0,0)$ and $(2,0,2)$, while staying relatively flat everywhere else. The higher energy modes exhibit similar behavior, being strongly dispersive along the directions connecting the zone centers and weakly dispersive along the zone boundary. These modes appear to soften at the zone boundaries, complementary to the low energy modes which become flat there.

Under the application of magnetic fields, the excitation spectrum is seen to display a rich evolution. In moderate fields up to 6.25 T (second row from top in Fig. 4.23), it is seen that the modes in the top band become more diffuse and damped along most directions and appear to soften in energy. In particular, one branch seems to soften or hybridize with the lower energy modes at the zone boundary in 6.25 T, as can be seen at $(2,0,1)$, $(1,0,2)$ or $(2,0,1)$. The dispersion of the lower energy modes seems largely unaffected by a field of 6.25 T, however the spin gap to the elastic line has decreased and the scattering intensity has become weaker. At 7 T (second row from the bottom in Fig. 4.23), where the most dramatic change in the elastic scattering is observed, the higher energy band of excitations has effectively collapsed and only very diffuse, short-lived spin excitations survive. The lower energy branches have become very weak, the dispersion flattens and softens at an energy determined

by the single-ion anisotropy in the system. This is best seen at $\mathbf{Q} = (2, 0, 2)$, at which the spin wave softens to $\Delta E \sim 0.7$ meV, barely above the resolution limit of our measurements. Application of stronger fields leads to a gradual "re-organization" of the spin wave excitations in their location in reciprocal space and in their intensity distribution. The lower energy band gets lifted by the Zeeman energy in field for fields just exceeding 7 T, while the higher energy band first evolves into more well-defined spin waves that then are lifted in energy in a field of $\sim$ 13 T. Between 12 and 13 T, which is where the extrapolated phase transition occurs, based on magnetization measurements, no dramatic or abrupt change in the spin wave spectrum is observed. However, it appears that for fields above 13 T, and specifically at 15 T, no further modification to the dispersion or the lifetime of the excitations occurs. Overall the excitation spectrum gets lifted in energy continuously by the field, fully developing the gap between elastic line and the low energy band, as well as the gap between the low and high energy bands.

In this high field phase, the excitation spectrum exhibits a parabolic dispersion at the zone centers, however with anisotropic apparent spin wave velocities, and more pronounced dispersion than in zero field. The resulting spectrum displays a new gap structure, additional "soft" positions at $(2, 0, 1)$, for example, and a more complex dispersion in the higher energy spin wave band as well as a redistribution of spectral weight among the branches. These features are most obvious along three directions in reciprocal space, along [1,0,L], [H,0,1], and [H,0,L].

Along $[2, 0, L]$, the more diffuse, zero-field high energy more now shows a well defined, resolution-limited mode between ~ 2.8 and ~ 5 meV. This mode is separated by about 1 meV from the low energy band, which in turn, is gapped from the elastic line by only ~ 1 meV, compared to ~ 1.4 meV in zero field. Along $[1, 0, L]$, the lower energy band has lost almost all of its zero field intensity, whereas the higher energy band has split the ~ 2.5 meV zero field bandwidth into at least three visible modes extending over a slightly larger bandwidth, extending from ~ 3 meV to ~ 6.5 meV. One of these modes is sharp and resolution-limited and exhibits significant dispersion compared to any of the zero field modes along $[1, 0, L]$, while a band of relatively broad and less dispersive modes exists between 4.5-6 meV. Based on the energy width of this scattering, there are probably > 2 modes contained within that band.

Along $[H, 0, 1]$, the low energy band in zero field displays maxima at the $(1, 0, 1)$ and $(2, 0, 1)$ positions. By 15 T, this low energy dispersion has undergone a 180° phase shift, such that $(1, 0, 1)$ and $(2, 0, 1)$ now display a minimum in the dispersion. This change in dispersion actually occurs at the lower field transition near ~ 7 T, but it is most pronounced at 15 T. This is likely related to the antiferromagnetic arrangement of the spins on the cross-tie sites in the magnetic structure above 7 T, that is characterized by the appearance of the $(2, 0, 1)$ elastic peak in Fig. 4.22.

The change in the observed spin wave spectrum is shown in Fig. 4.24 in constant energy slices within the $[H, 0, L]$ plane for the high intensity, low energy modes around their maximum zero-field energies between $1.75 < E < 2.25$ meV, cutting through the dispersion surfaces there. Here we show how

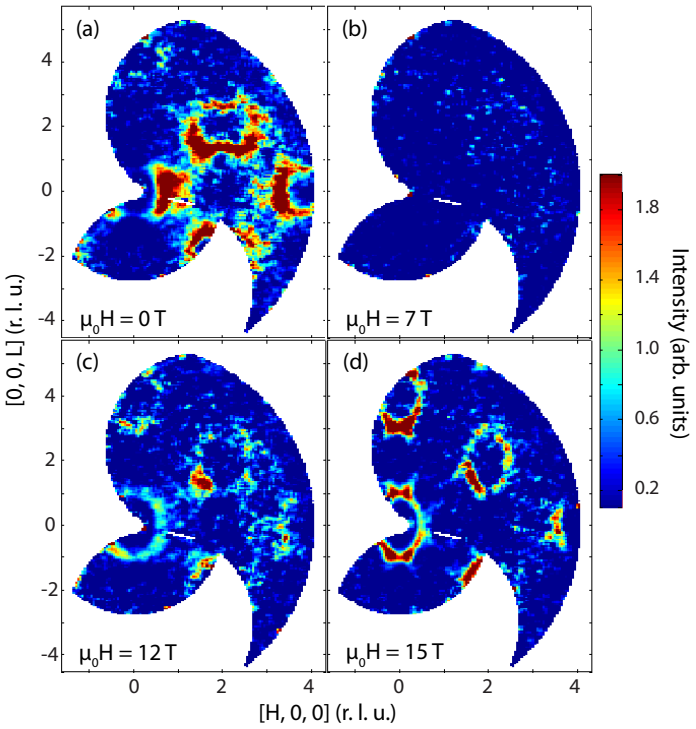

Figure 4.24: Constant energy slices for $1.75 < E < 2.25$ meV in the $[H, 0, L]$ plane in transverse magnetic fields of 0, 7, 12 and 15 T, cutting through the lowest lying dispersion surfaces. A distinct change in the nature of the spin fluctuations is observed as the transverse field increases.

the character of the fluctuations changes from zero field to 7 T, 12 T and 15 T. In zero field, where the cuts through the dispersion nicely reflect the symmetry of the Brillouin zone, the inelastic scattering intensity is strongest around the $[H, 0, 0]$ direction, indicating spin fluctuations along c. At 7 T, as previously noted, the spin excitations collapse and the low energy band disappears from our field of view here. In a larger field of 12 T, the overall scattering intensity appears weaker, but is redistributed in the $[H, 0, L]$ plane, now signaling fluctuations along both a and c. At the highest fields, the spin fluctuations now appear mostly along a as evidenced by strong scattering along

$[0, 0, L]$. This is consistent with an underlying magnetic spin structure in which the cross-tie moments point along c, and little or no fluctuations occur along the hard, b direction .

To better parametrize the gap closing at the observed quantum phase transitions at 6.25 and 7 T, we have taken energy cuts along specific $\mathbf{Q}$ points, approximating constant-$\mathbf{Q}$ cuts by integrating ± 0.2 in either H or L and ± 0.4 in K. These cuts focus only on the low energy behavior for $E < 3$ meV and are shown in Fig. 4.25 for three positions at $(2, 0, 1)$, $(1, 0, 0)$ and $(1, 0, 1)$ in panels (b) through (d), respectively. We consider only the lowest lying modes here as their energy dependence is easier to follow than that of the higher energy, more complex set of modes. The data have been corrected for detector efficiency but have no background subtracted from them, as we are comparing data taken at the same temperature in different fields. Panel (a) shows the field dependence of the energy at the center position of the low energy modes that were determined from fits to simple Gaussian lineshapes.

The energy gap at the three reciprocal space positions shows qualitatively similar behavior, as expected from the energy vs wave vector slices already discussed above. They all are weakly field-dependent below 6.25 T and get drastically suppressed at 7 T. Upon further increasing the applied field, the gap energies increase again. In particular, the field dependence of the energy gap at the $(2, 0, 2)$ position shows the gap closing in an order parameter-like fashion for a critical field of $\sim$7 T. The energy gaps at $(1, 0, 0)$ and $(1, 0, 1)$ show a more discontinuous change at 7 T, and their gaps are suppressed by > 1 meV from their value just below the phase transition. In larger fields, the

gaps slowly re-open, with a more pronounced field-induced lifting of the lower modes for the $(1, 0, 1)$ and $(1, 0, 0)$ positions. From the data at the highest fields, between 12 and 15 T, no dramatic changes indicative of a first order phase transition are observed, as the gaps evolve continuously up to the highest field of 15 T.

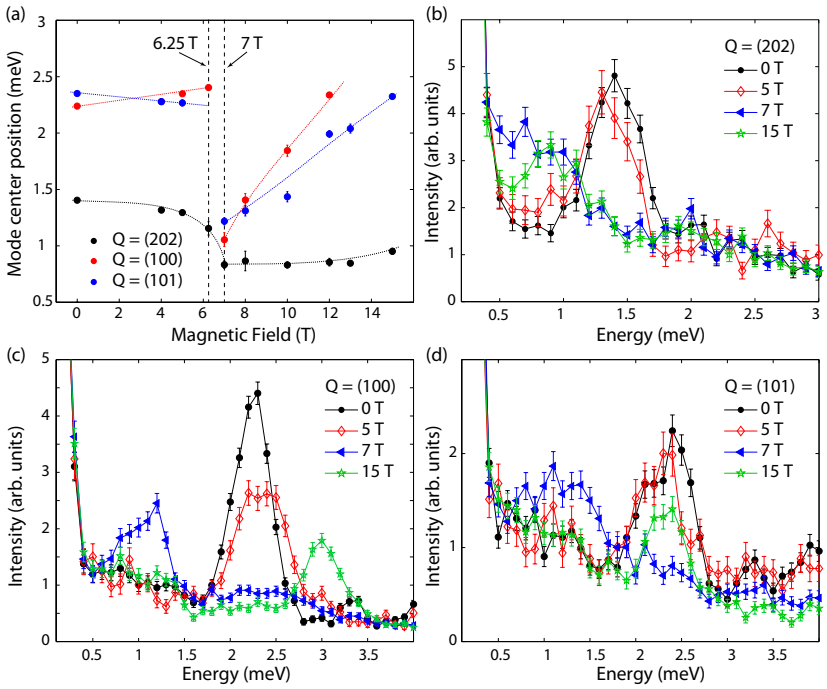

Figure 4.25: Magnetic field dependence of the lowest lying spin wave modes $E < 3.5$ meV and the evolution of their spin gaps ΔE. Data is shown for three positions, $\mathbf{Q} = (2, 0, 2)$, $(1, 0, 0)$, $(1, 0, 1)$. Panel (a) shows the center positions in energy of each mode, determined by a fit to a Gaussian lineshape. The phase transitions are indicated by dashed vertical lines. Dotted lines are meant as guide to the eyes. Panels (b) through (d) show representative data sets and energy scans for the $\mathbf{Q}$ positions shown in panel (a): $(2, 0, 2)$ in panel (b), $(1, 0, 0)$ in panel (c), and $(1, 0, 1)$ in panel (d). The binning ranges for these scans are ± 0.2 r.l.u. in H or L and ± 0.4 r.l.u. in K. The data are corrected for detector efficiency only.

The lack of an abrupt signature for a phase transition at $\sim$ 13 T from the spin fluctuations is consistent with a continuous phase transition. The intervention of the incommensurate phases between the low field ferromagnetic phase and the high field phase implies that the overall evolution of the spin waves emanating out of the low and high field structures can be gradual and continuous, even if some of the steps in this evolution, such as the ferromagnetic to incommensurate I transition, are not. However, what is more surprising is the fact that the magnetic structure at 15 T is not consistent with a scenario in which all moments are polarized along the field, as one would expect for a polarized paramagnet. This raises the question as to how the low temperature, high-field phase is connected to the high temperature, zero-field paramagnetic state above 11.2 K. The broken symmetry phase we observe at 15 T and 1.6 K must transform through thermal fluctuations into the restored symmetry phase at 0 T and 11.2 K. An understanding how this may occur is still lacking. Our magnetization measurements did not reveal any further features indicative of a transition at high fields and intermediate temperatures, however, already the signature for the transition at 13 T is quite weak. It is also possible that there is no conventional phase transition from the thermal paramagnet to the quantum paramagnet we observe, but that this "transition" has more of a crossover character, perhaps driven by the two-dimensionality of the system.

Finally, we show a constant-$\mathbf{Q}$ cut at $(1, 0, 0)$ in Fig. 4.26 as measured in two different experimental environments. We compare here cold triple-axis data measured at a temperature of 50 mK on FLEX, HZB, with data obtained at a temperature of $T = 1.6$ K on the cold neutron chopper spectrometer

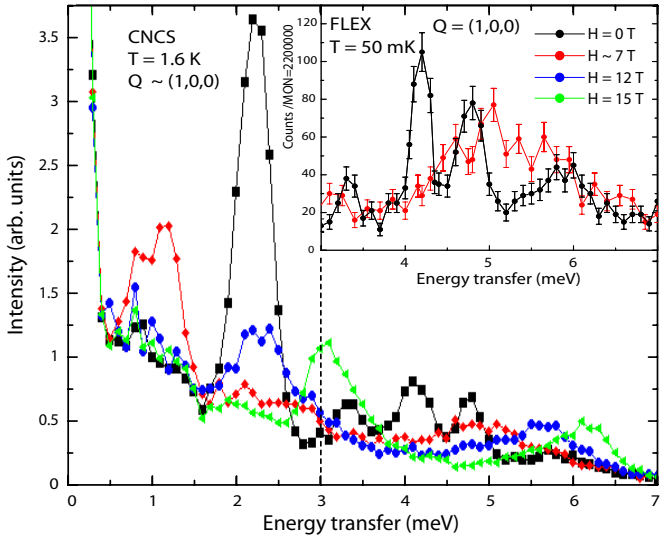

Figure 4.26: Comparison of a constant **Q**-cut from cold triple axis data taken with $E_f = 3.5$ meV at FLEX, HZB and time-of-flight data from CNCS, SNS, taken at $E_i = 12$ meV. Data at 50 mK (FLEX) and 1.6 K (CNCS) are both taken at $T \ll T_C$ and look qualitatively the same, in zero field and at 7 T. The zero-field measurement showed for the first time the existence of six spin wave branches, two at energies < 3 meV, and four at energies of $3 < E < 7$ meV. The integration range for the constant **Q**-cut at $(1, 0, 0)$ on CNCS was ± 0.1 r.l.u. in H and L and ± 0.4 r.l.u. in K. CNCS data are corrected for detector efficiency only.

CNCS, SNS. Apart from a slight broadening due to instrumental resolution, the CNCS data at the higher temperature look qualitatively similar to the data taken on FLEX. In zero field, six modes are observed (the lowest energy band at ~ 2.2 meV actually contains two branches). At the transition at 7 T, this low energy band is suppressed in energy, while the higher energy modes become weak and diffuse, typical of incommensurate or disordered systems. At higher fields, a reorganization of the spin excitations takes place. Moreover, the similarity between the 50 mK and 1.6 K data implies that thermal fluctuations play little role in the evolution of the phases and their spin fluctuations we

have presented earlier. At $T = 1.6$ K we are truly probing the transverse field-induced quantum fluctuations in this system. This is not so surprising given that 1.6 K is deep within the $H = 0$ ferromagnetic ground state and one which is separated by intermediate incommensurate phases by a strongly first order phase transition at $T_{\rm C} = 6.2$ K.

4.3.5 Conclusions

We have reported on transverse field induced quantum phase transitions in the quasi two-dimensional kagome staircase material $Co_3V_2O_8$, which we investigated using magnetization and neutron scattering techniques in a magnetic field applied transverse to the ferromagnetic easy axis of the system. From magnetization measurements, we found three quantum critical points at low temperature at fields of $H_{c1} \sim 6.25$ T, $H_{c2} \sim 7$ T and $H_{c3} \sim 13$ T. The lower two transitions are also observed and confirmed by elastic and inelastic neutron scattering measurements. These transitions appear as change in the magnetic structure (6.25 T) from FM to IC AFM I and as change in both magnetic structure (IC AFM I to IC AFM II) and spin excitation spectrum (7 T). In particular, the spin fluctuations get almost completely suppressed as indicated by the collapse of the high energy modes and the near-closing of the lowest energy gaps at 7 T. In higher fields, the spin excitation spectrum is characterized by a more complex set of dispersion relations with different energy gaps. Our neutron scattering data are not sensitive to the transition at 13 T, instead a gradual evolution across this phase boundary is observed.

This may reflect the continuous nature of this transition at high transverse fields in a quasi two-dimensional kagome plane system.

Moreover, we observe for the first time and in detail six spin wave branches in different fields, revealing that the system is more complex than previously thought. The mapping out of the spin wave dispersions and intensities as displayed in Fig. 4.23 are sufficiently detailed that a determination of a robust spin Hamiltonian, at least in the relatively simple ferromagnetic state at low fields and in the highest field ordered state, using linear spin wave theory should be possible. This would then underlie a thorough understanding of the QPTs at $H_{c1} \sim 6.25$ T, $H_{c2} \sim 7$ T and $H_{c3} \sim 13$ T. While this is beyond the scope of the present work, such analysis may well elevate our understanding of this quasi two-dimensional Ising system in a transverse field to that of both the three-dimensional analogue $LiHoF_4$,[51,52] and the quasi one-dimensional analogue $CoNb_2O_6$.

Work at McMaster University was supported by NSERC of Canada. The research at Oak Ridge National Laboratory's Spallation Neutron Source was sponsored by the Scientific User Facilities Division, Office of Basic Energy Sciences, U.S. Department of Energy. The data were reduced using Mantid[58] and analysed using the HORACE software package.[59] The authors would like to thank O. Petrenko for fruitful discussions.

4.4 * References

[1] G. Balakrishnan, O. A. Petrenko, M. R. Lees, and D. M. Paul, J. Phys.: Condens. Matter **16**, L347 (2004).

[2] M. Kenzelmann, A. B. Harris, A. Aharony, O. Entin-Wohlman, T. Yildirim, Q. Huang, S. Park, G. Lawes, C. Broholm, N. Rogado, R. J. Cava, K. H. Kim, G. Jorge, and A. P. Ramirez, Phys. Rev. B **74**, 014429 (2006).

[3] Y. Chen, J. W. Lynn, Q. Huang, F. M. Woodward, T. Yildirim, G. Lawes, A. P. Ramirez, N. Rogado, R. J. Cava, A. Aharony, O. Entin-Wohlman, and A. B. Harris, Phys. Rev. B **74**, 014430 (2006).

[4] R. Szymczak, M. Baran, R. Diduszko, J. Fink-Finowicki, M. Gutowska, A. Szewczyk, and H. Szymczak, Phys. Rev. B **73**, 094425 (2006).

[5] M. Ramazanoglu, C. P. Adams, J. P. Clancy, A. J. Berlinsky, Z. Yamani, R. Szymczak, H. Szymczak, J. Fink-Finowicki, and B. D. Gaulin, Phys. Rev. B **79**, 024417 (2009).

[6] J. D. Pless, N. Erdman, D. Ko, L. D. Marks, P. C. Stair, and K. R. Poeppelmeier, Cryst. Growth Des. **3**, 615 (2003).

[7] E. E. Sauerbrei, R. Faggiani, and C. Calvo, Acta Cryst. B **29**, 2304 (1973).

[8] N. Krishnamachari and C. Calvo, Can. J. Chem. **49**, 1629 (1971).

[9] P.-L. Wang, P.-E. Werner, and A. G. Nord, Z. Kristallographie **198**, 271 (1992).

[10] M. Sahimi, in *Applications of Percolation Theory* (Taylor and Francis, London, 1994), p. 11.

[11] A. P. Ramirez, Annu. Rev. Mater. Sci. **24**, 453 (1994).

[12] C. Lacroix, P. Mendels, and F. Mila, in *Introduction to Frustrated Magnetism* (Springer Series in Solid-State Sciences, Heidelberg, 2011).

[13] N. Rogado, G. Lawes, D. A. Huse, A. P. Ramirez, and R. J. Cava, Solid State Commun. **124**, 229 (2002).

[14] N. Rogado, M. K. Haas, G. Lawes, D. A. Huse, A. P. Ramirez, and R. J. Cava, J. Phys.: Condens. Matter **15**, 907 (2003).

[15] E. Morosan, J. Fleitman, T. Klimczuk, and R. J. Cava, Phys. Rev. B **76**, 144403 (2007).

[16] G. Lawes, M. Kenzelmann, N. Rogado, K. H. Kim, G. A. Jorge, R. J. Cava, A. Aharony, O. Entin-Wohlman, A. B. Harris, T. Yildirim, Q. Z. Huang, S. Park, C. Broholm, and A. P. Ramirez, Phys. Rev. Lett. **93**, 247201 (2004).

[17] N. R. Wilson, O. A. Petrenko, and L. C. Chapon, Phys. Rev. B **75**, 094432 (2007).

[18] N. Qureshi, M. Zbiri, J. Rodriguez-Carvajal, A. Stunault, E. Ressouche, T. C. Hansen, M. T. Fernandez-Diaz, M. R. Johnson, H. Fuess, H. Ehrenberg, Y. Sakurai, M. Itou, B. Gillon, T. Wolf, J. A. Rodriguez-Velamazan, and J. Sanchez-Montero, Phys. Rev. B **79**, 094417 (2009).

[19] O. A. Petrenko, N. R. Wilson, G. Balakrishnan, D. M. Paul, and G. J. McIntyre, Phys. Rev. B **82**, 104409 (2010).

[20] J. S. Helton, Y. Chen, G. L. Bychkov, S. N. Barilo, N. Rogado, R. J. Cava, and J. W. Lynn, J. Phys.: Condens. Matter **24**, 016003 (2012).

[21] R. C. Rai, J. Cao, L. I. Vergara, S. Brown, J. L. Musfeldt, D. J. Singh, G. Lawes, N. Rogado, R. J. Cava, and X. Wei, Phys. Rev. B **76**, 174414 (2007).

[22] L. I. Vergara, J. Cao, L. C. Tung, N. Rogado, F. Yen, Y. Q. Wang, R. J. Cava, B. Lorenz, Y. J. Wang, and J. L. Musfeldt, Phys. Rev. B **81**, 012403 (2010).

[23] T. Lancaster, S. J. Blundell, P. J. Baker, D. Prabhakaran, W. Hayes, and F. L. Pratt, Phys. Rev. B **75**, 064427 (2007).

[24] A. Smol'nikov, V. Ogloblichev, A. Sadykov, Y. Piskunov, A. Gerashchenko, S. Verkhovskii, A. Yakubovskii, S. Barilo, G. Bychkov, and S. Shiryaev, J. Exp. Theor. Phys. **112**, 1020 (2011).

[25] V. Ogloblichev, K. Kumagai, A. Yakubovsky, K. Mikhalev, Y. Furukawa, S. Verkhovskii, A. Gerashenko, S. Barilo, G. Bychkov, S. Shiryaev, and A. Korolev, J. Phys.: Conf. Series **150**, 042148 (2009).

[26] N. Qureshi, H. Fuess, H. Ehrenberg, T. C. Hansen, C. Ritter, P. Adelmann, C. Meingast, T. Wolf, Q. Zhang, and W. Knafo, J. Phys.: Condens. Matter **20**, 095219 (2008).

[27] N. Qureshi, H. Fuess, H. Ehrenberg, B. Ouladdiaf, J. Rodriguez-Carvajal, T. C. Hansen, T. Wolf, C. Meingast, Q. Zhang, W. Knafo, and H. v Lohneysen, J. Phys.: Condens. Matter **20**, 235228 (2008).

[28] R. J. Birgeneau, R. A. Cowley, G. Shirane, and H. Yoshizawa, J. Stat. Phys. **34**, 817 (1984).

[29] J. van Duijn, B. D. Gaulin, M. A. Lumsden, J. P. Castellan, and W. J. L. Buyers, Phys. Rev. Lett. **92**, 077202 (2004).

[30] R. B. Griffiths, Phys. Rev. Lett. **23**, 17 (1969).

[31] H. A. Dabkowska and A. B. Dabkowski, in *Crystal Growth of Oxides by Optical Floating Zone Technique. Experimental Approach to Defects Determination* (Springer Handbook of Crystal Growth, Defects and Characterization, Berlin, Heidelberg, New York, Tokyo, 2010), pp. 367–392.

[32] K. Fritsch, M. Ramazanoglu, H. A. Dabkowska, and B. D. Gaulin, J. Cryst. Growth **327**, 205 (2011).

[33] J. Copley and J. Cook, Chem. Phys. **292**, 477 (2003).

[34] See Supplemental Material for magnetization data along different crystallographic axes of the two single crystal samples (x=0.029 and x=0.194) studied in this paper, [http://link.aps.org/supplemental/10.1103/PhysRevB.86.174421].

[35] N. R. Wilson, O. A. Petrenko, and G. Balakrishnan, J. Phys.: Condens. Matter **19**, 145257 (2007).

[36] M. F. Sykes and J. W. Essam, J. Math. Phys. **5**, 1117 (1964).

[37] J. W. Essam, Rep. Prog. Phys. **43**, 833 (1980).

[38] D. Stauffer, Phys. Rep. **54**, 1 (1979).

[39] D. S. Gaunt and M. F. Sykes, J. Phys. A: Math. Gen. **16**, 783 (1983).

[40] A. J. Bray, Phys. Rev. Lett. **59**, 586 (1987).

[41] M. E. Fisher, Physics **3**, 255 (1967).

[42] Y. J. Uemura and R. J. Birgeneau, Phys. Rev. Lett. **57**, 1947 (1986).

[43] R. T. Azuah, L. R. Kneller, Y. Qiu, P. L. W. Tregenna-Piggott, C. M. Brown, J. R. D. Copley, and R. M. Dimeo, J. Res. Natl. Inst. Stan. Technol. **114**, 341 (2009).

[44] Q. Si and F. Steglich, Science **329**, 1161 (2010).

[45] S. Sachdev, *Quantum Phase Transitions* (Cambridge University Press, New York, 2000).

[46] G. Oomi, M. Ohashi, Y. Uwatoko, I. Satoh, and T. Komatsubara, Physica B: Condens. Matter **359361**, 65 (2005), ¡ce:title¿Proceedings of the International Conference on Strongly Correlated Electron Systems¡/ce:title¿.

[47] P. Coleman, A. Schroeder, G. Aeppli, R. Coldea, M. Adams, O. Stockert, H. Loehneysen, E. Bucher, and R. Ramazashvili, Nature **407**, 351 (2000).

[48] O. Stockert, H. v. Löhneysen, A. Rosch, N. Pyka, and M. Loewenhaupt, Phys. Rev. Lett. **80**, 5627 (1998).

[49] H. Pfau, S. Hartmann, U. Stockert, P. Sun, S. Lausberg, M. Brando, S. Friedemann, C. Krellner, C. Geibel, S. Wirth, and et al., Nature **484**, 493 (2012).

[50] P. Gegenwart, J. Custers, C. Geibel, K. Neumaier, T. Tayama, K. Tenya, O. Trovarelli, and F. Steglich, Phys. Rev. Lett. **89**, (2002).

[51] H. M. Ronnow, Science **308**, 389 (2005).

[52] D. Bitko, T. Rosenbaum, and G. Aeppli, Phys. Rev. Lett. **77**, 940 (1996).

[53] R. Coldea, D. A. Tennant, E. M. Wheeler, E. Wawrzynska, D. Prabhakaran, M. Telling, K. Habicht, P. Smeibidl, and K. Kiefer, Science **327**, 177 (2010).

[54] G. Ehlers, A. A. Podlesnyak, S. E. Hahn, R. S. Fishman, O. Zaharko, M. Frontzek, M. Kenzelmann, A. V. Pushkarev, S. V. Shiryaev, and S. Barilo, Phys. Rev. B **87**, 214418 (2013).

[55] K. Fritsch, Z. Yamani, S. Chang, Y. Qiu, J. R. D. Copley, M. Ramazanoglu, H. A. Dabkowska, and B. D. Gaulin, Phys. Rev. B **86**, 174421 (2012).

[56] G. Ehlers, A. A. Podlesnyak, J. L. Niedziela, E. B. Iverson, and P. E. Sokol, Rev. Sci. Instrum. **82**, 085108 (2011).

[57] Y. Yasui, Y. Kobayashi, M. Soda, T. Moyoshi, M. Sato, N. Igawa, and K. Kakurai, J. Phys. Soc. Jpn. **76**, 034706 (2007).

[58] http://www.mantidproject.org/ (2012).

[59] T. G. Perring, R. A. Ewings, and J. V. Duijn, http://horace.isis.rl.ac.uk, and unpublished (2009).

Chapter 5

The Pyrochlore Spin Liquid Candidate $Tb_2Ti_2O_7$

This chapter includes two articles on neutron scattering measurements on $Tb_2Ti_2O_7$ that were motivated by the continual debate about the nature of $Tb_2Ti_2O_7$'s low temperature ground state.

Our first set of experiments was aimed at measuring the field-induced spin wave spectrum in sufficient detail to possibly allow us to extract the microscopic Hamiltonian in a similar approach as used successfully by our group on $Yb_2Ti_2O_7$. These measurements led to the surprising discovery of well-defined elastic diffuse scattering at $(\frac{1}{2},\frac{1}{2},\frac{1}{2})$ positions in reciprocal space at 80 mK that we modeled as "short-range antiferromagnetic spin ice". In addition, we were able to resolve for the first time very low-energy magnetic inelastic scattering, separated by a small energy gap from the elastic line. We associated this inelastic signal with the presence of the magnetic diffuse elastic scattering and showed that both disappear under the application of a small magnetic field and upon elevating temperature.

This work is presented in Section 5.1 of this chapter that incorporates the article *"Antiferromagnetic spin ice correlations at* $(\frac{1}{2}, \frac{1}{2}, \frac{1}{2})$ *in the ground state of the pyrochlore magnet* $Tb_2Ti_2O_7$*"*, which has been published in Physical Review B. The full reference is given below:

K. Fritsch, K. A. Ross, Y. Qiu, J. R. D. Copley, T. Guidi, R. I. Bewley, H. A. Dabkowska, and B. D. Gaulin. Physical Review B **87**, 094410 (2013).*

Figures 5.1-5.6 are reproduced from said article with permission.

Motivated by the work above, we performed a parametric study of the short-range antiferromagnetic spin ice correlations as a function of magnetic field and temperature.

This work is included in Section 5.2 as preprint *"Temperature and Magnetic Field Dependence of Spin Ice Correlations in the Pyrochlore Magnet* $Tb_2Ti_2O_7$*"*, which is intended for submission to Physical Review B.

In this paper, we propose a new low-field low-temperature phase diagram of $Tb_2Ti_2O_7$, showing that the $(\frac{1}{2}, \frac{1}{2}, \frac{1}{2})$ scattering corresponds to a frozen spin ice phase below 275 mK and for fields below 0.075 T and that this phase exhibits spin glass characteristics. This frozen phase can also been associated with the proposed quantum spin ice phase proposed by Yin *et al.* based on their magnetization measurements. We are also able to demonstrate that the low-lying inelastic scattering is indeed related to the frozen spin ice state and that it cannot be understood in terms of a nonmagnetic singlet ground state scenario also proposed in the literature. Finally, based on reports on non-stoichiometric, "stuffed" polycrystalline samples of $Tb_{2+x}T_{2-x}O_7$ that revealed

* ©(2013) The American Physical Society

a sharp peak in the specific heat as well as diffuse elastic scattering at $(\frac{1}{2}, \frac{1}{2}, \frac{1}{2})$ for slightly stuffed samples ($x = 0.005$), our collaborators at the University of Waterloo (David Pomaranski and Jan Kycia) measured the specific heat on a piece of our single crystal. They find a sharp peak in the specific heat at 450 mK, indicating that this anomaly is not related to the onset of the short-range magnetic order that we observe at 275 mK. At present, the origin of the specific heat peak remains unclear, and further studies will be needed to determine if and how this peak relates to the magnetic degrees of freedom in $Tb_2Ti_2O_7$.

5.1 Antiferromagnetic Spin Ice Correlations at $(\frac{1}{2},\frac{1}{2},\frac{1}{2})$ in the Ground State of the Pyrochlore Magnet $Tb_2Ti_2O_7$

K. Fritsch,[1] K. A. Ross,[1,2,3] Y. Qiu,[3,4] J. R. D. Copley,[3] T. Guidi,[5] R. I. Bewley,[5] H. A. Dabkowska,[6] and B. D. Gaulin[1,6,7]

[1]*Department of Physics and Astronomy, McMaster University, Hamilton, Ontario, L8S 4M1, Canada*

[2]*Institute for Quantum Matter and Department of Physics and Astronomy, Johns Hopkins University, Baltimore, Maryland 21218, USA*

[3]*NIST Center for Neutron Research, NIST, Gaithersburg, Maryland 20899-8102, USA*

[4]*Department of Materials Science and Engineering, University of Maryland, College Park, Maryland 20742, USA*

[5]*ISIS Pulsed Neutron and Muon Facility, Rutherford Appleton Laboratory, Chilton, Didcot OX11 0QX, UK*

[6]*Brockhouse Institute for Materials Research, Hamilton, Ontario, L8S 4M1, Canada*

[7]*Canadian Institute for Advanced Research, 180 Dundas St. W., Toronto, Ontario, M5G 1Z8, Canada*

Abstract

We present high-resolution single-crystal time-of-flight neutron scattering measurements on the candidate quantum spin liquid pyrochlore $Tb_2Ti_2O_7$ at low temperature and in a magnetic field. At $\sim$ 70 mK and in zero field, $Tb_2Ti_2O_7$ reveals diffuse magnetic elastic scattering at $(\frac{1}{2},\frac{1}{2},\frac{1}{2})$ positions in reciprocal space, consistent with short-range correlated regions based on a two-in, two-out spin ice configuration on a doubled conventional unit cell.

This elastic scattering is separated from very low-energy magnetic inelastic scattering by an energy gap of $\sim 0.06-0.08$ meV. The elastic signal disappears under the application of small magnetic fields and upon elevating temperature. Pinch-point-like elastic diffuse scattering is observed near (1,1,1) and (0,0,2) in zero field at ~ 70 mK, in agreement with Fennell *et al.* [Phys. Rev. Lett. **109**, 017201 (2012)] supporting the quantum spin ice interpretation of $Tb_2Ti_2O_7$.

5.1.1 Introduction

Geometrically frustrated magnets have been intensely studied over the course of the last decade due to the rich variety of unconventional ground states they display. [1] In particular, the magnetic rare-earth titanate pyrochlore oxides with the chemical formula $R_2Ti_2O_7$ have received considerable attention.[2] In this structure, trivalent R^{3+} rare-earth metal ions occupy a network of corner-sharing tetrahedra known as the pyrochlore lattice, which is the prototypical example of geometric frustration in three dimensions. The interplay between exchange and dipolar interactions with crystal-field (CF) induced anisotropy on the underlying pyrochlore lattice leads to a variety of exotic phenomena. These include ground state selection by order-by-disorder,[3,4] as well as classical[5–8] and quantum spin ice [9–14] physics.

$Tb_2Ti_2O_7$ has attracted much interest as a potential experimental realization of a quantum spin liquid,[15] based on its lack of long-range order (LRO) down to at least 50 mK [16,17] despite a Curie Weiss temperature of ~ -14 K.[18] The Tb^{3+} ions in $Tb_2Ti_2O_7$ have an Ising CF doublet ground state that leads to $\langle 111 \rangle$ easy-axis anisotropy as in the canonical spin ice materials $Ho_2Ti_2O_7$

and $Dy_2Ti_2O_7$. In contrast to these spin ices however, the net exchange in $Tb_2Ti_2O_7$ is antiferromagnetic (AF). Since the combination of Ising-like $\langle 111 \rangle$ anisotropy and AF interactions on the pyrochlore lattice is unfrustrated,[19] $Tb_2Ti_2O_7$ is naively expected to display a unique LRO ground state.

Recently, two theoretical pictures have sought to explain its enigmatic ground state. One of these proposed a "quantum spin ice" (QSI) scenario for the disordered ground state in $Tb_2Ti_2O_7$.[20,21] This scenario invokes virtual quantum excitations between the CF ground state doublet and the first excited doublet ($\Delta \sim 15$ K) that reposition $Tb_2Ti_2O_7$ into the spin ice regime. Jahn-Teller physics and a non-magnetic singlet ground state have also been proposed and debated [22,23] as the cause underlying its failure to order.

In this paper, we report new neutron scattering measurements on single crystalline $Tb_2Ti_2O_7$ that elucidate the nature of its ground state. Our measurements were performed in zero field and in magnetic fields applied along two high-symmetry directions in the pyrochlore lattice. The zero field measurements reveal short-range AF spin ice correlations extending over roughly two conventional unit cells, characterized by elastic diffuse scattering around $(\frac{1}{2},\frac{1}{2},\frac{1}{2})$ positions in reciprocal space. The previously reported checkerboard-pattern of diffuse scattering [24,25] is now resolved as low-energy inelastic scattering for 0.06 meV $< E <$ 0.6 meV, while the higher-energy inelastic scattering regime for 0.8 meV $< E <$ 2.0 meV is dominated by CF excitations, in agreement with earlier studies.[18,26] A model of the elastic scattering intensity involving 128 spins in a doubled conventional unit cell is presented. A fit of this model to the observed peak intensities suggests that the Tb^{3+} moments

form an AF ordered spin ice configuration with spins tilted $\sim 12^{\circ}$ from their local $\langle 111 \rangle$ axes. Finally, pinch-point-like diffuse elastic scattering is observed near (0,0,2) in zero field. These results suggest that $Tb_2Ti_2O_7$ may well form a long-range ordered (LRO) equilibrium state based on this spin ice-derived structure at lower temperatures, although this might require more pristine samples than are currently available.

5.1.2 Experimental Details

The single-crystal sample of $Tb_2Ti_2O_7$ used for both neutron scattering measurements was grown using the optical floating zone technique at McMaster University. [27,28] It is the same single crystal used in an earlier study by Rule *et al.*[25] Time-of-flight neutron scattering measurements were performed using the disk-chopper spectrometer DCS[29] at the NIST Center for Neutron Research and the LET spectrometer[30] at the ISIS Spallation Neutron Source. For the DCS measurements, incident neutrons of energy $E_i = 3.27$ meV were employed, giving an energy resolution of 0.1 meV. The sample was carefully aligned with the [1-10] direction vertical to within 0.5°, such that the [H,H,L] plane was coincident with the horizontal scattering plane. In the LET experiment, high-resolution measurements using $E_i = 2.32$ meV gave an energy resolution of 0.02 meV. At LET, the sample was aligned with the [11-1] direction vertical, placing the plane spanned by [H,H,2H] and [H,-H,0] within the horizontal scattering plane. Both DCS and LET experiments achieved a base temperature of $\sim$ 70 mK and maximum magnetic fields of $\mu_0 H = 10$ T and $\mu_0 H = 7$ T, respectively.

5.1.3 Results and Discussion

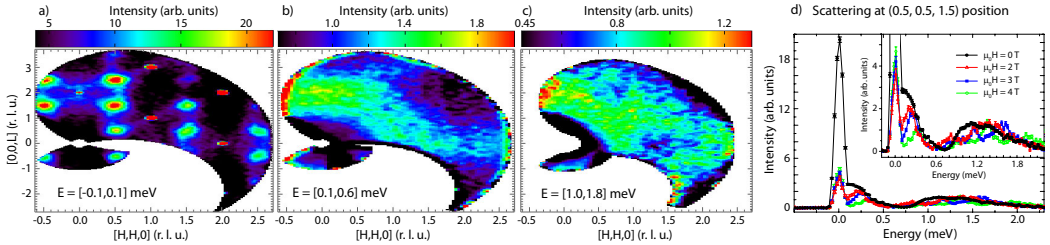

Figure 5.1: Neutron scattering data within the (H,H,L) plane of $Tb_2Ti_2O_7$ at $T = 70$ mK are shown for (a) -0.1 meV $< E <$ 0.1 meV, (b) 0.1 meV $< E <$ 0.6 meV and (c) 1.0 $< E <$ 1.8 meV. Panel (d) shows a plot of intensity vs energy transfer at the $(\frac{1}{2},\frac{1}{2},\frac{3}{2})$ position for fields $\mu_0 H = 0, 2, 3$, and 4 T. The integration range is $H = [0.2, 0.8]$ r.l.u., $L = [1.2, 1.8]$ r.l.u.. The inset expands the intensity scale. All data shown were corrected for detector efficiency, and an empty can background was subtracted. The error bars are $\pm 1\sigma$.

Figures 5.1(a)-5.1(c) show reciprocal lattice maps in the [H,H,L] plane in zero field, taken at $T \sim 70$ mK on DCS. The data were corrected for detector efficiency and to eliminate scattering from the sample environment. Figure 5.1(a) shows data in the elastic channel, integrating over -0.1 meV $< E <$ 0.1 meV. These data reveal strong diffuse elastic scattering at $(\frac{1}{2},\frac{1}{2},\frac{1}{2})$-type positions in reciprocal space. Cuts through the diffuse elastic scattering at $(\frac{3}{2},\frac{3}{2},\frac{3}{2})$ are shown in Fig. 5.2, for each of the [H,H,0], [H,H,H] and [0,0,L] directions, along with fits of this scattering to a standard Ornstein-Zernike (Lorentzian) form. As can be seen from Fig. 5.2, the diffuse elastic scattering is isotropic in $\mathbf{Q}$, and characterized by a correlation length of $\xi = 8.0 \pm 0.6$ Å. This corresponds to a correlated static magnetic region of diameter $2\xi = 16$ Å or roughly two conventional unit cells. The elastic scattering we observe indicates spins which are static on the time scale of our energy resolution, $\sim 10^{-10}$ s.

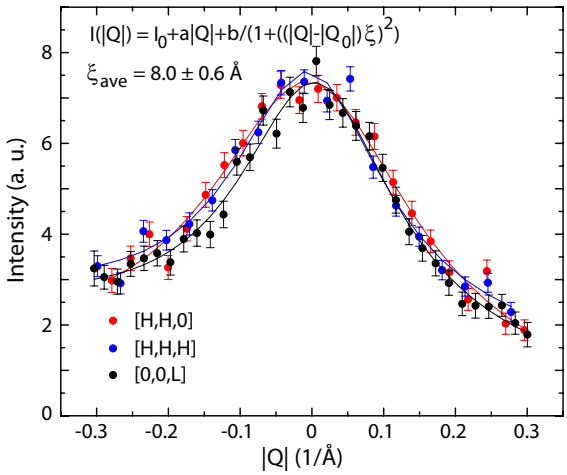

Figure 5.2: Cuts of the elastic scattering data in Fig.5.1(a) through the $(\frac{3}{2},\frac{3}{2},\frac{3}{2})$ position along each of the [H,H,0], [H,H,H], and [0,0,L] directions are shown, along with fits to an Ornstein-Zernike form for the diffuse lineshape. These data and associated fits show the short-range ordered, elastic antiferromagnetic Bragg features to be isotropic in **Q**, and characterized by a correlation length of ∼8 Å.

Figure 5.1(b) shows the low-lying inelastic scattering for 0.1 meV $< E <$ 0.6 meV. Within our energy resolution, this scattering appears to be nearly quasi-elastic and forms the distinct checkerboard pattern observed previously [24] with highest intensities near (0,0,2) and (2,2,0) in the [H,H,L] plane. Interestingly, this feature has boundaries formed by the $(\frac{1}{2},\frac{1}{2},\frac{1}{2})$ diffuse elastic scattering. The higher energy inelastic scattering for 1.0 meV $< E <$ 1.8 meV is shown in Fig. 5.1(c). This intensity results from excitations to the lowest excited CF doublet states at $\Delta \sim 1.2$ meV. Figure 5.1(d) shows the intensity around the $(\frac{1}{2},\frac{1}{2},\frac{3}{2})$ position as a function of energy for selected magnetic fields. The zero field data nicely illustrate the three distinct energy regimes that are mapped in reciprocal space in Figs. 5.1(a)-5.1(c). Under the application of a 2 T field, the zero field elastic scattering at the $(\frac{1}{2},\frac{1}{2},\frac{3}{2})$ and related positions drops to one-seventh of the initial intensity, as the elastic magnetic scattering

has been eliminated, leaving only nuclear incoherent scattering at the $(\frac{1}{2},\frac{1}{2},\frac{3}{2})$ position. The low-lying inelastic scattering displays a clear peak at ~ 0.2 meV at 2 T. This feature moves to higher energies and fades in intensity in larger magnetic fields. The broad, higher energy inelastic scattering from the CF excitations also splits in the presence of a [1-10] magnetic field, forming spin wave bands that were previously reported.[25]

The new elastic diffuse scattering at $(\frac{1}{2},\frac{1}{2},\frac{1}{2})$ and related wave vectors can be well described by a model based on a "two-in, two-out" spin ice arrangement which extends over two conventional unit cells in all three dimensions, leading to a supercell composed of eight conventional unit cells. This model takes into account (a) the observed phase shift of π between neighboring unit cells giving rise to scattering at $(\frac{1}{2},\frac{1}{2},\frac{1}{2})$ positions and (b) the observed width of the diffuse scattering. The spin arrangement over two neighboring cells in the xy plane is shown in Fig. 5.3(c). Note that the black spins are reversed in their neighboring cell (grey spins) along the x or y directions.

We calculate the neutron scattering intensity $S(\mathbf{Q})$ that is proportional to the square of the transverse component of the magnetic structure factor $|M_{\perp}(\mathbf{Q})|^2 = |\mathbf{Q}\times\mathbf{M}(\mathbf{Q})\times\mathbf{Q}|^2$ with $\mathbf{M}(\mathbf{Q}) = \sum_j f_j(\mathbf{Q})\cdot\mathbf{m}_j\cdot e^{i\mathbf{Q}\cdot\mathbf{r}_j}$, where j runs over the 128 spins in the supercell. $S(\mathbf{Q})$ is then averaged over all three spin ice domains. This calculation includes the magnetic form factor $f_j(\mathbf{Q})$ for Tb^{3+} and allows for direct comparison with experimental data.[31] In order to determine the deviation of the local structure from an ideal two-in, two-out scenario, we fit the calculated intensity to that at the nine $(\frac{1}{2},\frac{1}{2},\frac{1}{2})$-related positions observed in the experiment, letting the canting angles from

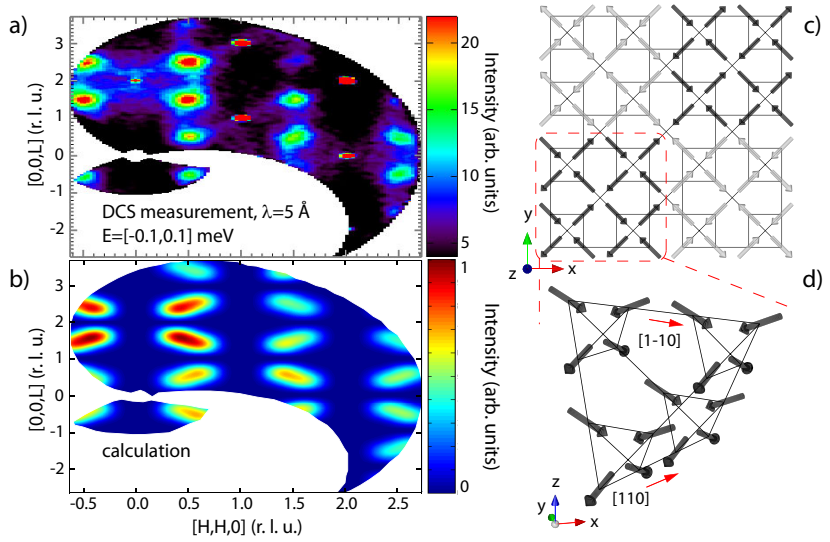

Figure 5.3: Comparison of the measured elastic diffuse scattering in the (H,H,L) plane of $Tb_2Ti_2O_7$ at 70 mK and $\mu_0 H = 0$ [panel (a)] to the calculated $S(\mathbf{Q})$ discussed in the text [panel (b)]. The intensity scale in the calculation is normalized to the largest intensity at $(\frac{1}{2},\frac{1}{2},\frac{3}{2})$. The spin arrangement between neighboring conventional unit cells is shown as a projection onto the xy plane in panel (c). The ordered two-in, two-out spin configuration in a single unit cell is shown in panel (d), and this pattern is reversed in the neighboring cells [black vs grey arrows in panel (c)] to form "$\langle \frac{1}{2}, \frac{1}{2}, \frac{1}{2} \rangle$ ordered spin ice". The spins are tilted from their local $\langle 111 \rangle$ axes by $\sim 12°$.

$\langle 111 \rangle$ vary. The best agreement with the experimental data [Fig. 5.3(a)] is shown in Fig. 5.3(b). The calculated magnetic structure factor reproduces the net intensities of the diffuse $(\frac{1}{2},\frac{1}{2},\frac{1}{2})$-like peaks very well. The elongation of the calculated diffuse scattering is a result of the finite size of the assumed spin arrangement (128 spins) for which we calculated the Fourier transform. The best-fit spin configuration has all spins canted by $\sim 12°$ from their local $\langle 111 \rangle$ axis with a reduction of the magnetic moment along the local z axis. Our fitting results are not very sensitive to the canting of the other two spin components. We show the resulting spin arrangement in Fig. 5.3(d) for one

conventional unit cell. $Tb_2Ti_2O_7$ at 70 mK is therefore composed of short-range ordered (SRO) domains of an AF $\left\langle \frac{1}{2}, \frac{1}{2}, \frac{1}{2} \right\rangle$ ordered spin ice.

The SRO AF spin ice state of $Tb_2Ti_2O_7$ at $\sim$ 70 mK and zero field shows $Tb_2Ti_2O_7$ to have a strong tendency to order. An actual LRO state may require lower temperatures and equilibrium conditions. Sensitivity to weak disorder, as is known to occur in single crystals of QSI $Yb_2Ti_2O_7$,[32] may also be relevant. We note that the spin canting angle from the local $\langle 111 \rangle$ axis is similar to the $\sim 13^\circ$ spin cant observed in the ferromagnetic "ordered spin ice" phase in $Tb_2Sn_2O_7$.[33,34] We further note a $\mathbf{q} = (\frac{1}{2}, \frac{1}{2}, \frac{1}{2})$ ordering wave vector is known to be selected by the combination of isotropic near neighbor exchange and dipolar interactions, as occurs in $Gd_2Ti_2O_7$.[35]

Figures 5.4 and 5.5 show the field and temperature dependence of the scattering near the $(-\frac{1}{2},\frac{1}{2},-\frac{1}{2})$ position as measured on LET with an incident neutron energy of 2.32 meV. A high magnetic field, low temperature data set at $T = 66$ mK and $\mu_0 H = 7$ T has been subtracted from all data sets in Figures 5.4 and 5.5. As is shown in these figures, even a small magnetic field removes the elastic diffuse scattering at $(\frac{1}{2},\frac{1}{2},\frac{1}{2})$ wave vectors, and a large magnetic field such as $\mu_0 H = 7$ T, pushes all inelastic magnetic scattering to higher energies, leaving our energy range of interest ($\leq$ 0.6 meV) empty. Consequently our $T = 66$ mK and $\mu_0 H = 7$ T data set serves as an excellent background for all the magnetic scattering of interest here.

Figure 5.4 shows elastic scattering, binned between -0.02 meV $< E <$ 0.02 meV for four different conditions of temperature and field, only one of which displays elastic Bragg-like scattering at $(\frac{1}{2},\frac{1}{2},\frac{1}{2})$. Figure 5.4(a) shows elastic

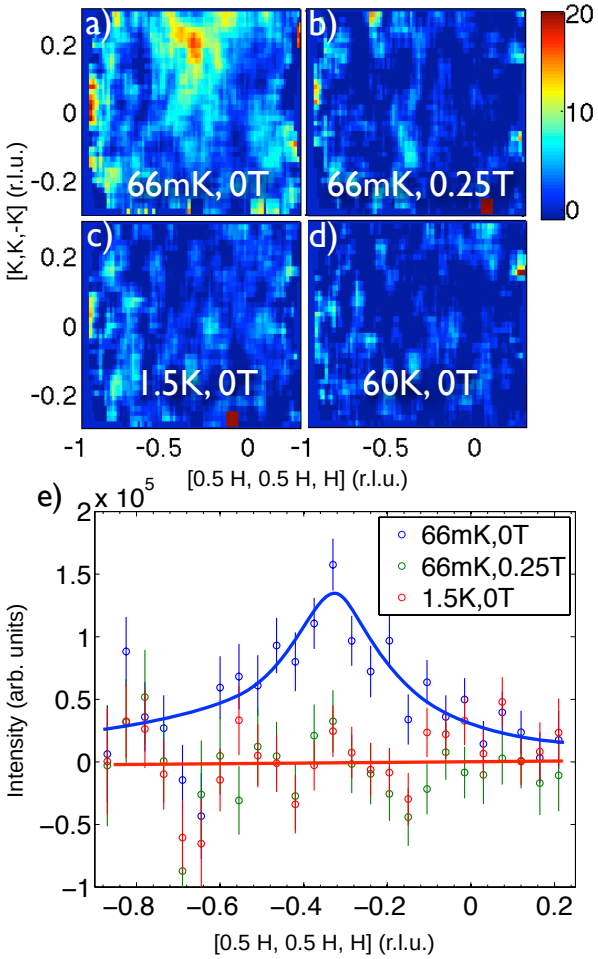

Figure 5.4: Elastic scattering data from LET, with the $T = 66$ mK, $\mu_0 H = 7$ T data set used as a background, shown in the [K,K,-K] vs [$\frac{1}{2}$H,$\frac{1}{2}$H,H] plane at μ_0H=0, integrated from E=[-0.02, 0.02] meV, and [H,-H,0] = [-0.6,-0.4] r.l.u.. In the scattering geometry used in the LET experiment, the [K,K,-K] direction is parallel to the vertical (field) direction. (a) The diffuse scattering at 66 mK, 0 T shown here corresponds to (-$\frac{1}{2}$,$\frac{1}{2}$,-$\frac{1}{2}$), which arises at [$\frac{1}{2}$H,$\frac{1}{2}$H,H] = -0.33 r.l.u., [H,-H,0] = -0.5 r.l.u., and [K,K,-K] = 0.166 r.l.u. This diffuse elastic scattering disappears upon either application of a $\mu_0 H = 0.25$ T field at $T = 66$ mK (b), or warming to 1.5 K (below Θ_{CW}) (c), or 60 K (above Θ_{CW}) (d). Panel (e) shows the field and temperature dependence of the diffuse elastic scattering at (-$\frac{1}{2}$,$\frac{1}{2}$,-$\frac{1}{2}$) as shown in panel (a), integrating over [$\frac{1}{2}$H,$\frac{1}{2}$H,H] = [0,0.3] r.l.u..

magnetic Bragg-like scattering at $(\frac{1}{2},\frac{1}{2},\frac{1}{2})$ at the lowest temperature, $T = 66$ mK and zero applied field. Figures 5.4(b), 5.4(c) and 5.4(d) show the same elastic scattering over the same range in $\mathbf{Q}$ space at (b) $T = 66$ mK and $\mu_0 H = 0.25$ T, (c) $T = 1.5$ K and $\mu_0 H = 0$ T, and (d) $T = 60$K and $\mu_0 H = 0$ T. The diffuse elastic scattering shown in Fig. 5.4(a) is of the same $(\frac{1}{2},\frac{1}{2},\frac{1}{2})$ type that was measured on DCS, although it occurs here within a different scattering plane than was shown in Figs. 5.1, 5.2, and 5.3. Figure 5.4(e) shows cuts through this $(-\frac{1}{2},\frac{1}{2},-\frac{1}{2})$ position for different fields and temperatures, again using a $T = 66$ mK and $\mu_0 H = 7$ T data set as a background. As seen in Fig. 5.4(e), the $(-\frac{1}{2},\frac{1}{2},-\frac{1}{2})$ elastic scattering can be completely removed at low temperatures by an applied field of 0.25 T along [11-1], confirming that it is magnetic and of the same origin as the elastic scattering shown in Figs. 5.1, 5.2, and 5.3. The elastic scattering also vanishes by $T = 1.5$ K, indicating that it is likely related to the broad hump in specific heat observed at 0.4 K in many samples.[18,36–39] We note that earlier neutron measurements using DCS on this same single crystal sample did not observe this $(\frac{1}{2},\frac{1}{2},\frac{1}{2})$ Bragg-like magnetic scattering at $T = 0.4$ K and $\mu_0 H = 0$ T.[25]

Figure 5.5 shows energy vs. wave vector slices of these same $S(\mathbf{Q}, E)$ data under the same conditions as were relevant for the elastic scattering maps in Fig. 5.4. Figure 5.5(a) shows data at $T = 66$ mK and $\mu_0 H = 0$ T, Fig. 5.5(b) shows $T = 66$ mK and $\mu_0 H = 0.25$ T, Fig. 5.5(c) shows $T = 1.5$ K and $\mu_0 H = 0$ T, and Fig. 5.5(d) shows $T = 60$ K and $\mu_0 H = 0$ T. As with the elastic data shown in Fig. 5.4, this inelastic data has employed a background data set at $T = 66$ mK and $\mu_0 H = 7$ T. The data set at $T = 66$ mK and zero field in Fig. 5.5(a) shows elastic scattering characteristic of the

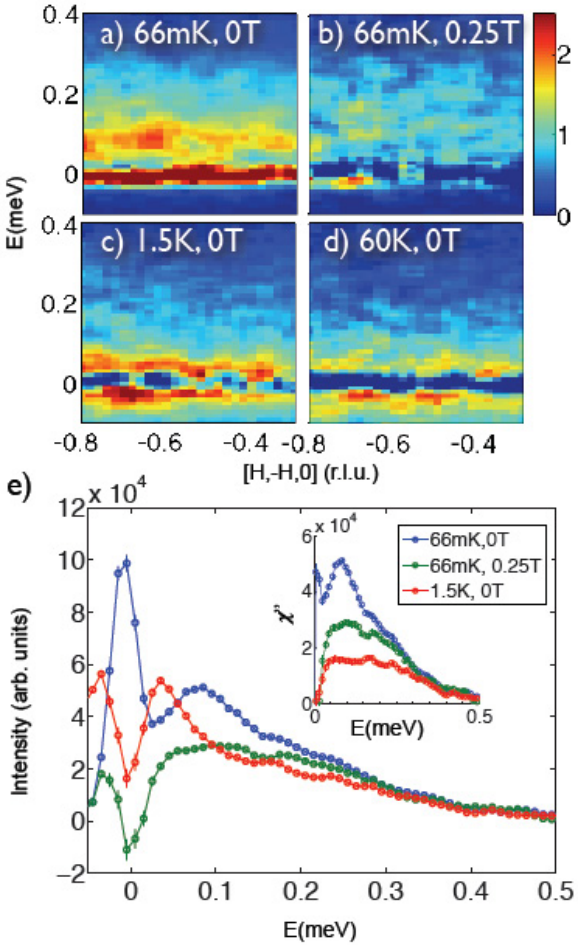

Figure 5.5: High-energy resolution data from LET, with the 66 mK, 7 T data set used as a background. Inelastic scattering integrated over $[\frac{1}{2}\mathrm{H},\frac{1}{2}\mathrm{H},\mathrm{H}]$ = [-1.5,1.0] r.l.u. and [K,K,-K] = [-0.5, 0.5] r.l.u. is shown for (a) $T = 66$ mK and $\mu_0 H = 0$, (b) $T = 66$ mK and $\mu_0 H = 0.25$ T, (c) $T = 1.5$ K and $\mu_0 H = 0$, and (d) $T = 60$ K and $\mu_0 H = 0$. A spin gap of $\sim 0.06 - 0.08$ meV opens up below 1.5 K, which was not resolved previously. The spin gap correlates strongly with the appearance of the $(\frac{1}{2},\frac{1}{2},\frac{1}{2})$ elastic magnetic peaks shown in Figs. 5.1-5.4. (e) Field and temperature dependence of the low energy inelastic scattering as shown in panels (a)-(c), integrated over the full [H,-H,0] range. The inset to Fig. 5.5(e) shows the same data corrected for the Bose factor, that is, $\chi''(\mathbf{Q}, E)$ [see Eq. 5.1].

diffuse antiferromagnetic spin ice short-range order. This elastic scattering is separated from a gapped continuum of inelastic scattering which extends from ~ 0.06 meV out to ~ 0.4 meV. Some magnetic inelastic spectral weight appears to exist within the gap, but this spectral weight is clearly strongly suppressed compared with that near the peak in the inelastic spectrum near ~ 0.08 meV. Application of a small field of 0.25 T at 66 mK, as is shown in Fig. 5.5(b) completely suppresses the elastic magnetic scattering at $(\frac{1}{2},\frac{1}{2},\frac{1}{2})$, as was shown in the elastic map in Fig. 5.4(b), but the low-energy inelastic magnetic scattering below 0.2 meV is also strongly suppressed. Data at higher temperatures and zero field is shown in Fig. 5.5(c) $T = 1.5$ K and Fig. 5.5(d) $T = 60$ K. The inelastic scattering at 1.5 K is taken at sufficiently low temperature (below $|\Theta_{\rm CW}| = |-19$ K$|$) to still be within the cooperatve paramagnetic regime. This 1.5 K data set shows the absence of $(\frac{1}{2},\frac{1}{2},\frac{1}{2})$ elastic magnetic scattering and an ungapped quasielastic magnetic spectrum. The data set at $T = 60$ K and zero field in Fig. 5.5(d) is taken well into the fully paramagnetic phase. Its inelastic spectrum is also ungapped and quasielastic, and the overall bandwidth of the magnetic inelastic spectrum has softened by a factor of ~ 1.5 relative to that shown in Fig. 5.5(a) for $T = 66$ mK and zero field.

The similarities and differences between the inelastic magnetic spectrum in the presence and absence of the $(\frac{1}{2},\frac{1}{2},\frac{1}{2})$ Bragg-like scattering can be appreciated by taking energy cuts through the data shown in Figs. 5.5(a) through 5.5(d). This is what is shown in Fig. 5.5(e) for $T = 66$ mK and $\mu_0 H = 0$ T, for $T = 66$mK and $\mu_0 H = 0.25$ T, and for $T = 1.5$ K and $\mu_0 H = 0$ T. One clearly sees that resolution-limited elastic magnetic scattering is only present

for $T = 66$ mK and zero field. The inelastic magnetic spectrum at this base temperature and zero field clearly peaks near 0.08 meV and is strongly suppressed at lower energies. The contrast between this gapped inelastic spectrum at 66 mK and zero field and the quasielastic scattering at higher temperature at $T = 1.5$ K, but still low compared with $\Theta_{\rm CW}$ is clear from Fig. 5.5(e). The inset to Fig. 5.5(e) shows the dynamic susceptibility, $\chi''(\mathbf{Q}, E)$, which is related to $S(\mathbf{Q}, E)$ through the Bose factor:

$$S(\mathbf{Q}, E) = \frac{\chi''(\mathbf{Q}, E)}{1 - e^{-E/k_B T}}. \tag{5.1}$$

We estimate the spin gap energy at $\sim$ 0.06-0.08 meV. The appearance of the gapped structure in the low energy magnetic excitation spectrum of $Tb_2Ti_2O_7$ is clearly tightly correlated with the appearance of strong $(\frac{1}{2},\frac{1}{2},\frac{1}{2})$ elastic magnetic Bragg scattering, which arises due to the formation of a SRO AF spin ice structure, as shown in Fig. 5.3(c) and (d).

The clear presence of the $\sim 0.06 - 0.08$ meV gap separating the low energy inelastic scattering (0.06-0.6 meV) from the elastic scattering due to the SRO AF spin ice scattering at $(\frac{1}{2},\frac{1}{2},\frac{1}{2})$ wave vectors, confirms that three distinct regimes of magnetic scattering exist at low temperatures: elastic, low-energy inelastic, and "high"-energy inelastic scattering due to the excited CF doublet at energies of ~ 1 meV [see Fig. 5.1(d)]. True static long-range order in zero field would be inconsistent with the nonmagnetic, singlet ground state scenario previously suggested.[22]

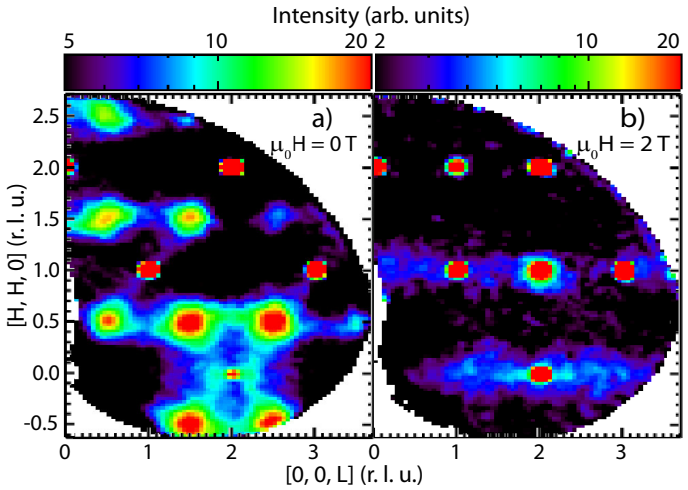

Figure 5.6: Pinch-point like scattering in the ground state of $Tb_2Ti_2O_7$ observed on DCS at ~ 70 mK for $\mu_0 H = 0$ T in panel (a). Panel (b) shows diffuse scattering along the $\langle 0, 0, L\rangle$ direction under application of a $\mu_0 H = 2$ T field, which might originate from anisotropic exchange. Both data sets show elastic scattering for -0.1 meV $< E <$ 0.1 meV and are displayed on a logarithmic intensity scale (compared to a linear scale in Fig. 5.1).

Pinch-point diffuse scattering characteristic of Coulombic spin ice correlations [40–42] has been of great interest in the classical spin ice materials $Dy_2Ti_2O_7$ and $Ho_2Ti_2O_7$ and recently in $Tb_2Ti_2O_7$.[43] Figure 5.6 shows these correlations, most notably around (0,0,2), as they appear in the elastic scattering at $T = 0.07$ K and (a) zero field, and with a (b) 2 T magnetic field applied along [1-10].

Our pinch point diffuse scattering near (0,0,2) is qualitatively similar to that observed in Fig. 5.2(a) of Fennell *et al.*[43] As shown in Fig. 5.6, we observe "rods" of scattering along the $\langle 00L\rangle$ and $\langle HHH\rangle$ directions, which appear to be modulated by pinch points near the zone centers at (1,1,1), (1,1,3) and near (0,0,2). In a 2 T field applied along [1-10], all elastic scattering at $(\frac{1}{2},\frac{1}{2},\frac{1}{2})$ positions has disappeared and only broad diffuse scattering along the $\langle 0, 0, L\rangle$

direction remains. The origin of this rod-like elastic diffuse scattering is not understood, but one can speculate that it originates from anisotropic exchange in $Tb_2Ti_2O_7$, as is known to describe the microscopic spin Hamiltonian in $Yb_2Ti_2O_7$ [12] and $Er_2Ti_2O_7$.[3]

5.1.4 Conclusion

The ground state of $Tb_2Ti_2O_7$ has by now been studied for more than a decade by neutron scattering techniques. It is surprising that the $(\frac{1}{2},\frac{1}{2},\frac{1}{2})$ elastic SRO scattering, presaging a transition to LRO, has not previously been observed. This is likely due to the low onset temperature of this scattering: for example Rule *et al.* [25] previously studied the same single crystal with the same instrumental conditions at DCS, but at temperatures of 400 mK and above, without seeing this scattering. In fact, triple-axis measurements by Yasui *et al.*[44] do show evidence for a peak at $(\frac{1}{2},\frac{1}{2},\frac{5}{2})$ at $T = 0.4$ K [Fig. 2 in Ref. 44], however this feature was not pursued further in subsequent studies. Diffraction experiments, such as that by Gardner *et al.*, [24] would be problematic due to integration over elastic and low energy inelastic scattering, which we show in Fig. 5.1 to have very different **Q** dependencies.

In conclusion, new neutron scattering measurements on $Tb_2Ti_2O_7$ at $T = 0.07$ K in zero field have revealed elastic diffuse scattering at $(\frac{1}{2},\frac{1}{2},\frac{1}{2})$ positions characteristic of short-range AF spin ice correlations extending over roughly two conventional pyrochlore unit cells. This elastic scattering is separated by a gap of $\sim 0.06 - 0.08$ meV from low lying inelastic scattering, and can be quantitatively described based on an ordered two-in, two-out local spin ice

structure with a spin canting angle of $\sim 12^{\circ}$. This development of AF spin ice correlations in $Tb_2Ti_2O_7$ is characteristic of a strong tendency to form the corresponding LRO state which does not occur either because the temperature is not sufficiently low, or due to weak disorder in the samples, as has been recently characterized in other exotic pyrochlore magnets,[32] or both.

Following completion of this work, we became aware of two preprints reporting related neutron work on single-crystal [45] and polycrystalline [46] $Tb_2Ti_2O_7$ samples.

The authors acknowledge useful contributions from M. J. P. Gingras. This work utilized facilities supported in part by the National Science Foundation under Agreement No. DMR-0944772, and was supported by NSERC of Canada. The DAVE software package[47] was used for data reduction and analysis of DCS data. LET data were reduced using Mantid[48] and analysed using the HORACE software package.[49]

5.2 Temperature and Magnetic Field Dependence of Spin Ice Correlations in the Pyrochlore Magnet $Tb_2Ti_2O_7$

K. Fritsch,[1] E. Kermarrec,[1] K. A. Ross,[1,2,3] Y. Qiu,[3,4] J. R. D. Copley,[3] D. Pomaranski,[5] J. B. Kycia,[5] H. A. Dabkowska,[6] and B. D. Gaulin[1,6,7]

[1]*Department of Physics and Astronomy, McMaster University, Hamilton, Ontario, L8S 4M1, Canada*

[2]*Institute for Quantum Matter and Department of Physics and Astronomy, Johns Hopkins University, Baltimore, Maryland 21218, USA*

[3]*NIST Center for Neutron Research, NIST, Gaithersburg, Maryland 20899-8102, USA*

[4]*Department of Materials Science and Engineering, University of Maryland, College Park, Maryland 20742, USA*

[5]*Department of Physics and Astronomy and Guelph-Waterloo Physics Institute, University of Waterloo, Waterloo, Ontario, Canada N2L 3G1*

[6]*Brockhouse Institute for Materials Research, Hamilton, Ontario, L8S 4M1, Canada*

[7]*Canadian Institute for Advanced Research, 180 Dundas St. W., Toronto, Ontario, M5G 1Z8, Canada*

Abstract

We present a parametric study of the diffuse magnetic scattering at $\left(\frac{1}{2},\frac{1}{2},\frac{1}{2}\right)$ positions in reciprocal space, ascribed to a frozen antiferromagnetic spin ice state in single crystalline $Tb_2Ti_2O_7$. Our high-resolution neutron scattering measurements show that the elastic (-0.02 meV $< E <$ 0.02 meV) $\left(\frac{1}{2},\frac{1}{2},\frac{1}{2}\right)$ scattering develops strongly below $\sim$ 275 mK, and correlates with the opening of a spin gap of $\sim 0.06 - 0.08$ meV over most of the Brillouin zone. The

concomitant low-lying magnetic spin excitations are weakly dispersive and appear to go soft at the $\left(\frac{1}{2}, \frac{1}{2}, \frac{1}{2}\right)$ wave vector at 80 mK. The nature of the transition at 275 mK has many characteristics of spin glass behavior, consistent with ac-susceptibility measurements. The application of a small magnetic field of 0.075 T applied along the [1-10] direction destroys the $\left(\frac{1}{2}, \frac{1}{2}, \frac{1}{2}\right)$ elastic scattering, revealing the fragility of this short-range ordered ground state. We construct a new H-T phase diagram for $Tb_2Ti_2O_7$ and [1-10] fields which incorporates this frozen spin ice regime and the antiferromagnetic long-range order previously known to be induced in relatively large fields. Specific heat measurements on the same crystal reveal a sharp anomaly at $T_c \sim 450$ mK and no indication of a transition near ~ 275 mK. We conclude that the higher temperature specific heat peak is not related to the magnetic ordering but involves different degrees of freedom.

5.2.1 Introduction

The search for experimental realizations of quantum spin liquid (QSL) and quantum spin ice (QSI) states is of great current interest [9,15] due to the potential for exotic physics within these systems. Geometrically frustrated magnetic materials are central to the discovery of such exotic states.[1] Besides materials based on quasi two-dimensional (2D) lattices such as herbertsmithite[50,51] or the organic spin liquid candidate κ-(BEDT-TTF)$_2$Cu$_2$(CN)$_3$,[52,53] the three-dimensional (3D) pyrochlore lattice consisting of networks of corner-sharing tetrahedra, has been the focus of significant and sustained research efforts.[2,5,8–10] The family of rare earth-based titanate pyrochlores has played a prominent

role in these studies as many members of this family can be grown as large and pristine single crystals.[3,12,40,42] Within this family, $Tb_2Ti_2O_7$ stands out as perhaps the least well understood, despite having been studied in this context for well over a decade. In this material, the Tb^{3+} magnetic moments that decorate the pyrochlore lattice are expected to display Ising-like easy axis anisotropy with spins pointing along the local $\langle 111 \rangle$ axes, either into or out of the tetrahedra, as a consequence of their crystal field (CF) doublet ground state.[18,26] Based on a negative Curie-Weiss temperature ($\Theta_{CW} \sim$ -14 K) and this Ising-like anisotropy, mean-field theory shows the classical ground state of $Tb_2Ti_2O_7$ to not be frustrated, and $Tb_2Ti_2O_7$ is expected to order into an antiferromagnetic (AF) $\mathbf{Q} = 0$ Néel ordered state around $\sim$ 1 K.[18] Yet, this material fails to exhibit conventional long-range order (LRO) down to at least 50 mK as shown by very early studies by Gardner *et al.*[16,17]

This puzzle has motivated two vigorously debated[20,21,23,54] theoretical scenarios to account for $Tb_2Ti_2O_7$'s disordered ground state: a quantum spin ice (QSI) scenario[20,21] and a nonmagnetic singlet ground state.[22] The QSI proposal introduces quantum dynamics to the problem through virtual fluctuations of the Tb^{3+} ions between their ground state and excited CF doublets. These quantum fluctuations reposition $Tb_2Ti_2O_7$ into the nearby spin ice regime within a generalized phase diagram appropriate to Ising-like pyrochlore magnets. The nonmagnetic singlet scenario assumes a splitting of the accidental CF doublet ground state of the Tb^{3+} ions ($J = 6$, non-Kramers) into two non-magnetic singlets through a Jahn-Teller-like symmetry lowering of the CF environment, thus producing a non-magnetic ground state. The latter scenario implies a non-cubic structure at low but finite temperatures

in $Tb_2Ti_2O_7$, and to date, evidence for this is lacking at all but very large magnetic fields.[55,56]

Recent experiments on $Tb_2Ti_2O_7$ have shown signatures of the proposed QSI state, most notably pinch point scattering[43] indicative of Coulombic correlations in spin ice, and signs of a magnetization plateau for magnetic fields along [111], although there is a diversity in the interpretation of this latter evidence.[57–61] Our recent neutron scattering measurements [62] on single-crystalline $Tb_2Ti_2O_7$ at 70 mK have revealed short-range spin ice correlations at $\left(\frac{1}{2}, \frac{1}{2}, \frac{1}{2}\right)$ wave vectors which can be ascribed to a short-range antiferromagnetically ordered spin ice state with spin canting at an angle of $\sim 12^\circ$ from the local $\langle 111 \rangle$ axes. These static correlations observed in the elastic scattering channel were shown to be very sensitive to both applied magnetic field and temperature, although parametric studies of the field and temperature dependence of this scattering were not performed. These static $\left(\frac{1}{2}, \frac{1}{2}, \frac{1}{2}\right)$ correlations were separated from low-lying inelastic magnetic excitations by a spin gap of $\sim$0.06-0.08 meV. A subsequent study of non-stoichiometric $Tb_{2+x}Ti_{2-x}O_{7+y}$ by Taniguchi *et al.* [46] also observed the appearance of a $\left(\frac{1}{2}, \frac{1}{2}, \frac{1}{2}\right)$ Bragg-like peak associated with quasi-long-range order at low temperatures in a polycrystalline sample which was lightly "stuffed", $Tb_{2+x}Ti_{2-x}O_{7+y}$ ($x = 0.005$).

In this paper, we report a detailed study of the temperature and field dependence of the previously observed elastic $\left(\frac{1}{2}, \frac{1}{2}, \frac{1}{2}\right)$ and associated low-lying inelastic scattering in $Tb_2Ti_2O_7$. We show that the elastic scattering appears upon lowering the temperature below $\sim$ 275 mK and that its appearance correlates with the opening of a spin gap within the low-lying magnetic spectral

weight over most of the Brillouin zone. This magnetic spectral weight and its associated spin excitations exhibit weak dispersion and appear to soften at the "quasi"-ordering wave vector $\left(\frac{1}{2}, \frac{1}{2}, \frac{1}{2}\right)$ and at the lowest temperature measured, $T = 80$ mK. The application of a magnetic field along [1-10] leads to a destruction of the short-range ordered ground state by $\mu_0 H = 0.075$ T. We construct a new $H - T$ phase diagram for $Tb_2Ti_2O_7$ in a [1-10] magnetic field, which encompasses both this new frozen spin ice state at very low fields and temperature, and the previously known long-range antiferromagnetic state which exists at relatively high fields and over a much larger range of temperatures.

5.2.2 Experimental Details

The single crystal sample of $Tb_2Ti_2O_7$ used for the neutron scattering measurements we present here is the same sample used in earlier studies[25,62] and was grown using the optical floating zone technique at McMaster University.[27,28] Time-of-flight neutron scattering measurements were performed using the disk-chopper spectrometer DCS [29] at the NIST Center for Neutron Research. Two different incident energies were employed; for lower energy-resolution measurements we used E_i=3.27 meV, giving an energy resolution of 0.1 meV, while the higher energy-resolution measurements we report used E_i=1.28 meV with a resulting resolution of 0.02 meV. The sample was carefully aligned with the [1-10] direction vertical to within 0.5°, such that the (H,H,L) plane was coincident with the horizontal scattering plane. Measure-

ments were performed in a temperature range of $\sim$ 80 mK $< T \lesssim$ 650 mK and at magnetic fields $\leq$ 0.2 T.

Specific heat measurements were performed with a ^{3}He/^{4}He dilution refrigerator at the University of Waterloo. The crystal used for neutron scattering measurements was sectioned into a 33.8 mg mass with dimension 2.6 x 2.6 x 1.3 mm^3. The relaxation method was employed with a thermal weak link of manganin wire, with conductance 5.0 x 10^{-7} J/K/s at 0.80 K. The resulting time constant was greater than 600 seconds at the highest temperature measured. The average step size for the relaxation measurement was 3.5% of the nominal temperature, with a minimum equilibration time window of five times the thermal relaxation constant.

5.2.3 Magnetic Field dependence

Figure 5.7 shows a series of elastic scattering maps in the (H,H,L) plane for different magnetic fields applied along [1-10] in panels (a) through (e). Here, elastic scattering integrates over -0.1 meV $< E <$ 0.1 meV in energy. Figure 5.7(f) shows a cut of this elastic scattering, along the [111] high-symmetry direction covering the $(-0.5, -0.5, 1.5)$, $(0.5, 0.5, 2.5)$ as well as the $(0, 0, 2)$ and $(1, 1, 3)$ Bragg positions, as indicated by the yellow dashed line in Fig. 5.7(e). As the applied magnetic field is increased to 0.05 T, the previously observed strong diffuse scattering at the $\left(\frac{1}{2}, \frac{1}{2}, \frac{1}{2}\right)$ positions in zero field (panel (a)) gets suppressed substantially (panel (b)) and is much reduced by 0.075 T (panel (c)).

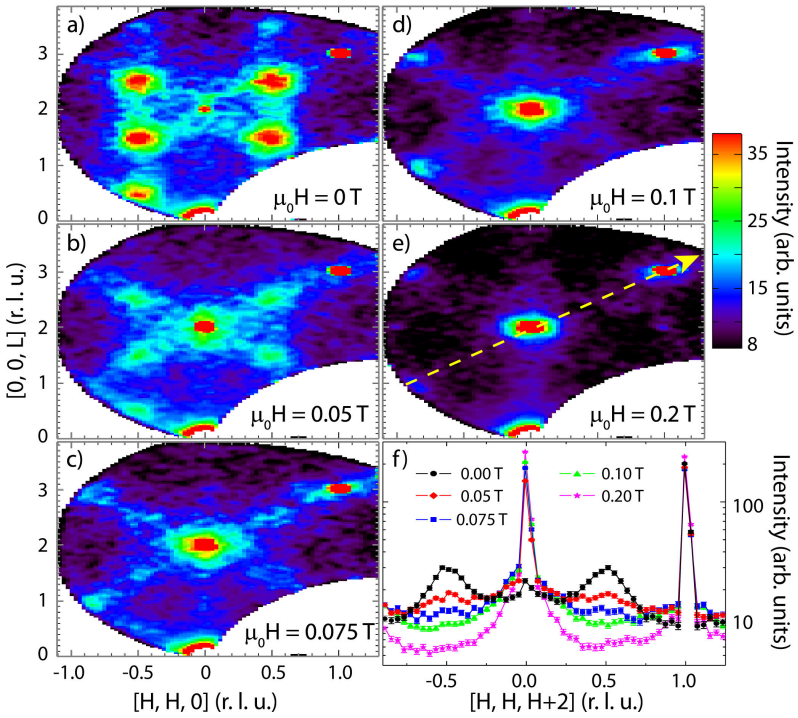

Figure 5.7: Elastic neutron scattering data within the (H,H,L) plane of $Tb_2Ti_2O_7$ at $T = 80$ mK for different values of applied magnetic field ($H \parallel$ [1-10]). The energy is integrated from -0.1 meV $< E <$ 0.1 meV. Panels (a) through (e) show the evolution of the elastic scattering for an applied magnetic field of 0, 0.05, 0.075, 0.1 and 0.2 T, respectively. Panel (f) shows the **Q**-dependence of the elastic scattering along the [111] direction cutting through the $(0, 0, 2)$ Bragg position as indicated by the yellow arrow in panel (e). The $\left(\frac{1}{2}, \frac{1}{2}, \frac{1}{2}\right)$ peaks vanish around $\mu_0 H \sim 0.075$ T. All data have an empty can background subtracted. The error bars are $\pm 1\sigma$.

Simultaneous to the suppression of the $\left(\frac{1}{2}, \frac{1}{2}, \frac{1}{2}\right)$ diffuse scattering intensity in fields up to 0.075 T, we observe a strong build-up in magnetic elastic intensity at the structurally forbidden $(0, 0, 2)$ peak and a weak decrease in the structurally allowed $(1, 1, 3)$ Bragg peak. As the field is increased further (panels (d) and (e)), most of the remaining diffuse scattering condenses into the Bragg positions at $(0, 0, 2)$ and $(1, 1, 3)$. The intensity scale is linear for Fig. 5.7(a)-(e). In contrast, the cut along the [111] direction through $(0, 0, 2)$

in Fig. 5.7(f) is plotted on a logarithmic intensity scale. Note that the highest applied field here, 0.2 T, is still far below the critical [1-10] field ~ 2 T, above which $Tb_2Ti_2O_7$ is found in a field-induced antiferromagnetic long-range ordered state, characterized by the appearance of resolution-limited spin waves and a strong $(1, 1, 2)$ magnetic Bragg peak.[25]

A further feature in the elastic scattering maps are weak rods of scattering along both the $\langle 00L \rangle$ and $\langle 111 \rangle$ directions that can be identified as evidence for significant anisotropic exchange in $Tb_2Ti_2O_7$.[43] Rods of magnetic scattering have been identified in other rare-earth titanate pyrochlores, such as $Yb_2Ti_2O_7$,[63] where anisotropic exchange is well established.[12,13,64] Anisotropic exchange in $Tb_2Ti_2O_7$ has recently been investigated in papers by Bonville *et al.*[54] and Curnoe,[65] the latter of which related an effective $S = 1/2$ spin Hamiltonian to diffuse magnetic neutron scattering.

One can integrate up the elastic scattering data in a relatively small region around the $\left(\frac{1}{2}, \frac{1}{2}, \frac{1}{2}\right)$ or $(0, 0, 2)$ positions in reciprocal space, and look at its explicit [1-10] magnetic field dependence. This is what is shown in Fig. 5.8, with relatively small integration ranges of ± 0.2 r.l.u. in [H,H,H], and ± 0.15 r.l.u. perpendicular to [H,H,H] for $\left(\frac{1}{2}, \frac{1}{2}, \frac{1}{2}\right)$, and ± 0.1 r.l.u. in [H,H,H] and ± 0.15 r.l.u. perpendicular to [H,H,H] for $(0, 0, 2)$. We identify the inflection point in the field dependence of $\left(\frac{1}{2}, \frac{1}{2}, \frac{1}{2}\right)$ near $\mu_0 H \sim 0.075$ T, as well as the leveling off of the $(0, 0, 2)$ elastic intensity for fields beyond 0.075 T with the $T \sim 0$ phase boundary to the frozen, antiferromagnetic spin ice state in $Tb_2Ti_2O_7$.

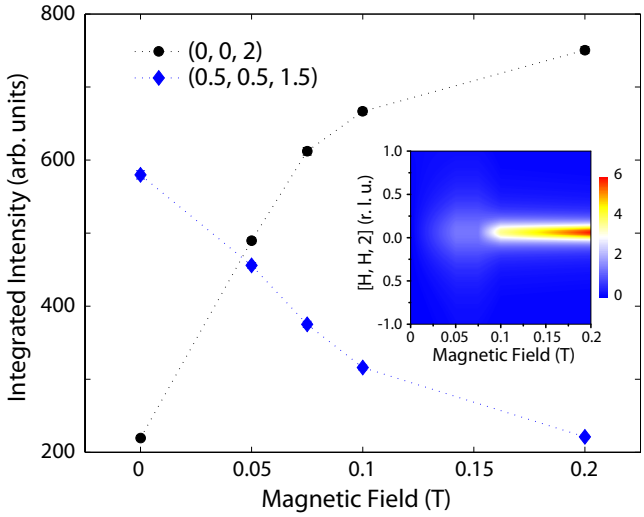

Figure 5.8: Integrated elastic scattering at the $\left(\frac{1}{2}, \frac{1}{2}, \frac{1}{2}\right)$ and $(0, 0, 2)$ positions as a function of magnetic field. The $\left(\frac{1}{2}, \frac{1}{2}, \frac{1}{2}\right)$ scattering gets clearly suppressed at $\sim$ 0.075 T. The inset shows a color contour map of the diffuse elastic scattering around the $(0, 0, 2)$ Bragg peak made of line scans along [H,H,2]. The binning ranges for this cut were $L = [1.9, 2.1]$ r.l.u.. The intensity of the resolution-limited elastic scattering at (0,0,2) has been subtracted. An empty can background subtraction and correction for detector efficiency were performed. Error bars are $\pm 1\sigma$.

The field dependence of the elastic magnetic scattering, and in particular the rapid fall-off of the $\left(\frac{1}{2}, \frac{1}{2}, \frac{1}{2}\right)$ frozen spin ice elastic scattering near 0.075 T is in qualitative agreement with recent work by Yin *et al.*.[60] They have proposed a low-temperature low-field phase diagram for $Tb_2Ti_2O_7$ based on magnetization and ac-susceptibility data. These measurements reveal two magnetic phases, the first one of which appears below 140 mK and for fields $\mu_0 H < 0.067$ T, while another phase is found at very low temperatures $T < 40$ mK and higher fields $0.067 < \mu_0 H < 0.6$ T. From the observation of a weak magnetization plateau in the presence of a [111] magnetic field, these authors conclude that a kagome spin ice state exists at higher fields, with a QSI state

at low and zero magnetic fields. Although these Yin *et al.*[60] measurements were performed in a [111] applied magnetic field, we note that anisotropy in the magnetization of $Tb_2Ti_2O_7$ is only observed for field strengths exceeding $\gtrsim 0.3$ T, well above the range of applied field strengths which we report here in our neutron scattering measurements. For that reason, we consider the phase diagram presented in Ref. 60 to be germane to our findings, reinforcing our assertion that the $\left(\frac{1}{2}, \frac{1}{2}, \frac{1}{2}\right)$ elastic scattering is associated with a QSI state.

5.2.4 Temperature Dependence

The temperature dependence of the integrated elastic intensity of the $\left(\frac{1}{2}, \frac{1}{2}, \frac{1}{2}\right)$ peaks in zero field is presented in Fig. 5.9. We determined the elastic integrated intensity (-0.1 meV <E< 0.1 meV) at the four $\left(\frac{1}{2}, \frac{1}{2}, \frac{1}{2}\right)$ positions in our field of view in Fig. 5.9(a) and average the integrated intensities at each temperature. The corresponding background signal for each T was obtained by integrating over a region of low intensity in reciprocal space around $(1, 1, 2)$. This background term was subsequently subtracted from the averaged $\left(\frac{1}{2}, \frac{1}{2}, \frac{1}{2}\right)$ integrated elastic intensity.

The results of these calculations are shown in Fig. 5.9(b) for individual heating and cooling runs labeled in the order of the measurements. Two prominent features become apparent from that Fig. 5.9. First, the temperature dependence of the $\left(\frac{1}{2}, \frac{1}{2}, \frac{1}{2}\right)$ peaks behaves in an order parameter-like fashion with a distinctive drop in integrated intensity around 275 mK. Second, the ground state below 275 mK has some history dependence to it, with the elastic $\left(\frac{1}{2}, \frac{1}{2}, \frac{1}{2}\right)$ peak intensity variable from one thermal history to the next.

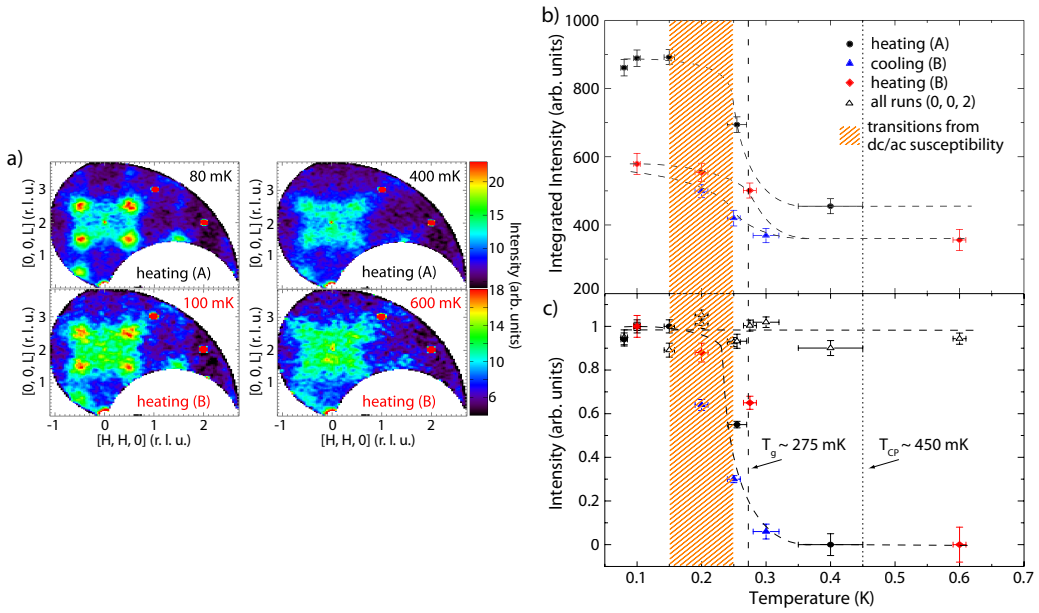

Figure 5.9: Temperature dependence of the elastic $\left(\frac{1}{2}, \frac{1}{2}, \frac{1}{2}\right)$ scattering in zero field. The integrated elastic scattering intensity (-0.1 meV $< E <$ 0.1 meV, H$= \pm [0.4, 0.6]$ r.l.u., L$= [1.4, 1.6]$ and L$= [2.4, 2.6]$ r.l.u.) at the four $\left(\frac{1}{2}, \frac{1}{2}, \frac{1}{2}\right)$-like positions is presented as a function of temperature for different heating and cooling cycles in panel (b). Please see text for details. Representative reciprocal space maps for the two heating cycles are shown in panel (a). Panel (c) shows the integrated intensity from (b) scaled to the difference between the low-temperature phase at 100 mK and the high-temperature phase at 600 mK (heating B) or 400 mK (heating A), placing the transition below which $\left(\frac{1}{2}, \frac{1}{2}, \frac{1}{2}\right)$ peaks appear at a temperature of ~ 275 mK. In addition, the temperature dependence of the elastic $(0, 0, 2)$ scattering, normalized to the intensity at the lowest temperatures, is shown on the same plot, indicating no obvious temperature dependence. Various reports of this glassy transition from ac-susceptibility measurements[17,36,57,66] are encompassed by the hatched area. The specific heat anomaly found for our crystal at $T_{\mathrm{Cp}} \sim 450$ mK is indicated by a dotted vertical line. This anomaly appears at considerably higher temperature than the onset of the short-range magnetic ordering. Dashed lines serve as guide to the eyes.

History dependence is a common feature of spin glass states. [67,68] We first discuss the second observation. Data points were collected in three temperature sweeps; heating A, cooling B and heating B. Representative elastic reciprocal space maps for the two runs obtained during heating are shown in Fig. 5.9(a) for the low temperature short-range ordered ground state (80 mK or 100 mK) and for the higher temperature disordered state (400 mK or 600 mK, respectively). We observe that the absolute intensity of the $(\frac{1}{2},\frac{1}{2},\frac{1}{2})$ elastic peaks in the second heating run is a factor of $\sim$2 smaller, and that the overall diffuse elastic scattering background is somewhat larger compared to the first heating run. This indicates that a complex freezing process with several metastable states is likely at play at low temperatures. This is not so surprising, as the $(\frac{1}{2},\frac{1}{2},\frac{1}{2})$ elastic scattering does not correspond to long-range order, but rather is known to be characterized by a relatively short and isotropic correlation length of $\sim$ 8 Å, again typical of spin glasses. Despite this, a common feature in all three heating and cooling runs is the appearance of the $(\frac{1}{2},\frac{1}{2},\frac{1}{2})$ peaks below 275 mK. To make that point, we scaled and normalized the integrated elastic intensities at $(\frac{1}{2},\frac{1}{2},\frac{1}{2})$ from Fig. 5.9(b) to the difference in intensity between the low-temperature state at 100 mK or below and that of the high-temperature state (400 mK or 600 mK, respectively). The result is shown in Fig. 5.9(c), which shows a glass-like transition to occur around $\sim$275 mK, independent of the detailed history dependence. We also note here that, in contrast to the elastic scattering at $(\frac{1}{2},\frac{1}{2},\frac{1}{2})$, the elastic scattering at (0,0,2) does not show any significant temperature dependence as shown in Figure 5.9(c).

The spin glass transition as measured with the $(\frac{1}{2},\frac{1}{2},\frac{1}{2})$ elastic magnetic scattering is consistent with that observed by several groups using ac-susceptibility

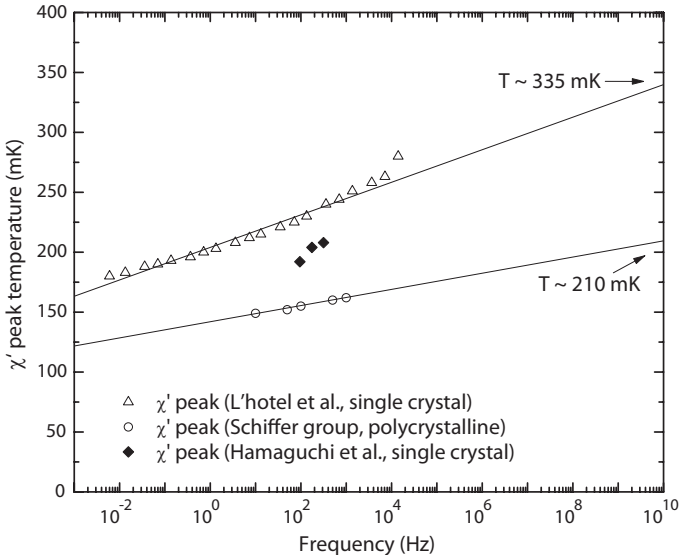

Figure 5.10: Shift of the ac-susceptibility peaks per decade frequency for polycrystal and single crystalline samples from different groups.[36,57,69] For these three measurements, the slope $\frac{\Delta T}{T\Delta(\log_{10} f)}$ <0.1, typical of what is expected for spin glasses.[67] The extrapolation of the ac-susceptibility peak to frequencies of the order 0.01 THz$\sim$ 0.04 meV energies, at which our measurements probe the system, shows that the expected transition occurs between 210-335 mK. The transition temperature we determine falls right within that range and is thus consistent with these measurements.

measurements. [17,36,57,69] This data is summarized in Fig. 5.10, and peaks found in the χ', the real part of the ac-susceptibility, lie in the temperature range from $\sim$150-250 mK. This temperature regime is indicated with an orange hatched area in Fig. 5.9(b) and (c), so that the results from elastic neutron scattering and ac-susceptibility can be compared. As neutron scattering measurements are performed at relatively high frequencies compared with ac-susceptibility, it is typical for neutron scattering to measure spin freezing associated with spin glass transitions at higher temperatures than are observed in ac-susceptibility. This is illustrated in Fig. 5.10, in which we show the linearly extrapolated peak-shift per decade frequency, a phenomenological

parameter used to describe the temperature dependence of the χ' peak in spin glasses as a function of frequency, to the frequency appropriate to our neutron measurements, ∼0.01 THz. This shows that the transition is expected to occur between 210-335 mK in our measurement, in good agreement with our observations. This frequency dependence may indeed play a role here, although as seen in Fig. 5.9(b) and (c), this does not seem to be a large effect as the agreement between the two techniques is quite good.

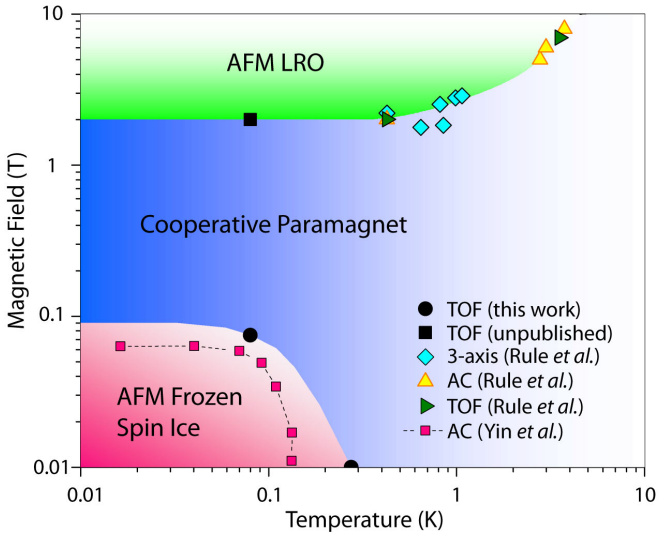

Figure 5.11: *H-T* phase diagram for $Tb_2Ti_2O_7$ in [1-10] field extracted from neutron scattering measurements in the low field and low temperature region presented in this work and from high field and higher temperature measurements by Rule *et al.*.[25] The magnetic phase transitions measured by Yin *et al.*[60] from ac-susceptibility with fields along [111] are also shown.

Based on the temperature and field dependence of the $\left(\frac{1}{2}, \frac{1}{2}, \frac{1}{2}\right)$ elastic scattering, we can construct an *H-T* phase diagram for $Tb_2Ti_2O_7$ in [1-10] field, shown in Figure 5.11, including the high-field and high-temperature regions determined by Rule *et al.*'s work.[25] Note that both temperature and field axes are on a logarithmic scale.

Higher energy resolution neutron scattering measurements with $E_i = 1.28$ meV were performed to investigate the temperature and **Q**-dependence of the low-lying spin excitations in $Tb_2Ti_2O_7$ in zero magnetic field. Figure 5.12(a) shows a plot of intensity vs energy transfer obtained by integrating over the two $(\frac{1}{2},\frac{1}{2},\frac{1}{2})$ positions in reciprocal space shown as the black squares in the inset to Fig. 5.12(a). Data is shown for three different temperatures, in the ground state ($T = 80$ mK), near the spin glass transition ($T = 275$ mK) and well above the transition ($T = 600$ mK). As the temperature is lowered through the transition at 275 mK, spectral weight is transferred from the low-energy inelastic channel into the resolution-limited elastic channel (-0.02 meV $< E <$0.02 meV), opening up a gap of $\sim 0.06 - 0.08$ meV. The low-lying spin excitation spectrum above the gap extends ∼0.2meV. This collapse of the magnetic spectral weight over much of the magnetic Brillouin zone into the elastic channel is a canonical signature of spin freezing behavior, as observed in spin glasses such as, for example, $Y_2Mo_2O_7$.[70]

μSR measurements[16,66] in zero field have consistently reported persistent dynamics in the spin lattice relaxation rate down to very low temperatures in $Tb_2Ti_2O_7$, which suggest that either the elastic scattering itself is not truly elastic on the lower frequency scale probed by μSR, or that the depletion of spectral weight in the spin gap is not complete.

Weak **Q**-dependence is observed to the inelastic magnetic spectral weight at low temperatures, as shown in Fig. 5.12(b). This plot compares intensity vs energy transfer over small regions of reciprocal space centered on **Q**=$\left(\frac{1}{2}, \frac{1}{2}, \frac{1}{2}\right)$ wave vectors, and positions in reciprocal space far-removed from $\left(\frac{1}{2}, \frac{1}{2}, \frac{1}{2}\right)$ posi-

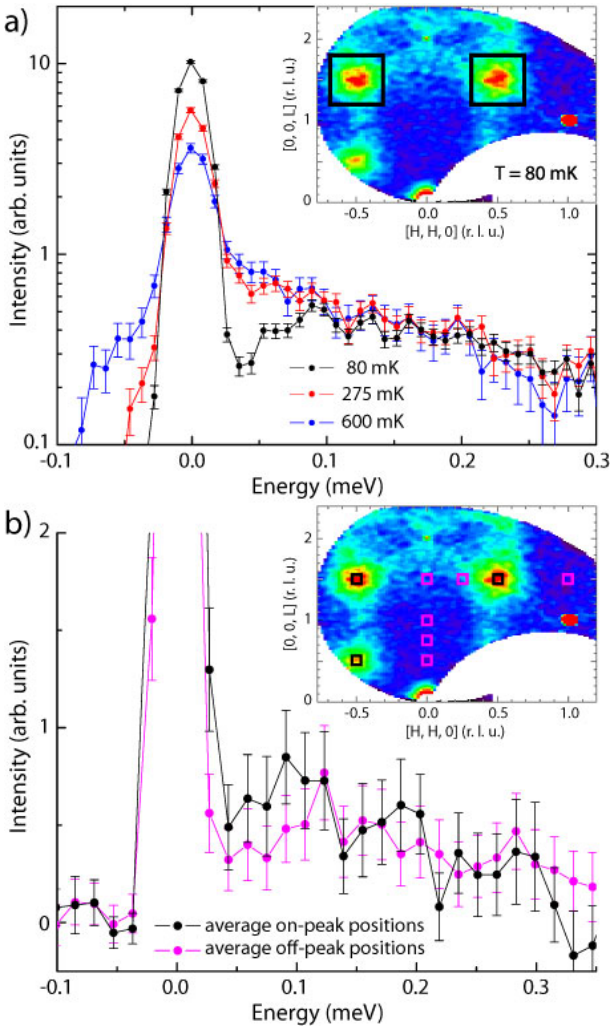

Figure 5.12: High-resolution neutron scattering data of $Tb_2Ti_2O_7$ in zero field. Panel (a) shows a plot of intensity vs energy transfer of the $(\frac{1}{2},\frac{1}{2},\frac{1}{2})$ peak intensity averaged over two peaks as a function of temperature. Note the logarithmic intensity scale. The **Q**-integration range (H= $[\pm 0.3, \pm 0.7]$, L = $[1.2, 1.8]$ r.l.u.) is shown in the inset by the two black squares. Panel (b) shows the intensity vs energy transfer plot for the averaged $(\frac{1}{2},\frac{1}{2},\frac{1}{2})$ (on-peak) positions compared to other averaged (off-peak) positions at a temperature of 80 mK. The integration ranges for the averaging and extraction of the energy dependence is depicted in the inset by the black and magenta squares.

tions (referred to in Fig. 5.12(b) as "on-peak" and "off-peak" positions, which are shown in the black and magenta boxes, respectively, in the inset to Fig. 5.12(b)). The low-energy inelastic scattering appears to be gapped over the entire Brillouin zone, the spectral weight extends ~ 0.03 meV lower in energy at the $\mathbf{Q}=\left(\frac{1}{2},\frac{1}{2},\frac{1}{2}\right)$ frozen spin ice zone center as compared with $\mathbf{Q}$-positions in the middle of the zone. While $Tb_2Ti_2O_7$ in $H = 0$ does not display conventional long-range order at any temperature and therefore does not display well defined spin wave excitations, this observation is consistent with a dispersion of a sort in the spin excitations, softening at the $\mathbf{Q}=\left(\frac{1}{2},\frac{1}{2},\frac{1}{2}\right)$ frozen spin ice zone center.

Taken together, our new neutron scattering data is fully consistent with a spin glass transition near $T_g \sim 275$ mK in $H = 0$. The spin glass state is based on an antiferromagnetic spin ice state, with a low temperature isotropic correlation length of ~ 8 Å, as previously reported. The collapse of the low energy magnetic spectral weight across the magnetic zone into short-range ordered elastic scattering at $\mathbf{Q}=\left(\frac{1}{2},\frac{1}{2},\frac{1}{2}\right)$ wave vectors is a necessary component to this picture, informing on the magnetism in the frequency or time domain. It is also inconsistent with the singlet ground state scenario proposed theoretically for $Tb_2Ti_2O_7$ at low temperatures, as the inelastic magnetic intensity which forms the gap is transferred to elastic magnetic scattering, as opposed to being transferred above the gap leaving a nonmagnetic ground state and an absence of elastic magnetic scattering. The magnetic spin glass ground state based on antiferromagnetic spin ice is also consistent with ac-susceptibility measurements which also show canonical signatures for spin glass ground states in a variety of $Tb_2Ti_2O_7$ samples, both in polycrystalline and single crystal form.

While there is some sample variation observed in the precise temperature at which a signature for a spin glass ground state is seen in $Tb_2Ti_2O_7$, all samples reported to date have shown such a signature in the approximate temperature range of 150-275 mK, consistent with the neutron scattering measurements we present.

5.2.5 Specific Heat

Significant sample variability has however been reported in anomalies, and the lack thereof, in the low temperature heat capacity measured on different samples of $Tb_2Ti_2O_7$. We note that sample variability in the position and sharpness of heat capacity anomalies at low temperature in $Yb_2Ti_2O_7$ have also been reported,[32] and these have been ascribed to the relative role of weak "stuffing" (excess Yb ions substituting on the Ti sublattice at the $\sim 2\%$ level). In particular, Taniguchi and co-workers studied a family of polycrystalline samples of the form $Tb_{2+x}Ti_{2-x}O_7$ for very small non-stoichiomtery, $|x| < 0.005$.[46] They report very significant variability in both the temperature at which the heat capacity anomaly is observed, as well as in the amplitude of the anomaly. These anomalies in C_P are typically observed in the 400 mK to 500 mK regime in zero field, and these results present two important questions for our study. First, does our neutron scattering single crystal sample of $Tb_2Ti_2O_7$ display such a C_P anomaly; if so how strong and at what temperature? Second, what is the relation between these sample dependent C_P anomalies in zero field in $Tb_2Ti_2O_7$ and the transition to the frozen spin ice state we observe in our neutron scattering sample at $T_g \sim 275$ mK?

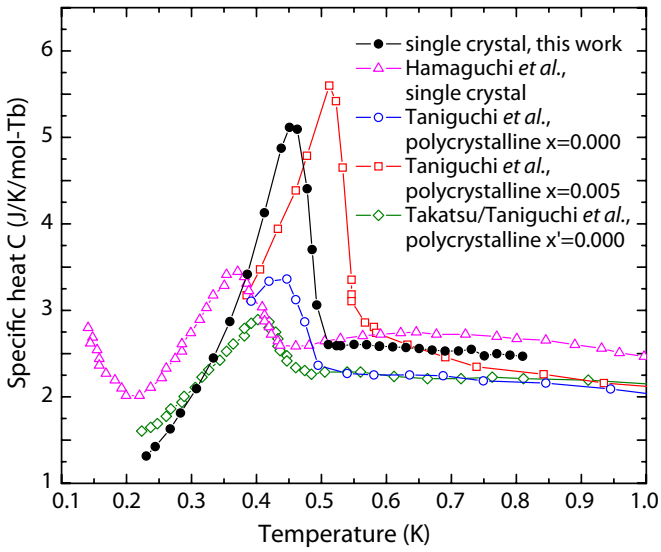

Figure 5.13: Specific heat versus temperature for single crystalline $Tb_2Ti_2O_7$ in zero magnetic field. The feature at 450 mK does not coincide with the glass-like transition at 275 mK indicated by the neutron scattering measurements. For comparison, we also show C_P data taken from the literature.[36,46]

To address these questions we performed specific heat measurements down to a temperature of 220 mK on a 33.8 mg single crystal sample, cut from the neutron scattering sample which was the focus of this paper and, as already mentioned, that of a previous study.[25] Figure 5.13 shows the measured specific heat of our single crystal sample of $Tb_2Ti_2O_7$, compared with several other samples, both single crystals and polycrystals, taken from the literature.[36,46] As can be seen from Fig. 5.13, we observe a relatively large anomaly in C_P at $\sim$ 450 mK, almost twice the T_g associated with the frozen spin ice state characterized in this paper with neutron scattering. For reference, we have indicated the location of the C_P anomaly in zero field in Fig. 5.9(c), which also shows the temperature dependence of the $\mathbf{Q}=\left(\frac{1}{2},\frac{1}{2},\frac{1}{2}\right)$ elastic scattering. Clearly, the temperature scales associated with the results of these measure-

ments are distinct. As this $\sim$ 450 mK temperature scale is not present in either our neutron scattering results or ac-susceptibility results on $Tb_2Ti_2O_7$ taken from the literature, we conclude that while this heat capacity anomaly and its associated sample dependence are intriguing and potentially important phenomena, they do not originate from dipole magnetic degrees of freedom in $Tb_2Ti_2O_7$, similarly to what is found in $Yb_2Ti_2O_7$.[71]

5.2.6 Conclusion

In conclusion, our neutron scattering data on $Tb_2Ti_2O_7$ in a magnetic field show that a small field of $\sim$ 0.075 T applied along [1-10] is sufficient to destroy the short-range antiferromagnetically ordered spin ice state characterized by diffuse elastic scattering at $(\frac{1}{2},\frac{1}{2},\frac{1}{2})$ positions. This field range is consistent with a $H_C \sim 0.067$ T for fields along [111] reported by Yin *et al.*,[60] who also suggest that the zero-field ground state of $Tb_2Ti_2O_7$ is a quantum spin ice. The temperature dependence of the elastic diffuse scattering reveals a spin glass-like freezing at $T_g \sim 275$ mK. The details of the neutron signatures associated with the $(\frac{1}{2},\frac{1}{2},\frac{1}{2})$ elastic scattering display some history-dependence. The appearance of the elastic diffuse scattering below 275 mK correlates with the opening of a spin gap of 0.06-0.08 meV over most of reciprocal space and concomitant weakly dispersive spin excitations extending out to $\sim$0.2 meV. These excitations appear to go soft at the short-range ordering positions of $(\frac{1}{2},\frac{1}{2},\frac{1}{2})$.

Specific heat measurements on a piece of the same single crystal show an anomaly at 450 mK, consistent with other reports by Hamaguchi *et al.* and

Taniguchi *et al.* However, we observe no signs for an anomaly near 275 mK, indicating that different degrees of freedom are involved in the ordering process responsible for this specific heat anomaly in $Tb_2Ti_2O_7$.

The new neutron measurements we report on the temperature and magnetic field parametrics allow us to complete the H-T magnetic phase diagram for $Tb_2Ti_2O_7$ in a [1-10] magnetic field. We find the dynamic and disordered, cooperative paramagnetic phase, which generated much of the original interest in $Tb_2Ti_2O_7$, to be bracketed by a low-field frozen spin ice state, and a field-induced, long-range ordered antiferromagnetic state at high fields.

The authors acknowledge useful contributions from M. J. P. Gingras. This work utilized facilities supported in part by the National Science Foundation under Agreement No. DMR-0944772, and was supported by NSERC of Canada. The DAVE software package[47] was used for data reduction and analysis of DCS data.

5.3 * References

[1] C. Lacroix, P. Mendels, and F. Mila, in *Introduction to Frustrated Magnetism* (Springer Series in Solid-State Sciences, Heidelberg, 2011).

[2] J. S. Gardner, M. J. P. Gingras, and J. E. Greedan, Rev. Mod. Phys. **82**, 53 (2010).

[3] L. Savary, K. A. Ross, B. D. Gaulin, J. P. C. Ruff, and L. Balents, Phys. Rev. Lett. **109**, 167201 (2012).

[4] M. E. Zhitomirsky, M. V. Gvozdikova, P. C. W. Holdsworth, and R. Moessner, Phys. Rev. Lett. **109**, 077204 (2012).

[5] S. T. Bramwell and M. J. P. Gingras, Science **294**, 1495 (2001).

[6] M. J. P. Gingras, in *Introduction to Frustrated Magnetism*, edited by C. Lacroix, P. Mendels, and F. Mila (Springer Series in Solid-State Sciences, Heidelberg, 2011), Chap. Spin Ices.

[7] C. L. Henley, Annu. Rev.: Condens. Matter Phys. **1**, 179 (2010).

[8] C. Castelnovo, R. Moessner, and S. Sondhi, Annu. Rev.: Condens. Matter Phys. **3**, 35 (2012).

[9] S. Lee, S. Onoda, and L. Balents, Phys. Rev. B **86**, 104412 (2012).

[10] S. Onoda and Y. Tanaka, Phys. Rev. Lett. **105**, 047201 (2010).

[11] S. Onoda and Y. Tanaka, Phys. Rev. B **83**, 094411 (2011).

[12] K. A. Ross, L. Savary, B. D. Gaulin, and L. Balents, Phys. Rev. X **1**, 021002 (2011).

[13] R. Applegate, N. R. Hayre, R. R. P. Singh, T. Lin, A. G. R. Day, and M. J. P. Gingras, Phys. Rev. Lett. **109**, 097205 (2012).

[14] L.-J. Chang, S. Onoda, Y. Su, Y.-J. Kao, K.-D. Tsuei, Y. Yasui, K. Kakurai, and M. R. Lees, Nat. Commun. **3**, 992 (2012).

[15] L. Balents, Nature **464**, 199 (2010).

[16] J. S. Gardner, S. R. Dunsiger, B. D. Gaulin, M. J. P. Gingras, J. E. Greedan, R. F. Kiefl, M. D. Lumsden, W. A. MacFarlane, N. P. Raju, J. E. Sonier, I. Swainson, and Z. Tun, Phys. Rev. Lett. **82**, 1012 (1999).

[17] J. S. Gardner, A. Keren, G. Ehlers, C. Stock, E. Segal, J. M. Roper, B. Fåk, M. B. Stone, P. R. Hammar, D. H. Reich, and B. D. Gaulin, Phys. Rev. B **68**, 180401 (2003).

[18] M. J. P. Gingras, B. C. den Hertog, M. Faucher, J. S. Gardner, S. R. Dunsiger, L. J. Chang, B. D. Gaulin, N. P. Raju, and J. E. Greedan, Phys. Rev. B **62**, 6496 (2000).

[19] S. T. Bramwell and M. J. Harris, J. Phys.: Condens. Matter **10**, L215 (1998).

[20] H. R. Molavian, M. J. P. Gingras, and B. Canals, Phys. Rev. Lett. **98**, 157204 (2007).

[21] H. R. Molavian, P. A. McClarty, and M. J. P. Gingras, (2009), arXiv:0912.2957v1 [cond-mat.stat-mech].

[22] P. Bonville, I. Mirebeau, A. Gukasov, S. Petit, and J. Robert, Phys. Rev. B **84**, 184409 (2011).

[23] B. D. Gaulin, J. S. Gardner, P. A. McClarty, and M. J. P. Gingras, Phys. Rev. B **84**, 140402 (2011).

[24] J. S. Gardner, B. D. Gaulin, A. J. Berlinsky, P. Waldron, S. R. Dunsiger, N. P. Raju, and J. E. Greedan, Phys. Rev. B **64**, 224416 (2001).

[25] K. C. Rule, J. P. C. Ruff, B. D. Gaulin, S. R. Dunsiger, J. S. Gardner, J. P. Clancy, M. J. Lewis, H. A. Dabkowska, I. Mirebeau, P. Manuel, Y. Qiu, and J. R. D. Copley, Phys. Rev. Lett. **96**, 177201 (2006).

[26] I. Mirebeau, P. Bonville, and M. Hennion, Phys. Rev. B **76**, 184436 (2007).

[27] H. A. Dabkowska and A. B. Dabkowski, in *Crystal Growth of Oxides by Optical Floating Zone Technique. Experimental Approach to Defects Determination* (Springer Handbook of Crystal Growth, Defects and Characterization, Berlin, 2010), pp. 367–392.

[28] J. Gardner, B. Gaulin, and D. McK Paul, J. Cryst. Growth **191**, 740 (1998).

[29] J. R. D. Copley and J. C. Cook, Chem. Phys. **292**, 477 (2003).

[30] R. Bewley, J. Taylor, and S. Bennington, Nuclear Instruments and Methods in Physics Research Section A: Accelerators, Spectrometers, Detectors and Associated Equipment **637**, 128 (2011).

[31] P. J. Brown, International Tables for Crystallography **C**, 454 (2006).

[32] K. A. Ross, T. Proffen, H. A. Dabkowska, J. A. Quilliam, L. R. Yaraskavitch, J. B. Kycia, and B. D. Gaulin, Phys. Rev. B **86**, 174424 (2012).

[33] I. Mirebeau, A. Apetrei, J. Rodriguez-Carvajal, P. Bonville, A. Forget, D. Colson, V. Glazkov, J. P. Sanchez, O. Isnard, and E. Suard, Phys. Rev. Lett. **94**, 246402 (2005).

[34] S. Petit, P. Bonville, I. Mirebeau, H. Mutka, and J. Robert, Phys. Rev. B **85**, 054428 (2012).

[35] J. D. M. Champion, A. S. Wills, T. Fennell, S. T. Bramwell, J. S. Gardner, and M. A. Green, Phys. Rev. B **64**, 140407 (2001).

[36] N. Hamaguchi, T. Matsushita, N. Wada, Y. Yasui, and M. Sato, Phys. Rev. B **69**, 132413 (2004).

[37] A. Yaouanc, P. Dalmas de Réotier, Y. Chapuis, C. Marin, S. Vanishri, D. Aoki, B. Fåk, L.-P. Regnault, C. Buisson, A. Amato, C. Baines, and A. D. Hillier, Phys. Rev. B **84**, 184403 (2011).

[38] Y. Chapuis, Ph.D. thesis, Université Joseph Fourier (2009).

[39] H. Takatsu, H. Kadowaki, S. T. J., J. W. Lynn, Y. Tabata, T. Yamazaki, and K. Matsuhira, J. Phys.: Condens. Matter **24**, 052201 (2012).

[40] D. J. P. Morris, D. A. Tennant, S. A. Grigera, B. Klemke, C. Castelnovo, R. Moessner, C. Czternasty, M. Meissner, K. C. Rule, J.-U. Hoffmann, K. Kiefer, S. Gerischer, D. Slobinsky, and R. S. Perry, Science **326**, 411 (2009).

[41] S. T. Bramwell, S. R. Giblin, S. Calder, R. Aldus, D. Prabhakaran, and T. Fennell, Nature **461**, 956 (2009).

[42] T. Fennell, P. P. Deen, A. R. Wildes, K. Schmalzl, D. Prabhakaran, A. T. Boothroyd, R. J. Aldus, D. F. McMorrow, and S. T. Bramwell, Science **326**, 415 (2009).

[43] T. Fennell, M. Kenzelmann, B. Roessli, M. K. Haas, and R. J. Cava, Phys. Rev. Lett. **109**, 017201 (2012).

[44] Y. Yasui, M. Kanada, M. Ito, H. Harashina, M. Sato, H. Okumura, K. Kakurai, and H. Kadowaki, J. Phys. Soc. Jpn. **71**, 599 (2002).

[45] S. Petit, P. Bonville, J. Robert, C. Decorse, and I. Mirebeau, Phys. Rev. B **86**, 174403 (2012).

[46] T. Taniguchi, H. Kadowaki, H. Takatsu, B. Fåk, J. Ollivier, T. Yamazaki, T. J. Sato, H. Yoshizawa, Y. Shimura, T. Sakakibara, T. Hong, K. Goto, L. R. Yaraskavitch, and J. B. Kycia, Phys. Rev. B **87**, 060408 (2013).

[47] R. T. Azuah, L. R. Kneller, Y. Qiu, P. L. W. Tregenna-Piggott, C. M. Brown, J. R. D. Copley, and R. M. Dimeo, J. Res. Natl. Inst. Stan. Technol. **114**, 341 (2009).

[48] http://www.mantidproject.org/ (2012).

[49] T. G. Perring, R. A. Ewings, and J. V. Duijn, http://horace.isis.rl.ac.uk, and unpublished (2009).

[50] T.-H. Han, J. S. Helton, S. Chu, D. G. Nocera, J. A. Rodriguez-Rivera, C. Broholm, and Y. S. Lee, Nature **492**, 406 (2012).

[51] J. S. Helton, K. Matan, M. P. Shores, E. A. Nytko, B. M. Bartlett, Y. Yoshida, Y. Takano, A. Suslov, Y. Qiu, J.-H. Chung, D. G. Nocera, and Y. S. Lee, Phys. Rev. Lett. **98**, 107204 (2007).

[52] Y. Shimizu, K. Miyagawa, K. Kanoda, M. Maesato, and G. Saito, Phys. Rev. Lett. **91**, 107001 (2003).

[53] F. L. Pratt, P. J. Baker, S. J. Blundell, T. Lancaster, S. Ohira-Kawamura, C. Baines, Y. Shimizu, K. Kanoda, I. Watanabe, and G. Saito, Nature **471**, 612 (2011).

[54] P. Bonville, S. Petit, I. Mirebeau, J. Robert, E. Lhotel, and C. Paulsen, http://arxiv.org/abs/1302.6418 (2013).

[55] J. P. C. Ruff, B. D. Gaulin, J. P. Castellan, K. C. Rule, J. P. Clancy, J. Rodriguez, and H. A. Dabkowska, Phys. Rev. Lett. **99**, 237202 (2007).

[56] J. P. C. Ruff, Z. Islam, J. P. Clancy, K. A. Ross, H. Nojiri, Y. H. Matsuda, H. A. Dabkowska, A. D. Dabkowski, and B. D. Gaulin, Phys. Rev. Lett. **105**, 077203 (2010).

[57] E. Lhotel, C. Paulsen, P. D. de Réotier, A. Yaouanc, C. Marin, and S. Vanishri, Phys. Rev. B **86**, 020410 (2012).

[58] P. J. Baker, M. J. Matthews, S. R. Giblin, P. Schiffer, C. Baines, and D. Prabhakaran, Phys. Rev. B **86**, 094424 (2012).

[59] S. Legl, C. Krey, S. R. Dunsiger, H. A. Dabkowska, J. A. Rodriguez, G. M. Luke, and C. Pfleiderer, Phys. Rev. Lett. **109**, 047201 (2012).

[60] L. Yin, J. S. Xia, Y. Takano, N. S. Sullivan, Q. J. Li, and X. F. Sun, Phys. Rev. Lett. **110**, 137201 (2013).

[61] R. Higashinaka, private communication.

[62] K. Fritsch, K. A. Ross, Y. Qiu, J. R. D. Copley, T. Guidi, R. I. Bewley, H. A. Dabkowska, and B. D. Gaulin, Phys. Rev. B **87**, 094410 (2013).

[63] K. A. Ross, J. P. C. Ruff, C. P. Adams, J. S. Gardner, H. A. Dabkowska, Y. Qiu, J. R. D. Copley, and B. D. Gaulin, Phys. Rev. Lett. **103**, 227202 (2009).

[64] N. R. Hayre, K. A. Ross, R. Applegate, T. Lin, R. R. P. Singh, B. D. Gaulin, and M. J. P. Gingras, Phys. Rev. B **87**, 184423 (2013).

[65] S. H. Curnoe, Phys. Rev. B **88**, 014429 (2013).

[66] A. Yaouanc, P. Dalmas de Réotier, Y. Chapuis, C. Marin, S. Vanishri, D. Aoki, B. Fåk, L.-P. Regnault, C. Buisson, A. Amato, C. Baines, and A. D. Hillier, Phys. Rev. B **84**, 184403 (2011).

[67] J. A. Mydosh, *Spin Glasses: An Experimental Introduction* (CRC Press, Bristol, PA, 1993).

[68] K. Binder and A. P. Young, Rev. Mod. Phys. **58**, 801 (1986).

[69] P. Schiffer group, private communication.

[70] J. S. Gardner, B. D. Gaulin, S.-H. Lee, C. Broholm, N. P. Raju, and J. E. Greedan, Phys. Rev. Lett. **83**, 211 (1999).

[71] R. M. D'Ortenzio, H. A. Dabkowska, S. R. Dunsiger, B. D. Gaulin, M. J. P. Gingras, T. Goko, J. B. Kycia, L. Liu, T. Medina, T. J. Munsie, D. Pomaranksi, K. A. Ross, Y. J. Uemura, T. J. Williams, and G. M. Luke, arXiv:1303.3850 [cond-mat.str-el] (2013).

Chapter 6

Conclusions and Perspectives

In this thesis, three insulating oxide materials based on triangular structural motifs have been studied by neutron scattering techniques. All three show interesting disordered ground states that are a consequence of geometric frustration ($Tb_2Ti_2O_7$), site disorder ($(Co_{1-x}Mg_x)_3V_2O_8$), a combination of site disorder and geometric frustration ($LuCoGaO_4$), and quantum fluctuations introduced by a transverse magnetic field ($Co_3V_2O_8$).

Our neutron scattering measurements on $LuCoGaO_4$ discussed in chapter 3 represent the first time-of-flight neutron scattering study on a single crystal of this material. This work showed this bilayer system to be an excellent approximation of a two-dimensional spin glass characterized by frozen short-range antiferromagnetic correlations extending over $\sim$ 15 Å in decoupled bilayers in the $(ab)^*$ plane. The energy dependence of these spin fluctuations evolves in a manner consistent with a typical spin glass freezing process - again consistent with expectations for a conventional two-dimensional spin glass. In addition, these measurements unexpectedly revealed a well-localized spin excitation, two-dimensional in character, at an energy of $\sim$ 12 meV, whose behavior strongly correlates with the development of the static correlations and

the anisotropy in this system. While the exact nature of this "resonant" spin excitation is not understood, one can speculate that it arises as a consequence of the combination of a gapped spin wave band in the presence of finite spin correlations which effectively broaden the magnetic zone center.

There are several avenues for interesting future work on this material. This could possibly include the tuning of different parameters in this problem, for example by doping with excess Co^{2+} ions substituting for the nonmagnetic Ga^{3+} ions or by applying a transverse magnetic field to the Ising-like spins. In the first case, the doping with Co^{2+} ions might give rise to different phenomena. Firstly, the magnetic properties of the system might change considerably as the Co concentration is raised above the percolation threshold of $p_c = 0.5$ for the triangular lattice, allowing us to study the relative effects of site disorder and geometric frustration. Furthermore, charge-order or polar regions may be so-induced in the system, as has been observed in the isostructural sister compounds $LuFe_2O_4$ or $LuFeCoO_4$, for example. Our group has successfully grown single crystals of $LuCo_{1+x}Ga_{1-x}O_4$ for $x = 0.05$ and $x = 0.25$, that have undergone preliminary structural and magnetic characterization, comparing their properties to the undoped material. The magnetic susceptibility is consistent with spin glass behavior, and interestingly displays the same freezing temperature T_g for all samples, while the antiferromagnetic interactions are seen to change with doping as evidenced by changes in the Curie Weiss behavior at higher temperatures. Furthermore, to study the effects of a magnetic field, we have performed preliminary magnetization measurements on the undoped $LuCoGaO_4$, applying the field in the plane of the bilayers, perpendicular to the Ising axis of the Co^{2+} moments. These measurements reveal a roughly

linear suppression of the freezing temperature by ~ 4 K in fields up to 5.5 T, which indicates that magnetic fields in excess of 25 T might be necessary to suppress the freezing transition altogether.

In chapter 4, two main projects involving the kagome staircase material $Co_3V_2O_8$ have been presented. The first one involved the study of the effects of site disorder in $(Co_{1-x}Mg_x)_3V_2O_8$ by means of magnetization as well as elastic and inelastic neutron scattering measurements. This work showed the magnetic order in $Co_3V_2O_2$ to be very sensitive to nonmagnetic dilution. We found that long-range order in this system is suppressed to below 1.5 K by a doping level of $\sim 19\%$. At first glance surprising, we were able to explain this suppression in a simple, two-dimensional percolation model. In addition, this work confirmed the quasi two-dimensional nature of $Co_3V_2O_8$.

The second project focussed on the study of quantum fluctuations induced by a transverse field in $Co_3V_2O_8$. This is the first work to observe quantum criticality in a quasi two-dimensional Ising system, and will be of significant interest to the condensed matter community. We presented a comprehensive set of elastic and inelastic neutron scattering measurements that reveal several quantum phase transitions in this material. Based on our measurements of the full excitation spectrum in $Co_3V_2O_8$ over a wide range of fields and temperature and the description of the magnetic structure deduced from the elastic scattering, it should be possible for theorists to calculate the spin wave spectrum and to determine the microscopic interactions, at least in the relatively simple high-field and zero-field phases. As starting point of such calculations,

our work presents an important contribution towards a better understanding of this complex material, and of quantum phase transitions in general.

Finally, we presented neutron scattering measurements on the antiferromagnetic pyrochlore spin liquid candidate $Tb_2Ti_2O_7$. Our measurements reveal a new low temperature, low field phase below $\sim$ 275 mK and $\sim$ 0.075 T in this material that corresponds to a frozen short-range antiferromagnetic spin ice phase characterized by the appearance of diffuse elastic $(\frac{1}{2}, \frac{1}{2}, \frac{1}{2})$ scattering and a concomitant gapped, low lying spin excitation spectrum. These measurements are shown to be in agreement with previous ac-susceptibility measurements, and suggest $Tb_2Ti_2O_7$ to form a quantum spin ice state as its ground state, refuting the nonmagnetic singlet ground state scenario proposed in the literature. What is more, our specific heat measurements reveal a sharp anomaly at $\sim$ 450 mK in the same neutron crystal which is clearly not related to this frozen spin ice phase at lower temperature, indicating that different degrees of freedom must be involved. How exactly this anomaly is related to the low temperature behavior of $Tb_2Ti_2O_7$ and recently reported spin-lattice effects at low temperature, and whether this is an important part to the overall picture of how $Tb_2Ti_2O_7$ reaches its ground state remains to be seen.

Katharina Fritsch,

Hamilton, Ontario, Canada

September 03, 2013